Broadband Terahertz Metasurfaces

by

Xiaolong You

B Eng (Communication Engineering),
Nanjing University of Information Science and Technology, China, 2014

M Eng (Electronics and Communication Engineering)
Wuhan University, China, 2016

Thesis submitted for the degree of

Doctor of Philosophy

in

School of Electrical & Electronic Engineering
Faculty of Engineering, Computer & Mathematical Sciences
The University of Adelaide

2021

Supervisors:

Prof. Christophe Fumeaux, School of Electrical & Electronic Engineering

Assoc. Prof. Withawat Withayachumnankul, School of Electrical & Electronic Engineering

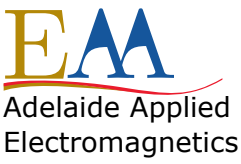

THE UNIVERSITY of ADELAIDE

Contents

Abstract

The terahertz frequency range spans from 0.1 THz to 10 THz and presents unique potential for medical imaging, material characterisation, non-destructive evaluation, and wireless communications. In recent years, various functional devices have been developed to harness the potential of terahertz waves, however mostly with limited bandwidth and efficiency. The thesis presents diverse broadband terahertz metasurfaces for wavefront control and polarisation manipulation. The concept of metasurfaces along with rigorous design approaches yields terahertz components with bandwidth and efficiency superior to existing devices. Such properties are much needed for terahertz technology to leverage vast available bandwidth with moderate source power. This thesis comprises nine chapters in total that are divided into four major parts.

Part I introduces relevant research background and fundamental theories. Specifically, Chapter 1 presents the definitions of terahertz technology and metasurfaces, while Chapter 2 details the fundamental theories involved in this doctoral research.

Part II concerns terahertz reflectarray bandwidth enhancement. A single-layer stub-loaded resonator is proposed in Chapter 3 for constructing broadband reflectarrays. As a proof-of-concept, a terahertz reflectarray is designed, fabricated, and experimentally characterised to focus an incident plane wave to a focal spot at a finite distance.

Part III involves terahertz transmitarrays for antireflection and polarisation manipulation. Each transmitarray employs three metallic layers to realise a complete control over the electric and magnetic responses, so that an arbitrary transmission phase together with high transmittance can be produced. Chapter 4 introduces a broadband semi-analytical approach that is developed on the basis of an existing narrowband method. The broadband approach involves network analysis combined with a genetic algorithm to determine the optimal frequency-independent circuit parameters, so that the desired transmission coefficients can be achieved over a wide bandwidth. In order to illustrate and verify the functionality of this broadband design approach, a wideband and highly efficient antireflection transmitarray is systematically designed based on this approach. Chapters 5 and 6 detail a quarter- and half-wave transmitarray, respectively, which are designed using the same procedure. The measured results confirm the functionality of the proposed quarter- and half-wave transmitarrays and suggest that they

provide superior bandwidth and efficiency over the notable existing designs. Lastly, Chapter 7 shows a terahertz circular polariser with enhanced bandwidth, which is designed with the assistance of the broadband semi-analytical approach. The circular polariser is capable of transmitting circularly polarised waves of one handedness while blocking the other. Importantly, the three-layer circular polariser possesses frequency tunability obtained by adjusting the air spacers. Moreover, by rotating the top or bottom metallic layer, the circular polariser can be reconfigured to function as a transmissive quasi-half-wave plate.

Part IV focuses on ultra-wideband absorber design. Chapter 8 presents a non-resonant absorber that is developed by etching air cavities into moderately doped silicon. In the realised absorber, inverted pyramidal air cavities are etched into doped silicon using a wet-etching technique, so as to realise impedance matching between the lossy silicon and free-space. The measured results demonstrate that a high absorption can be maintained over an ultra-wide bandwidth that spans nearly the entire far-infrared spectrum. The presented absorber far outperforms the existing resonance-based perfect absorbers in terms of achieved fractional bandwidth.

Lastly, Chapter 9 concludes the thesis and gives an outlook of terahertz metasurfaces for practical applications. This thesis introduces technical advancements to metasurface-based terahertz devices for wavefront control and polarisation manipulation. The developed and experimentally validated functional devices can be incorporated into compact terahertz systems, and they address the bandwidth and efficiency limitations associated with the existing designs.

Originality Declaration

I certify that this work contains no material which has been accepted for the award of any other degree or diploma in my name, in any university or other tertiary institution and, to the best of my knowledge and belief, contains no material previously published or written by another person, except where due reference has been made in the text. In addition, I certify that no part of this work will, in the future, be used in a submission in my name, for any other degree or diploma in any university or other tertiary institution without the prior approval of the University of Adelaide and where applicable, any partner institution responsible for the joint-award of this degree.

I acknowledge that copyright of published works contained within this thesis resides with the copyright holder(s) of those works.

I also give permission for the digital version of my thesis to be made available on the web, via the University's digital research repository, the Library Search and also through web search engines, unless permission has been granted by the University to restrict access for a period of time.

Signe

12-June-2021

Date

Acknowledgments

I would like to express my gratitude to all of those people, who have generously encouraged me and provided support during my PhD candidature.

First of all, my deepest gratitude definitely goes to my supervisors Prof. Christophe Fumeaux and Assoc. Prof. Withawat Withayachumnankul. I have been receiving strong support from Prof. Christophe Fumeaux since my PhD scholarship application back in 2015. Prof. Fumeaux has been a very supportive, patient, and responsible supervisor throughout my PhD candidature. His profound knowledge and extensive experience in electromagnetics provided me invaluable suggestions for my doctoral program and publications. Selflessly supporting his students and passionately diving into research are Prof. Fumeaux's iconic images. He is an outstanding supervisor whom I had always wanted to work with and learn from. Dear Christophe, I am so grateful to have your patient guidance, warm encouragement, and enthusiastic supervision, and I will always treasure the memory of being your "neighbour".

I gratefully acknowledge my excellent co-supervisor Assoc. Prof. Withawat Withayachumnankul. His vast and comprehensive knowledge in everything related to terahertz technology assisted me in every research step since the first day of my PhD journey. He was very generous in sharing his knowledge and time, which made me feel free to request for a zoom chat for intellectual supervision at any time. His extremely high standard on work and rigorous attitude towards research have always inspired me. His enlightening questions and critical comments on my research projects and manuscripts trained my logical thinking. He has been a role model for me in every aspect as a scholar. Dear Withawat, I am so appreciated that you are always there when I need guidance. I will always remember your words "you have our full support", which gave me strong strength to face challenges.

I would like to convey my special thanks to Prof. Sharath Sriram, Prof. Madhu Bhaskaran, Mr. Rajour Tanyi Ako, Ms. Mei Xian Low, and Ms. Aditi Upadhyay of the Functional Materials and Microsystems Research Group and the Micro Nano Research Facility at RMIT University, Melbourne. All delicate metasurface prototypes with excellent performance exhibited in this thesis were fabricated by them.

During my PhD candidature, I received plentiful assistance from my colleagues of the Applied Electromagnetics Group and Terahertz Engineering Laboratory at the University of Adelaide, Dr. Shengjian (Jammy) Chen, Dr. Nghia Nguyen Trong, Dr. Sree Pramod Pinapati, Dr. Nicholas Lawrence, Dr. Siti Nailah Mastura Zainarry, Dr. Seyedali Malakooti, Dr. Jin Huang, Dr. Morteza Shahpari, Mr. Ken Paramayudha, Mr. Xiaojing (Alex) Lv, Mr. Weijie (Jack) Gao, Mr. Mohamed Shehata, Ms. Yuan (Grace) Yuan, Mr. Xiaoyang Yin, Mr. Quoc Hung Dang, Ms. Panisa Dechwechprasit, Mr. Mingxiang (Stephen) Li, and Mr. Harrison Lees. Great thanks to Dr. Chengjun Zou for laboratory inductions, Dr. Daniel Headland and Dr. Wendy Suk Ling Lee for invaluable assistance and fruitful discussions in conducting experiments. I would also like to thank Mr. Brandon Pullen for realising high-quality customised device.

To my friends, I appreciate all of you for your helpful advices and extensive support, and I will treasure our happy moments and friendships forever, Dr. Yansong Gao, Dr. Vichet Duk, Jing Zhao, Mi Du, Xuyi Wang, Di Shen, Yang Fei, Bing Yan, Dr. Lin Zhou, Huanhuan Shang, Xiang Zhang, Boya Li, and Yao Li. Special thanks to Qing Lu, who always stands by me and offers me infinite support.

My appreciation goes to China Scholarship Council (CSC) for providing the PhD scholarship that covers my cost of living in Adelaide. Without this scholarship, the thesis would not have been possible. I am also thankful to the School of Electrical and Electronic Engineering, which has financially supported me to attend international conferences and built up connections with the attendees. I would like to extend my gratitude to Adelaide Graduate Centre for offering the Research Travel Scholarship, and the Trustees of the Frank and Hilda Perry Trust for providing The Frank Perry Travelling Scholarship in Engineering.

Last but not least, my endless appreciation goes to my parents, who have been unconditionally and continuously supporting and encouraging me over the past years. I am so fortunate to have parents like them, and no words can fully express my love to them.

Thesis Conventions

The following conventions have been adopted in this Thesis:

Typesetting

This document was compiled using LaTeX2e. Texmaker 5.0.2 was used as text editor interfaced to LaTeX2e. Inkscape 0.92.2 was used to produce schematic diagrams and other drawings.

Spelling

Australian English spelling conventions have been used, as defined in the Macquarie English Dictionary (A. Delbridge (Ed.), Macquarie Library, North Ryde, NSW, Australia, 2001).

Referencing

The Harvard style is used for referencing and citation in this thesis.

System of Units

The units comply with the international system of units recommended in an Australian Standard: AS ISO 1000-1998 (Standards Australia Committee ME/71, Quantities, Units and Conversions 1998).

Publications

Journals

You-X., Ako-R. T., Lee-W. S. L., Bhaskaran-M., Sriram-S., Fumeaux-C., and Withayachumnankul-W. (2021). Terahertz transmissive half-wave metasurface with enhanced bandwidth. (Under review)

You-X., Ako-R. T., Lee-W. S. L., Bhaskaran-M., Sriram-S., Fumeaux-C., and Withayachumnankul-W. (2020). Broadband terahertz transmissive quarter-wave metasurface, *APL Photonics*, **5**(9), art. no. 096108.

You-X., Upadhyay-A., Cheng-Y. Z., Bhaskaran-M., Sriram-S., Fumeaux-C., and Withayachumnankul-W. (2020). Ultra-wideband far-infrared absorber based on anisotropically etched doped silicon, *Optics Letters*, **45**(5), pp. 1196–1199.

You-X., Ako-R. T., Lee-W. S. L., Low-M. X., Bhaskaran-M., Sriram-S., Fumeaux-C., and Withayachumnankul-W. (2019). Terahertz reflectarray with enhanced bandwidth, *Advanced Optical Materials*, **7**(20), art. no. 1900791.

Conferences

You-X., Fumeaux-C., and Withayachumnankul-W. (2021). Concept of mechanically tunable terahertz circular polarizer, *11th International Conference on Metamaterials, Photonic Crystals and Plasmonics (META)*, Warsaw, Poland. (**Invited**; scheduled)

You-X., Fumeaux-C., and Withayachumnankul-W. (2021). Systematically designed broadband terahertz metasurfaces, *SPIE Next-Generation Spectroscopic Technologies XIV*, Florida, USA. (**Invited**)

You-X., Fumeaux-C., and Withayachumnankul-W. (2019). Broadband terahertz quarter-wave plate design, *44th International Conference on Infrared, Millimeter, and Terahertz Waves (IRMMW-THz)*, Paris, France, DOI: 10.1109/IRMMW-THz.2019.8874192.

Upadhyay-A., **You-X.**, Fumeaux-C., Bhaskaran-M., Sriram-S., and Withayachumnankul-W. (2019). Fabrication of broadband absorbers for the far-infrared

spectral range, *44th International Conference on Infrared, Millimeter, and Terahertz Waves (IRMMW-THz)*, Paris, France, DOI: 10.1109/IRMMW-THz.2019.8873993.

You-X., Fumeaux-C., and Withayachumnankul-W. (2018). Terahertz focusing reflectarray with enhanced bandwidth, *43rd International Conference on Infrared, Millimeter, and Terahertz Waves (IRMMW-THz)*, Nagoya, Japan, DOI: 10.1109/IRMMW-THz.2018.8510345.

List of Figures

List of Tables

Chapter 1

Introduction

THE terahertz spectral frequency range is a subset of the electromagnetic spectrum that is sandwiched between the microwave and infrared regimes. Terahertz waves possess unique potential for material characterisation, medical imaging, and wireless communications. However, the terahertz frequency range remains relatively un-tapped as a result of its associated practical challenges. To explore the capabilities of terahertz waves, metasurfaces have emerged as one category of functional terahertz devices. This introductory Chapter presents a general introduction to terahertz waves accompanied with metasurfaces for wavefront control and polarisation manipulation. Furthermore, a summary of motivations and original contributions of this doctoral research is given together with the thesis structure.

1.1 Terahertz waves

The terahertz frequency range that spans from 0.1 to 10 THz is one of the least-utilised portions of the electromagnetic spectrum (Siegel, 2002). The terahertz region overlaps with the millimetre-wave range on its lower frequency bound and the infrared range on its upper frequency bound. More specifically, the terahertz region starts from 0.1 THz and as such intersects with the millimetre-wave range that is defined between 30 GHz and 300 GHz (Wiltse, 1984). The terahertz region covers the entire sub-millimetre-wave regime that ranges from 300 GHz to 3 THz (Wiltse, 1984). At higher frequencies, the terahertz region overlaps with the far-infrared regime, which is defined between 3 THz and 20 THz (Vatansever and Hamblin, 2012).

In the past decades, the terahertz region was often referred to "terahertz gap" due to the lack of techniques for generating and detecting sufficient terahertz power. At frequencies below the terahertz range, electronics-oriented techniques are widely implemented for generating power at microwave and millimetre-wave frequencies (Eisele and Haddad, 1998; Sedra *et al.*, 1998). However, such techniques exhibit a low efficiency at terahertz frequencies, resulting from increasing parasitic effects including Ohmic loss and reactance. At frequencies above the terahertz range, lasers are commonly adopted to function as sources at optical frequencies. However, laser sources demand media that transfer proper levels of energy, which encounter thermal issues at terahertz frequencies (Williams, 2007). Consequently, it is challenging to generate an adequate amount of power for practical applications at terahertz frequencies.

In addition to the inadequate transmitting power, terahertz waves suffer from severe attenuation when propagating in the atmosphere as illustrated in Figure 1.1. The strong atmospheric attenuation is partly attributed to water vapour molecules that are resonant at terahertz frequencies. It can be observed from Figure 1.1 that several transmission windows exist, which present an absorption much lower than the absorption peaks and thus are promising for wireless communications. To account for the attenuation introduced by the atmosphere, an appropriate carrier frequency has to be determined for a specific application. For instance, a carrier frequency of ∼100–150 GHz is suitable for a long-distance transmission of ∼1–10 km, while the two transmission windows above 600 GHz located at ∼625–725 GHz and ∼780–910 GHz are limited for indoor communications (Nagatsuma *et al.*, 2016). Additionally, due to the strong attenuation from water vapour molecules in the propagation path, terahertz waves with a carrier

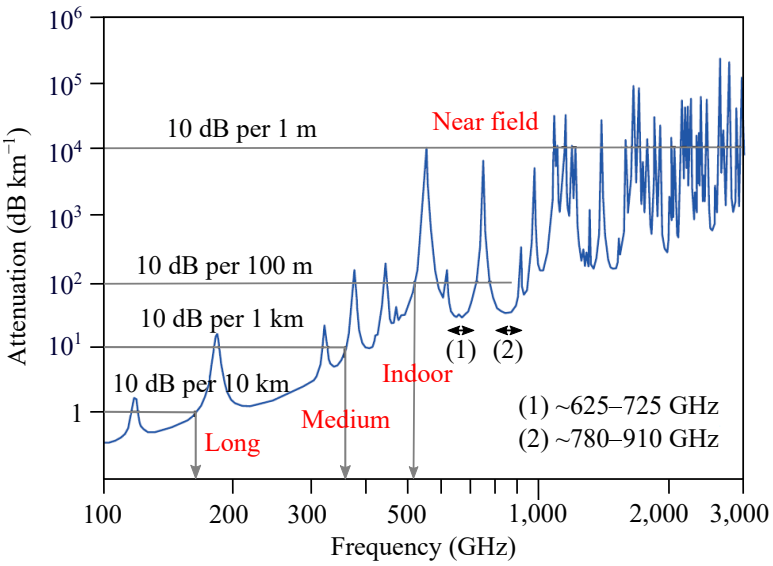

Figure 1.1. Atmospheric attenuation. Attenuation of electromagnetic waves by the atmosphere. Two transmission windows above 600 GHz include ~625–725 GHz and ~780–910 GHz. Adopted from Nagatsuma *et al.* (2016).

frequency of higher than 1 THz can only practically propagate in the range of ~1 m, thus their application is restricted to near-field communications.

In recent years, the rapid evolution of power generation techniques has increasingly made it possible to generate terahertz pulses with sufficient signal strength using terahertz time-domain spectroscopy (THz-TDS) systems. Figure 1.2 shows a commercially available all fibre-coupled terahertz spectrometer TERA K15 developed by Menlo Systems. The system consists of a femtosecond laser source, a fibre-coupled optical path with delay line, a terahertz emitter and detector module. Terahertz pulses are generated and detected by making use of photoconductive antennas that are excited by infrared laser pulses. An attractive feature related to the THz-TDS system is that both the magnitude and phase responses of a sample under test can be readily obtained by transforming the measured time-domain signal to its frequency-domain counterpart. Despite the practical limitations related to terahertz waves, the advent of THz-TDS systems has promoted the use of terahertz waves by exploiting their prominent abilities in spectroscopy and characterisation.

One of the applications benefiting from the development of terahertz technology is material characterisation (Naftaly and Miles, 2007; Scheller, 2011). Many materials, especially crystalline substances and polar gases, present unique spectral characteristics at terahertz frequencies. Terahertz waves thus can be utilised for object identifications

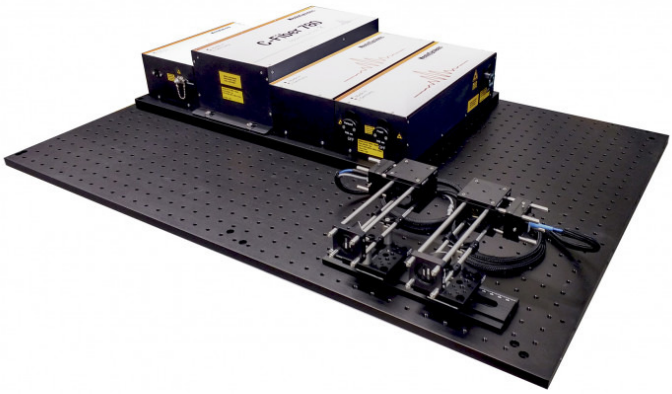

Figure 1.2. Fibre-coupled THz-TDS system TERA K15 from Menlo Systems. The THz-TDS system comprises a femtosecond laser source, a fibre-coupled optical path, a terahertz emitter and detector module. Adopted from Menlo Systems (2020).

(Shen *et al.*, 2005; Miles *et al.*, 2007). Moreover, the relative permittivity and loss tangent of substances can be readily extracted from the transmission coefficients of samples under test (Dorney *et al.*, 2001; Zhang *et al.*, 2017; Sahin *et al.*, 2018). Besides, due to the fact that terahertz waves are sensitive to humidity, they then can be employed to probe the water content of samples (Banerjee *et al.*, 2008; Shin *et al.*, 2017; Fan *et al.*, 2019). To date, material characterisation using terahertz waves has demonstrated its remarkable abilities in chemistry (Balakrishnan *et al.*, 2009; Yakovlev *et al.*, 2015) and biology (George and Markelz, 2013; Yang *et al.*, 2016).

Owing to the low photon energy, terahertz waves are non-ionising and have been employed in medical (Cheon *et al.*, 2017; Hernandez-Cardoso *et al.*, 2017; Zhao *et al.*, 2018a) and biological imaging (Yun *et al.*, 2017; Shi *et al.*, 2018; Wu *et al.*, 2020) to avoid damaging tissues. In addition, the wavelength-dependent diffraction limit determines that terahertz waves are capable of providing improved imaging resolution compared to microwaves and millemetre-waves. Apart from that, terahertz waves can penetrate dry and non-metallic materials that are optically opaque, including polymers, ceramics, and textiles. Hence, terahertz waves hold the potential in security screening to reveal hidden explosives and weapons (Tzydynzhapov *et al.*, 2020; Cheng *et al.*, 2020), as illustrated in Figure 1.3.

The terahertz region offers significant potential for ultrafast-data-rate wireless communications because of its vast under-utilised spectral range. Congestion of wireless

Figure 1.3. Terahertz security screening. Potential application of terahertz imaging at 100 GHz for revealing concealed explosives and weapons. Adopted from Tzydynzhapov *et al.* (2020)

communications bands at microwave and millimetre-wave frequencies results in a limited transmission data rate. To date, noteworthy realisations of wireless communications links employ carrier frequencies up to 60 GHz and provide data rates of ∼3.5 Gbps (Yue *et al.*, 2017). To support large-volume and high-data-rate transfer, the terahertz frequency range provides higher unallocated carrier frequencies and adequate bandwidth. Shannon theorem (Shannon, 1949) suggests that migrating to higher carrier frequencies leads to a broader available bandwidth and thus improved channel capacity. For instance, an experimentally verified terahertz wireless link using a carrier frequency of 300 GHz can realise wireless transmission data rate of 102.4 Gbps (Castro *et al.*, 2020). It is envisioned that moving to even higher terahertz frequencies can achieve even faster data rates, but will encounter a higher atmospheric transmission loss and free-space path loss, and as a result a significantly limited transmission range.

The terahertz spectral range presents unique properties and huge spectral resources making it a promising candidate for a wide range of applications. To harness the capabilities of terahertz waves, intensive efforts have been made to develop functional terahertz devices. One prominent category of terahertz device is metasurfaces. Metasurfaces are seen as essential for manipulating the wavefront and polarisation states of terahertz waves for a myriad of applications. For example, focusing metasurfaces hold the potential of being used for point-to-point terahertz communications, while metasurface-based waveplates can realise polarisation conversion with application in imaging systems.

1.2 Metasurfaces

In the past decades, metamaterials have provided an effective way to manipulate electromagnetic waves. Metamaterials promised an arbitrary combination of effective permittivity and permeability values that are not commonly found in natural materials, thus opening pathways for realising negative refraction (Valentine *et al.*, 2008) and electromagnetic cloaking (Schurig *et al.*, 2006). Owing to its unprecedented capabilities in controlling electromagnetic waves, the concept of metamaterial has been widely implemented for operation across the electromagnetic spectrum, from microwave to optical frequencies (Hawkes *et al.*, 2013; Singh *et al.*, 2009; Valentine *et al.*, 2008). Importantly, metamaterials are attractive to the terahertz community as they break the natural material limitations. However, as metamaterials are typically based on a resonance mechanism, dissipation loss is inevitable, which raises practical challenges. Moreover, bulky metamaterial structures involving multiple layers pose additional complexity to fabrication especially at terahertz frequencies.

In order to overcome the technological challenges associated with three-dimensional metamaterials, metasurfaces that were originally considered as planar building blocks of metamaterials have increasingly received more attention on their own. A metasurface is typically formed by using subwavelength metallic or dielectric resonators arranged as a planar and periodic array. Owing to their planar structures, metasurfaces can be readily fabricated by employing existing standard lithography techniques and also present improved integrability. Furthermore, the reduced thickness of metasurfaces results in a shorter interaction length with the incident waves, thereby leading to a lower dissipation loss compared to that of metamaterials. Each individual element on the metasurface interacts locally with the incident waves to impose a scattering response to the outgoing waves. To obtain the customised radiation characteristics, the employed radiating elements are required to introduce an abrupt phase change coverage of at least 2π at a specified frequency. Owing to their remarkable capabilities in manipulating the wavefront and polarisation states of electromagnetic waves, metasurfaces have been implemented in a myriad of applications from wireless communications (Tang *et al.*, 2019), sensing (Singh *et al.*, 2014), to imaging (Colburn *et al.*, 2018). In general, the metasurface concept is highly relevant to reflectarrays, transmitarrays, and absorbers.

1.2.1 Reflectarrays

A pioneer work relevant to reflectarray introduced a passive reflecting array consisting of shorted waveguides of various lengths (Berry *et al.*, 1963). The reflectarray concept was initially conceived to provide an alternative to reflectors and was then further developed following the advent of printable microstrip antenna techniques (Pozar *et al.*, 1997). The basic form of a reflectarray consists of a planar array of scattering elements on a metal-backed substrate combined with an illuminating free-space feed antenna. A reflectarray can be considered as a hybridisation of a parabolic reflector and a phased array. Its planar structure reduces the fabrication complexity compared to the 3D-shaped reflectors, and the employment of a free-space feed promises high efficiency by eliminating the complicated feeding network demanded by phased arrays. Owing to its advantages of being low profile, low cost, and high efficiency, the reflectarray concept has been widely implemented across the spectrum from microwave and millimetre-wave regions (Tamminen *et al.*, 2013) to optical frequencies (Ahmadi *et al.*, 2010; Zou *et al.*, 2013, 2014). Specifically, reflectarrays developed at terahertz frequencies (Niu *et al.*, 2013, 2014; Chen *et al.*, 2017) address the scarcity of available materials and show significant potential for achieving wavefront control (Busch *et al.*, 2015; Headland *et al.*, 2016a) and polarisation manipulation (Niu *et al.*, 2014).

To achieve low-profile and to simplify the fabrication, various types of scattering elements have been presented to realise the 2π reflection phase coverage at a specified frequency. Figure 1.4 shows some examples of widely implemented scattering elements for broadband reflectarrays. The reflection phase of a scattering element is predominately determined by its geometrical parameters, and thus the reflection phase can be easily tuned by varying its dimensions. A nonuniform reflectarray is formed by a large number of scattering elements of different dimensions and each element introduces a phase discontinuity that collectively alters the phase front of the reflected waves. As a result, constructive interference takes place at the desired direction while destructive interference happens at other directions, leading to a prescribed radiation pattern in the far-field region. Aside from beamforming, a reflectarray can function as a reflective waveplate consisting of uniform scattering elements that jointly provides a constant phase difference between the two orthogonal electric field components over a broad bandwidth. Figure 1.5 presents reflective quarter- and half-wave plates each formed by identical scattering elements (Lee *et al.*, 2018a).

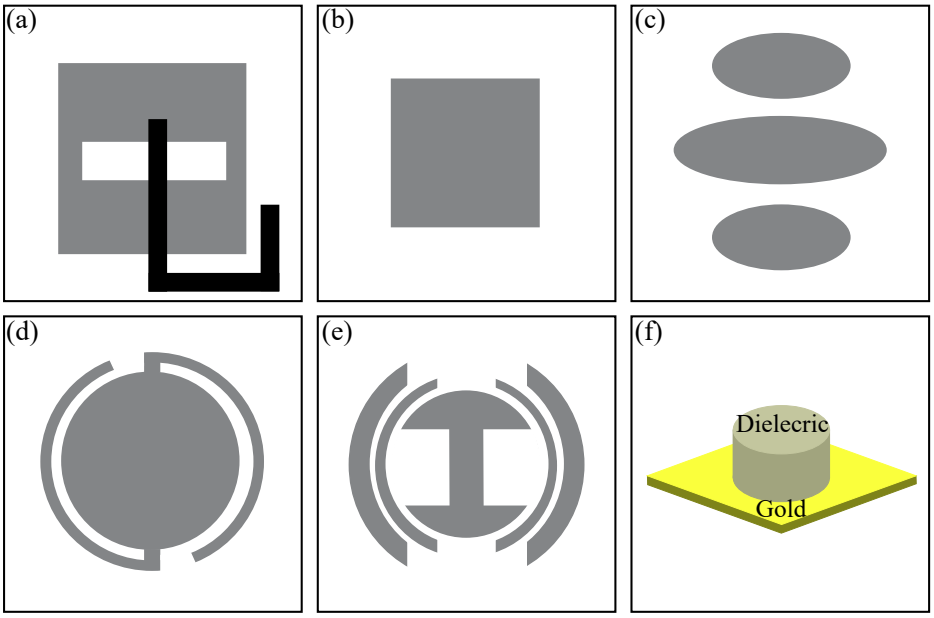

Figure 1.4. Scattering elements for constructing broadband reflectarrays. (a) Aperture-coupled reflectarray unit cell with a true-time delay line. Adapted from Carrasco *et al.* (2007). (b) Square patch of varying lengths. Adapted from Niu *et al.* (2013). (c) Multi-resonant parallel dipoles of varying lengths. Adapted from Niu *et al.* (2015). (d) A round metal disk with phase-delay lines. Adapted from Hasani *et al.* (2010). (e) Reflectarray unit cell consisting of concentric open rings and an I-shaped dipole. Adapted from Chen *et al.* (2012). (f) Dielectric resonator antenna of varying radii. Adapted from Headland *et al.* (2016a).

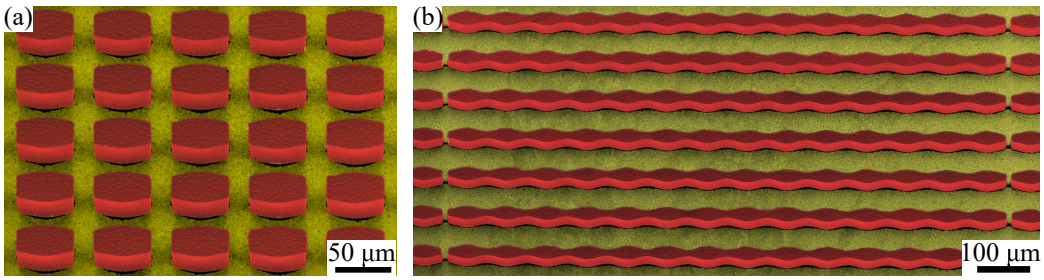

Figure 1.5. Reflectarray-based reflective waveplates made of identical dielectric resonators. (a) Quarter-wave mirror. (b) Half-wave mirror. Adopted from Lee *et al.* (2018a).

1.2.2 Transmitarrays

Conceptually similar to reflectarrays, transmitarrays basically consist of an array of subwavelength metallic or dielectric radiating elements combined with a free-space feed. Different from reflectarrays, transmitarrays operate in the transmission mode so the feed blockage associated with reflectarrays is eliminated. Owing to the advantages

of being low-profile and high-efficiency, transmitarrays have been adopted to design flat lenses (Pfeiffer and Grbic, 2013a; Chang *et al.*, 2017) and polarisation-dependent beam splitters (Yoon *et al.*, 2018). Furthermore, transmitarray-based circular polarisers that selectively transmit one handedness of circular polarisation while blocking the other have been developed and are promising for applications in biological imaging and wireless communications (Pfeiffer and Grbic, 2014).

Despite the advantages, transmitarrays are susceptible to reflection loss, which results in a degraded efficiency. In addition, transmitarrays using one-single layer cannot achieve a complete transmission phase coverage of 2π at a specified frequency. In theory, the maximum transmission phase range is independent of the radiating element pattern. Instead, the transmission phase coverage is set collectively by the number of metallic layers, relative permittivity of spacers, and the separations between metallic layers (Abdelrahman *et al.*, 2017). It is assumed that a transmitarray employs identical patterns for each metallic layer. Calculations suggest that the maximum transmission phase coverage for single-, double-, triple-, and quad-layer transmitarrays are 54°, 170°, 308°, and 360°, respectively, in which a transmission magnitude above -1 dB is maintained (Abdelrahman *et al.*, 2017). Consequently, multi-layer structures are preferred to provide more degrees of freedom to manipulate the transmission magnitude and phase, but at the cost of an increased fabrication complexity. It is worth mentioning that a triple-layer transmitarray that functions as ”Huygens’ Surfaces” employing identical top and bottom metallic layers with the same spacer thickness is capable of providing a large transmission phase tuning range together with a high transmittance, thereby enhancing bandwidth and efficiency (Pfeiffer and Grbic, 2013b).

1.2.3 Absorbers

Electromagnetic absorbers are essential components for wireless communications systems to eliminate electromagnetic interference. Metasurfaces are promising candidates to function as absorbers resulting from their capability in tailoring the electric and magnetic responses for impedance matching. Typically, metasurface-based absorbers consist of two metallic layers separated by a dielectric spacer. The top metallic layer couples with an external incident electric field to tailor the electric response, while the magnetic response is collectively altered by the top metallic layer and a metallic ground plane or metallic wires (Cheng *et al.*, 2015). Hence, the electric and magnetic responses of metasurface-based absorbers can be readily modified by changing their

unit cell shapes and geometrical parameters. In the microwave and terahertz regimes, a near-unity absorption can be achieved by thin metasurface-based absorbers, and the high absorption is derived though impedance matching and dielectric loss at and around the resonant frequencies (Watts *et al.*, 2012). Due to their resonant nature, perfect absorbers typically exhibit a limited relative bandwidth of around 10%–30% (Liu *et al.*, 2018) and can be used in filtering and modulation (Watts *et al.*, 2014).

To obtain a high absorption across a wide spectral range, one possible solution is to combine various resonant structures of different dimensions into a unit cell so as to form a wide absorption band (Wen *et al.*, 2009; Huang *et al.*, 2012). Alternatively, non-resonant structures have demonstrated their broadened absorption bandwidth functionalities in various frequency bands (Kim *et al.*, 2012; Liu *et al.*, 2018). The non-resonant absorbers mitigate the reflection by impedance matching to free space, and dissipate the incident energy through dielectric or conductive losses. Recently, surface-relief structures have been employed to show a broad absorption bandwidth at terahertz frequencies (Kim *et al.*, 2012), and their fabrication complexity is significantly reduced by utilising conventional micro-fabrication techniques.

1.3 Motivations

In the microwave range, reflectors and phased arrays are commonly implemented to concentrate the radiated power into a predesignated direction to improve the antenna gain. In the terahertz region, due to the lack of sufficient power and the strong atmospheric attenuation, practical terahertz communications links demand adequate signal strength to maintain a sufficiently high signal-to-noise ratio. An adequate signal strength can be realised by employing a high-gain antenna. Therefore, wavefront control techniques that collect, manipulate, and re-radiate terahertz beams in a desired manner are of great significance. For instance, it is revealed that if high-gain antennas are employed, terahertz communications links with data transmission rate of several tens of Gbps can be sustained over a propagation distance up to 1 km using carrier frequencies between 300 GHz and 900 GHz (Schneider *et al.*, 2012). Conventional wavefront control devices based on geometric optics, for example lenses, are well-developed and offer a large bandwidth and a low insertion loss. However, practical applications require a high degree of compactness and integrability. Consequently, metasurface-based optical

components with flat-profile, high-efficiency, and improved integrability provide a viable route to meet the stringent requirements set by practical scenarios.

Aside from wavefront control, polarisation manipulation is essential for a wide range of applications in terahertz systems, including studies of chiral structure in biology and chemistry, and polarisation-division multiplexing for terahertz communications. Polarisation manipulation comprises polarisation conversion and circular polarisation filtering. Conventional approaches to achieving polarisation conversion involves waveplates that are made of anisotropic crystalline dielectric materials. The operation mechanism of conventional waveplates can be explained in terms of the distinct phase accumulations for electric field components along two orthogonal polarisations. Due to the birefringent nature of anisotropic crystalline dielectric materials, waveplates made of such a material exhibit different refractive indices to the orthogonal electric field components, thus leading to distinctive transmission phase delays. By carefully determining the thickness of such a birefringent material, a desired phase difference between the two electric field components can be obtained at a specified frequency. However, waveplates made of such materials typically feature substantial thickness, narrow bandwidth, and relatively low efficiency. In addition, there is a lack of available anisotropic birefringent materials in nature that provide desired refractive indices at terahertz frequencies.

Another category of polarisation manipulation is circular polarisation filtering, which selectively transmits one handedness of circular polarisation but blocks the other. It is noted that there is no natural material that yields this function in the terahertz frequency range. Hence, three-dimensional chiral structures such as helices (Gansel *et al.*, 2009) have been employed to realise circular polarisation filtering. However, such three-dimensional structures introduce additional complexities to micro-scale fabrications. Alternatively, planar metasurfaces are attractive for polarisation manipulation with designable birefringence and reduced fabrication complexity.

Despite the fact that metasurfaces promise attractive properties for wavefront control and polarisation manipulation, the inherent characteristic of narrow bandwidth associated with resonance impedes their further applications. For instance, moderate-size reflectarrays typically exhibit a limited fractional bandwidth of less than 10% and the bandwidth even becomes narrower for larger reflectarrays (Huang and Encinar, 2007). In addition to the narrow bandwidth performance, metasurfaces operating at terahertz frequencies are susceptible to non-negligible material losses from metals and dielectrics. One possible solution to mitigate material losses is to implement gold for

metallic layers and ultra-low loss cyclic olefin copolymer (COC) as dielectrics. It is noted that gold acts as a good conductor at terahertz frequencies, and it exhibits a strong anti-oxidization ability in air (Niu, 2015). The research focus of this doctoral program emphasises on designing terahertz metasurfaces for wavefront control and polarisation manipulation with enhanced bandwidth and efficiency.

1.4 Thesis outline

This thesis consists of four major parts, where each part contains one to four chapters. The thesis comprises nine chapters in total including a summary chapter, as illustrated in the outline of Figure 1.6.

Part I - Background The first two chapters explain the motivations and relevant research background for this study. Chapter 1 gives definitions of terahertz technology and metasurfaces, and illustrates the motivations for pursuing broadband

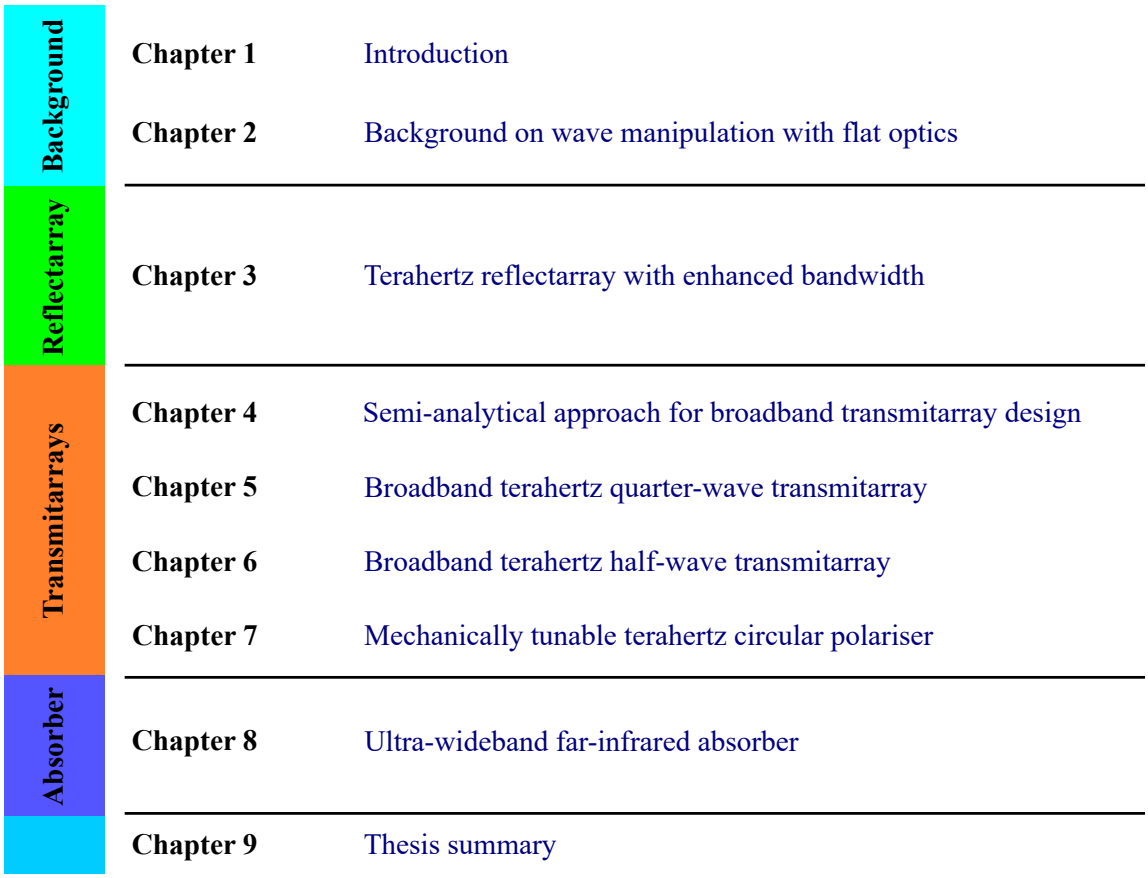

Figure 1.6. Thesis outline. This thesis is grouped into four major parts including background, reflectarray, transmitarrays, and absorber. It is concluded by a thesis summary section.

and high-efficiency terahertz metasurfaces for wavefront control and polarisation manipulation. Chapter 2 details the background knowledge and theory employed in this thesis, including wave generation and propagation theories, wavefront control techniques, and polarisation manipulation methods.

Part II - Reflectarray The work described in this part aims to enhance the bandwidth of reflectarray-based wavefront control devices. In Chapter 3, a single-layer stub-loaded resonator is presented for broadband reflectarray constructions. As a proof-of-concept, a broadband reflectarray that focuses an incident collimated beam into a point at a finite distance is designed, fabricated, and experimentally demonstrated.

Part III - Transmitarrays The objective of this part is to investigate methodologies for designing transmitarrays for antireflection and polarisation manipulation. Firstly, Chapter 4 details a broadband semi-analytical approach that is then applied to designing an antireflection transmitarray with enhanced bandwidth and efficiency. Subsequently, Chapters 5 to 7 present broadband transmitarray-based devices for polarisation manipulation, designed with the same broadband semi-analytical approach. Specifically, Chapters 5 and 6 detail transmitarray-based quarter- and half-wave plates that provide designable birefringence to realise polarisation conversion, while Chapter 7 describes a broadband circular polariser that filters one handedness of circular polarisation but transmits the other. Importantly, further simulations suggest that the presented circular polariser can be reconfigured as a quasi-half-wave plate, and holds the potential of frequency tunability.

Part IV - Absorber This part presents a terahertz absorber based on moderately-doped silicon. The non-resonant absorber is formed by etching air cavities into doped silicon, and providing an ultra-wide and polarisation-insensitive operation bandwidth that is far greater than that of resonance-based perfect absorbers.

1.5 Summary of original contributions

This thesis contains several original contributions to terahertz technology as summarised in this Section. These contributions take the form of novel methodologies for designing and implementing broadband metasurface-based wavefront control and polarisation

manipulation devices, as well as a broadband semi-analytical approach for designing transmitarrays.

Chapter 3 presents a study on broadband terahertz reflectarrays. A novel single-layer resonator is designed to present a smooth and near-linear reflection phase response with a complete 2π phase coverage at 1 THz. A focusing reflectarray has been constructed and experimentally verified to investigate the functionality of the proposed resonator. The simulated 3-dB relative bandwidth of the constructed focusing reflectarray is over twice that of an existing dielectric resonator reflectarray, while the measured relative bandwidth is far greater than the conventionally achievable bandwidth of 10%. To the best of the author's knowledge, this is the largest relative bandwidth of focusing reflectarray that has been achieved to date. The content of this Chapter has been presented at the conference (You *et al.*, 2018) and published in (You *et al.*, 2019a)

- **You-X.**, Fumeaux-C., and Withayachumnankul-W. (2018). Terahertz focusing reflectarray with enhanced bandwidth, *43rd International Conference on Infrared, Millimeter, and Terahertz Waves (IRMMW-THz)*, Nagoya, Japan, DOI: 10.1109/IRMMW-THz.2018.8510345.

- **You-X.**, Ako-R. T., Lee-W. S. L., Low-M. X., Bhaskaran-M., Sriram-S., Fumeaux-C., and Withayachumnankul-W. (2019). Terahertz reflectarray with enhanced bandwidth, *Advanced Optical Materials*, **7**(20), art. no. 1900791.

Chapter 4 presents a broadband semi-analytical approach developed on the basis of a narrowband approach (Pfeiffer and Grbic, 2013c; Pfeiffer and Grbic, 2014). The broadband approach incorporates network analysis and genetic algorithm to explore the optimal frequency-independent circuit parameters for transmitarrays that maintain the desired transmission coefficients over a wide bandwidth. An antireflection transmitarray is rigorously designed following the optimal circuit parameters provided by the broadband semi-analytical approach. The resulting geometry exhibits a superior simulated performance over the existing terahertz antireflection designs. The functionality of the broadband approach is thus validated by the antireflection transmitarray. To the best of the author's knowledge, the proposed antireflection transmitarray provides the largest relative bandwidth together with a high efficiency at terahertz frequencies. The content of this Chapter has been accepted for publication in (You *et al.*, 2021c)

- **YOU-X.**, FUMEAUX-C., AND WITHAYACHUMNANKUL-W. (2021). Systematically designed broadband terahertz metasurfaces, *SPIE Next-Generation Spectroscopic Technologies XIV*, Florida, USA. (**Invited**)

Chapters 5 and 6 present a quarter- and half-wave transmitarray, respectively, which are designed based on the broadband semi-analytical approach. The three-layer quarter-wave transmitarray presented in Chapter 5 employs identical top and bottom metallic layers to form a pair of electric and magnetic dipoles of equal strength. By controlling the resonance of these electric and magnetic dipoles, a large transmission phase coverage accompanied with a high transmittance can be obtained. Importantly, the presented quarter-wave transmitarray provides superior bandwidth and efficiency performance over the notable existing terahertz counterparts. In Chapter 6, a half-wave transmitarray is designed to cover the WR-3.4 waveguide frequency range from 220 to 330 GHz, which is foreseen for terahertz communications. The presented transmitarray-based waveplates overcome the limitations of naturally available birefringent materials and are more amendable to practical applications. To the best of the author's knowledge, both the quarter- and half-wave transmitarrays present the largest bandwidth among the reported designs at terahertz frequencies. The content of this Chapter has been presented at the IRMMW-THz conference in 2019 (You *et al.*, 2019b), with the quarter-wave design published in (You *et al.*, 2020a), and half-wave design submitted for publication in (You *et al.*, 2021a)

- **YOU-X.**, FUMEAUX-C., AND WITHAYACHUMNANKUL-W. (2019). Broadband terahertz quarter-wave plate design, *44th International Conference on Infrared, Millimeter, and Terahertz Waves (IRMMW-THz)*, Paris, France, DOI: 10.1109/IRMMW-THz.2019.8874192.

- **YOU-X.**, AKO-R. T., LEE-W. S. L., BHASKARAN-M., SRIRAM-S., FUMEAUX-C., AND WITHAYACHUMNANKUL-W. (2020). Broadband terahertz transmissive quarter-wave metasurface, *APL Photonics*, **5**(9), art. no. 096108.

- **YOU-X.**, AKO-R. T., LEE-W. S. L., BHASKARAN-M., SRIRAM-S., FUMEAUX-C., AND WITHAYACHUMNANKUL-W. (2021). Terahertz transmissive half-wave metasurface with enhanced bandwidth. (Under review)

Chapter 7 presents a versatile passive circular polariser that can function as a mechanically tunable terahertz device, provided that air gaps are introduced in between the

dielectric spacers. To the best of the author's knowledge, there is no such terahertz passive circular polariser that exhibits frequency tunability. Additionally, the presented circular polariser is capable of providing the largest 15-dB extinction ratio fractional bandwidth at a high efficiency to date. More importantly, simulations suggest that the proposed three-layer circular polariser can also realise circular polarisation transformation from one handedness to the other by rotating the top or bottom metallic layer. The content of this Chapter has been accepted for publication in (You *et al.*, 2021b)

- **You-X.**, Fumeaux-C., and Withayachumnankul-W. (2021). Concept of mechanically tunable terahertz circular polarizer, *11th International Conference on Metamaterials, Photonic Crystals and Plasmonics (META)*, Warsaw, Poland. (**Invited**; scheduled)

Chapter 8 presents an ultra-wideband absorber made of moderately-doped silicon. The non-resonant absorber realises impedance matching to free-space by forming inverted pyramidal air cavities into the doped silicon using a wet-etching technique. As a result, a high absorption that spans nearly the entire far-infrared spectrum is achieved. This non-resonant absorber far outperforms the existing resonance-based perfect absorbers. To the best of the author's knowledge, the presented absorber provides the largest relative bandwidth across the far-infrared spectrum. The content of this Chapter has been published in (You *et al.*, 2020b)

- **You-X.**, Upadhyay-A., Cheng-Y. Z., Bhaskaran-M., Sriram-S., Fumeaux-C., and Withayachumnankul-W. (2020). Ultra-wideband far-infrared absorber based on anisotropically etched doped silicon, *Optics Letters*, **45**(5), pp. 1196–1199.

The developed methodologies to metasurface-based functional devices for wavefront control and polarisation manipulation contribute to the practical applications of terahertz technology. Particularly, these devices are integratable in compact systems and they overcome the bandwidth and efficiency limitations of existing designs.

Chapter 2

Background on wave manipulation with flat optics

THIS Chapter introduces the fundamental theories of wavefront control and polarisation manipulation that are relevant to the thesis. Specifically, this Chapter focuses on the control of field distributions and polarisation states of terahertz beams by metasurfaces, so that they reflect or transmit waves in a desired manner. Wave generation and propagation models including the Huygens-Fresnel principle and array theory are employed in this thesis as effective tools, and so they are briefly presented. Subsequently, some representative wavefront control techniques such as beam focusing, beam deflection, and Bessel beam generation are presented. Lastly, the operation mechanisms of waveplates and circular polarisers are discussed.

2.1 Introduction

This Chapter aims to offer a theoretical background for wavefront control and polarisation manipulation of terahertz waves. Metasurfaces promise versatile functionalities for wave manipulation, and they are typically composed of subwavelength metallic or dielectric scattering elements. Thus, the metasurface concept is highly relevant to diffracting apertures and array antennas. Section 2.2 presents the Huygens-Fresnel principle and array theory to provide a basis for calculating the field distribution of diffracting apertures and the radiation pattern of array antennas, respectively. Section 2.3 exhibits some exemplary wavefront control techniques that are directly related to Chapter 3, where a beam focusing reflectarray is realised at terahertz frequencies. Section 2.4 discusses polarisation conversion based on transmissive quarter- and half-wave plates that are relevant to Chapters 5 and 6. In addition, circular polarisation filtering of selectively transmitting one handedness of circular polarisation while blocking the other are also discussed in Section 2.4, and the content of this part is relevant to a transmitarray-based circular polariser design in Chapter 7.

2.2 Wave generation and propagation models

This Section presents wave generation and propagation models consisting of the Huygens-Fresnel principle and array theory for terahertz beam wavefront control. The Huygens-Fresnel principle offers an insight into the propagating beam field distribution of a given diffracting aperture, while array theory provides a way to calculate the radiation pattern of an array antenna. Moreover, the Huygens-Fresnel principle generally determines the field at a specific point in the Cartesian space that is at a limited distance from the diffracting aperture, whereas array theory basically solves the field delivered into a given direction in spherical coordinates that is in the far-field region (Headland, 2017). Although the Huygens-Fresnel principle and array theory emphasise on different aspects of electromagnetic waves propagation, both models are based on a linear superposition of fields radiated from individual sources. Moreover, both models can act as effective tools for predicting the propagating beam behaviour imposed by a metasurface, whose subwavelength resonators can be represented by Huygens' sources or individual scattering elements with controllable amplitude and phase responses.

2.2.1 Huygens-Fresnel principle

The Huygens-Fresnel principle states that each point on a primary wavefront functions as a source that outputs spherical waves for secondary wavelets, and the wavefront at a later instant can be found by constructing the envelope of the secondary wavelets (Goodman, 2005). Each point source that outputs spherical waves is also known as "Huygens' source", and it can be considered as a combination of infinitesimal electric and magnetic dipoles that are orthogonally arranged (Headland *et al.*, 2018a).

It is assumed that waves propagate along the z-axis in Cartesian coordinates. The field distributions of a given diffracting aperture in the observation plane can be readily calculated by using the Huygens-Fresnel principle (Goodman, 2005; Headland *et al.*, 2018a) as follows

$$A(x',y',z) = \frac{1}{j\lambda}\sum_x\sum_y A(x,y,0)\frac{\exp(-jkr_{01})(1+\cos\psi)}{2r_{01}}\Delta x\Delta y, \tag{2.1}$$

where $A = a\exp(j\varphi)$ represents the complex electric field amplitude, in which a is the scalar field amplitude and φ is the phase component. The wavenumber in the propagation medium is denoted by k. As depicted in Figure 2.1, the distance from $(x,y,0)$ to (x',y',z) is $r_{01} = \sqrt{(x'-x)^2+(y'-y)^2+z^2}$, while the angle between a line connecting those two points and the z-axis is represented by ψ. The term of $(1+\cos\psi)/2$ is known as the "obliquity factor", which represents the radiation pattern of a Huygens' source. It should be noted that Equation (2.1) is in the form of Riemann sum, and the summation steps of Δx and Δy are assumed to be in a subwavelength scale, and r_{01}

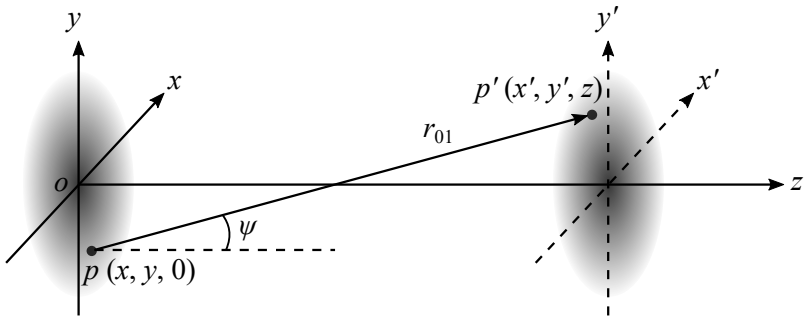

Figure 2.1. Huygens-Fresnel principle solution space. A diffracting aperture is located in $(x,y,0)$ plane, while field distributions that require to be calculated reside in (x',y',z) plane. Points p and p' are for illustration purpose and they are randomly taken from the diffracting aperture and observation plane, respectively. The distance between p and p' is represented by r_{01}, and ψ denotes the angle between pp'-line and the z-axis. Adapted from Headland (2017).

is considered to be far greater than one wavelength. Besides, electromagnetic waves are treated as a scalar field with complex values to simplify the discussion, and their polarisation is neglected (Headland *et al.*, 2018a).

2.2.2 Array theory

An array antenna consisting of a number of radiating elements is widely adopted to achieve a desired radiation characteristic such as an increased gain and a prescribed radiation pattern. As illustrated in Figure 2.2, we consider a linear antenna array comprised of N elements that are arranged along the y-axis, and the distance between the adjacent elements is d. It is assumed that the radiated electric field amplitudes of all elements are equal to E_0, and the phase of the n^{th} radiating element is denoted as φ_n. The radiated electric field of the n^{th} radiating element in the far-field can be expressed as (Niu, 2015)

$$\boldsymbol{E}_n = E_0 e^{-j(kr_n - \varphi_n)}, \tag{2.2}$$

where k is the wavenumber, while r_n is the radial distance between the n^{th} radiating element and a far-field observation point. We consider a progressive phase variation of $\Delta\varphi = \varphi_{n+1} - \varphi_n$ $(n = 1, 2, 3, ..., N-1)$ across the N radiating elements, the phase of the n^{th} radiating element can be written as

$$\varphi_n = \varphi_1 + (n-1)\Delta\varphi. \tag{2.3}$$

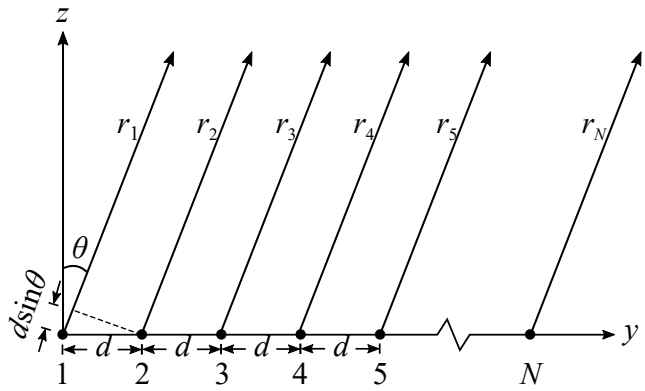

Figure 2.2. Far-field representation of a uniform N-element array positioned along the y-axis. The N elements in the linear array share a uniform electric field magnitude of E_0 and an equivalent element spacing of d, while the phase difference between the neighbouring elements is $\Delta\varphi = \varphi_{n+1} - \varphi_n$ $(n = 1, 2, 3, ..., N-1)$. Thus, the main lobe is steered into a direction of θ with respect to the z-axis. Adapted from Niu (2015).

It can be inferred from Figure 2.2 that the radial distances of neighbouring elements to a far-field observation point satisfy $r_{n+1} - r_n = -d\sin\theta$ $(n = 1, 2, 3, ..., N-1)$. Hence, the radial distance of the n^{th} element to an observation point in the far-field can be written as

$$r_n = r_1 - (n-1)d\sin\theta. \tag{2.4}$$

Inserting Equations (2.3) and (2.4) into Equation (2.2), we obtain the radiated electric field of the n^{th} radiating element in the far-field that can be expressed as

$$\begin{aligned} \boldsymbol{E}_n =& E_0 e^{-j\{k[r_1-(n-1)d\sin\theta]-[\varphi_1+(n-1)\Delta\varphi]\}} \\ =& E_0 e^{-j(kr_1-\varphi_1)} e^{j(n-1)(kd\sin\theta+\Delta\varphi)}. \end{aligned} \tag{2.5}$$

It is assumed that the mutual coupling between the adjacent radiating elements is negligible. The total electric field at the far-field observation point is a vector summation of the radiated fields contributed from each radiating element. This can be written as (Niu, 2015)

$$\begin{aligned} \boldsymbol{E}_{\text{total}} =& \sum_{n=1}^{N} E_0 e^{-j(kr_1-\varphi_1)} e^{j(n-1)(kd\sin\theta+\Delta\varphi)} \\ =& E_0 e^{-j(kr_1-\varphi_1)} \sum_{n=1}^{N} e^{j(n-1)(kd\sin\theta+\Delta\varphi)}. \end{aligned} \tag{2.6}$$

Equation (2.6) indicates that the total electric field of a uniform array in the far-field is equal to the electric field of a single element at the reference point multiplied by a factor, and this factor is known as "array factor" (Balanis, 2016). Thus, for this N-element uniform array of identical field amplitude, the array factor is written as

$$\text{AF} = \sum_{n=1}^{N} e^{j(n-1)(kd\sin\theta+\Delta\varphi)}. \tag{2.7}$$

The array factor of a uniform array depends on the array configuration and phase distribution across the whole array, and each array has its own array factor. It should be emphasised that Equations (2.2)–(2.7) assume a constant electric field amplitude and a progressive phase distribution across the aperture. For the case of an aperture consisting of radiating elements with arbitrary electric field amplitudes and phases, the total electric field at the far-field observation point remains as a vector summation of electric fields from each element, and Equations (2.2)–(2.7) should be altered accordingly to account for the field variations.

2.3 Wavefront control

Wavefront control aims to create desired beam patterns in the near- or far-field region through tailoring the spatial phase distributions of free-space propagating waves (Al-Naib and Withayachumnankul, 2017). Section 2.2 indicates that the wave propagation behaviour in the near- or far-field region can be predicted based on the field distribution over a radiating aperture. Hence, to realise a customised wave behaviour, the field distribution over the radiating aperture needs to be determined accordingly. Specifically, wavefront control of propagating beams is best achieved by prescribing the phase distributions of the radiating aperture rather than the magnitude distributions, so as to provide a higher efficiency and more degrees of freedom to shape the beam characteristics. To illustrate the operation mechanism of wavefront control, here some representative examples are given. For simplicity, the transmitting apertures are situated at $z = 0$ and are parallel to the xy-plane.

2.3.1 Beam focusing

Wavefront control techniques can be employed to focus an incident collimated beam into a focal spot. Figure 2.3 illustrates the principle of phase compensation provided by a transmitting aperture for realising beam focusing. In Figure 2.3, a hyperboloidal equiphase profile is formed by the aperture to ensure that all paths from the equiphase surface to the focal spot share an identical phase retardation, thereby resulting in constructive interferences at the focal spot. To achieve a convergent beam along the z-axis with a finite focal length F from the aperture, the required phase distribution across the transmitting aperture can be calculated by (Headland, 2017)

$$\varphi(x, y) = k_0 \left(\sqrt{F^2 + (x^2 + y^2)} - F \right) + \varphi_0, \tag{2.8}$$

where k_0 is the wavenumber in free-space, while φ_0 denotes an arbitrary phase offset. Equation (2.8) suggests that a frequency-dependent phase distribution is expected to maintain a fixed focal length, while a constant phase distribution would lead to a varying focal length at different frequencies. A collimated beam propagating along the z-axis, and impinging on a transmitting aperture is assumed. Figure 2.4(a) illustrates an example of the required phase distribution across the transmitting aperture for beam focusing calculated by using Equation (2.8). In Figure 2.4(b), an incident collimated beam is effectively converted into a convergent beam, while a well-defined focal spot

is delivered at the focal length of F as depicted in Figure 2.4(c). It should be noted that the $1/e$-radius of the focal spot denoted as w_0 is determined collectively by the Gaussian-distributed aperture radius d and the focal length F as (Saleh and Teich, 2019)

$$w_0 = \frac{\lambda_0 F}{d\pi}, \tag{2.9}$$

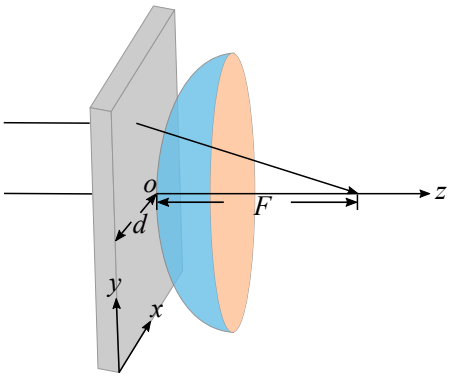

Figure 2.3. Schematic diagram of an equiphase profile formed by the transmitting aperture for beam focusing. An incident plane wave propagates along the z-axis, and converges to a focal spot at $z = F$. The blue hyperboloidal surface indicates an equiphase surface formed by the transmitting aperture, and the distance between any point from the equiphase surface and the focal spot is equal to F. The Gaussian-distributed aperture radius is denoted as d. Adapted from Wang *et al.* (2015b).

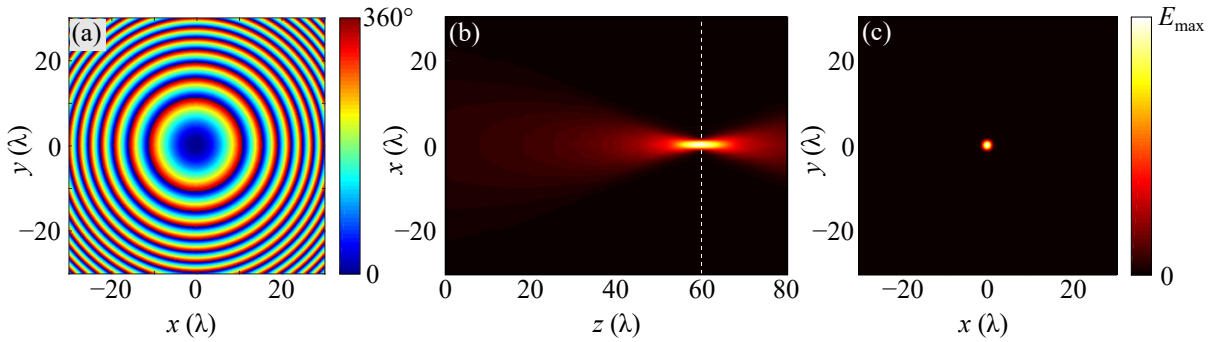

Figure 2.4. Beam focusing illustration. (a) Required phase distribution across the radiating aperture, (b) field distribution of the resultant beam in the transverse xz-plane, and (c) field distribution of the convergent beam in the focal plane of $z = 60\lambda$. The phase distribution shown in (a) is wrapped into a $360°$ cycle. The white dashed line in (b) denotes the focal plane position. Plot (a) is produced with Equation (2.8). Plots (b) and (c) are generated by employing the Huygens-Fresnel principle with Equation (2.1), and both plots are in linear scale and normalised to their respective maxima. A 2D Gaussian function of $1/e$-width 40λ is implemented as the field amplitude distribution with a discretised step of $\Delta x = \Delta y = \lambda/5$ across the Gaussian-distributed aperture.

where λ_0 is the free-space wavelength. It is worth mentioning that such a device that transforms an incident collimated beam into an outgoing convergent beam is also capable of converting a spherical wave into a plane wave in accordance with the reciprocity theorem.

2.3.2 Beam deflection

Beam deflection involves steering an incident beam off a normal path in the far-field region. It can be inferred from array theory that the first maximum of the array factor, which indicates the main lobe of the N-element array antenna radiation pattern, takes place at

$$\Delta\varphi = -k_0 d \sin\theta, \tag{2.10}$$

where k_0 is the free-space wavenumber, and $d \sin\theta$ represents the optical path difference between the adjacent antenna elements after wave propagation. Equation (2.10) suggests that to deflect a normally incident plane wave into a bespoke angle of θ away from the z-axis, a progressive phase change of $\Delta\varphi$ provided by the antenna elements is necessary. To simplify the design and fabrication, a "sub-array" consisting of scattering elements that offers the required progressive and cyclic phase is commonly employed. Typically, the sub-array provides a complete phase cycle of 360°. Identical sub-arrays are arranged periodically to form a linear-ramp phase distribution that can be described as

$$\varphi(x, y) = -k_0 x \sin\theta. \tag{2.11}$$

Figure 2.5 illustrates an example of beam deflection operation, where an incident collimated beam is deflected into a prescribed angle of $\theta = 10°$ away from the z-axis. Figure 2.5(a) shows the required phase distribution across the radiating aperture. It is noted that the phase distribution is wrapped into a 360° cycle, and the linear phase ramp is eventually turned into a sawtooth function. Figure 2.5(b) depicts the field distribution of the tilted beam in the transverse xz-plane, and a desired tilting angle of $\theta = 10°$ is obtained.

Beam deflection presents the potential of controlling the directionality of terahertz beams. For narrow-band operation, beam scanning could be achieved provided that the slope of the linear phase ramp is adjustable at the frequency of interest, so that the outgoing terahertz beams can continuously scan across a given range of angles. For broadband operation, a frequency-independent phase distribution across the radiating

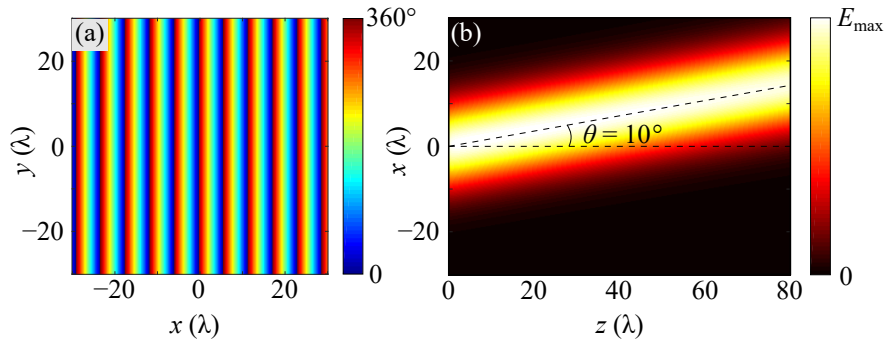

Figure 2.5. Beam deflection illustration. (a) Required phase distribution across the radiating aperture, and (b) field distribution of the resultant propagating beam in the transverse xz-plane. Plot (a) is calculated with Equation (2.11), and the phase distribution is wrapped into a 360° cycle. Plot (b) is generated with Equation (2.1), and the electric field distribution is in linear scale and normalised to its own maximum. A 2D Gaussian function of $1/e$-width 20λ is implemented as the field amplitude distribution with a discretised step of $\Delta x = \Delta y = \lambda/5$ across the Gaussian-distributed aperture.

aperture obtains frequency-dependent beam deflection angles, thus beam scanning across a given frequency range. On the other hand, in order to maintain a constant deflection angle over a wide bandwidth, an adjustable phase distribution is expected.

2.3.3 Other beam shapes

The aforementioned beam deflection is mostly relevant to the far-field region, while beam focusing concerns the near-field regime. Another beam type that operates in the near-field is the Bessel beam, which experiences a long column of constructive interference along the propagation direction, thus directing all fields toward the z-axis. Bessel beams have demonstrated their functionalities in detection (Lv *et al.*, 2020) and imaging systems (Niu *et al.*, 2019). The required phase distribution for generating Bessel beams can be expressed as (Headland *et al.*, 2018a)

$$\varphi(x,y) = k_0 \left(\sqrt{x^2 + y^2} \right) \sin\theta, \tag{2.12}$$

where θ is the deflection angle. Figure 2.6 presents an example of Bessel beam generation, where Figure 2.6(a) shows the required phase distribution calculated by using Equation (2.12) with a deflection angle of $\theta = 20^\circ$. In Figure 2.6(b), constructive interferences occur along the z-axis, where most of the energy is concentrated. Figure 2.6(c) presents the field distribution in the observation plane of $z = 40\lambda$, and concentric rings

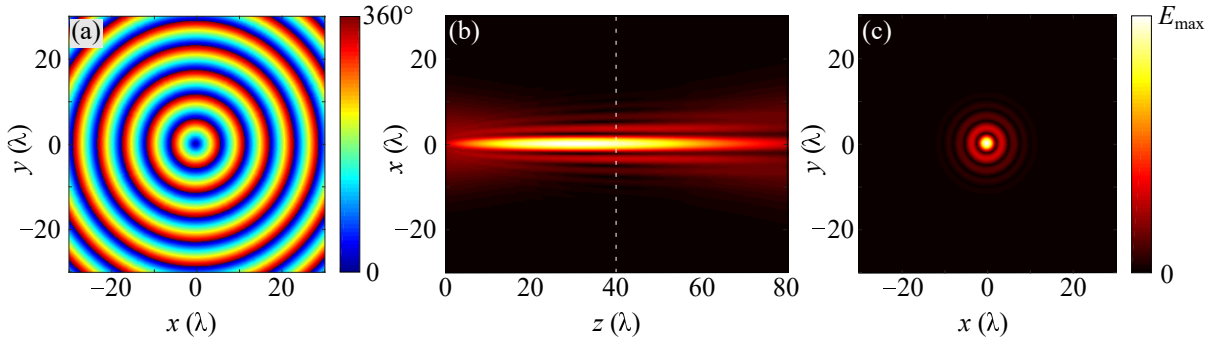

Figure 2.6. Bessel beam generation illustration. (a) Required phase distribution across the radiating aperture, (b) field distribution of the resultant propagating beam in the transverse xz-plane, and (c) beam pattern in the observing xy-plane at $z = 40\lambda$. Plot (a) is created by using Equation (2.12) with a deflection angle of $\theta = 20°$, and the phase distribution is wrapped into a $360°$ cycle. Plots (b) and (c) are calculated based on the Huygens-Fresnel principle with Equation (2.1), and they are in linear scale and normalised to their respective maxima. The white dashed line in (b) denotes the position of the observation plane. A 2D Gaussian function of $1/e$-width 20λ is implemented as the field amplitude distribution with a discretised step of $\Delta x = \Delta y = \lambda/5$ across the Gaussian-distributed aperture.

centred around the z-axis can be found. The formalism of concentric rings can be attributed to the interference between waves that have propagated through the z-axis at an earlier instant and waves that will propagate through the z-axis at a later instant (Headland *et al.*, 2018a).

Aside from Bessel beams, a myriad of beam behaviours exist, including the so called "bottle beam" (Arlt and Padgett, 2000) and beams carrying orbital angular momentum (Sobhani *et al.*, 2016; Rouhi *et al.*, 2019). It is worth noting that a near-arbitrary beam profile can be possibly achieved by employing the Gerchberg-Saxton phase retrieval algorithm (Gerchberg, 1972) to calculate its required phase distribution in a source plane, thus providing a great flexibility for terahertz wavefront control.

2.4 Polarisation manipulation

In addition to wavefront control, terahertz waves polarisation manipulation is also of great interest for a broad area of applications, namely wireless communications, sensing, and imaging. Among various functional terahertz devices, waveplates are widely implemented to realise polarisation conversion, while circular polarisers are adopted to

achieve circular polarisation filtering. This Section details the specific methodologies for polarisation manipulation.

2.4.1 Polarisation conversion

Circularly polarised waves are preferable in wireless communications systems, since they can double channel capacity by encoding distinctive information streams into circular polarisations with different handednesses. Additionally, circularly polarised waves are less affected by the varying environmental conditions compared to linearly polarised waves, making them suitable for long-distance communications. A linearly polarised incident wave can be effectively transformed into a circularly polarised wave by using a quarter-wave plate. Figure 2.7 illustrates the functionality of quarter-wave plates in transmission. A linearly polarised wave propagating along the z-axis is incident on a quarter-wave plate with an angle of 45° with respect to the x-axis, and the electric field can be decomposed into two orthogonal field components oriented along the x- and y-directions, respectively. To realise linear-to-circular polarisation conversion, an identical transmission magnitude for the two orthogonal electric field components and a phase difference of 90° between them is expected. Furthermore, broadband and highly efficient quarter-wave plates are anticipated to maintain a high transmittance and a constant quadrature phase difference over a wide bandwidth.

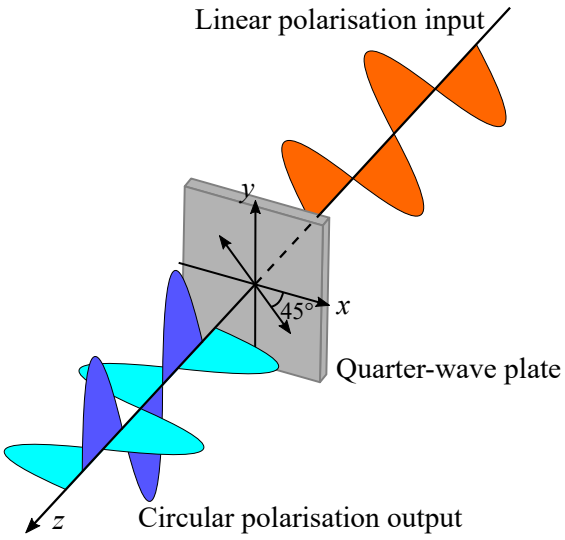

Figure 2.7. Quarter-wave plate operation illustration. A linearly polarised electromagnetic wave propagating along the z-axis is incident on a transmissive quarter-wave plate with an angle of 45° with respect to the x-axis, and then it is effectively converted into a circularly polarised wave.

Conventional quarter-wave plates can be made of birefringent materials such as crystalline quartz (Saha *et al.*, 2012) and liquid crystals (Ji *et al.*, 2018). Birefringent materials exhibit different refractive indices to the two orthogonal electric field components, and hence different phase retardations. Figure 2.8 shows the calculated results of a representative quarter-wave plate made of a single-layer quartz, which presents a refractive index difference of 0.046 between the x- and y-polarisations at 275 GHz (Grischkowsky *et al.*, 1990). The quartz is assumed to be lossless. To acquire the desired 90° phase difference at the design centre frequency of 275 GHz, the quartz-based quarter-wave plate thickness is determined to be 5.88 mm. It can be inferred from Figure 2.8 that strong multiple

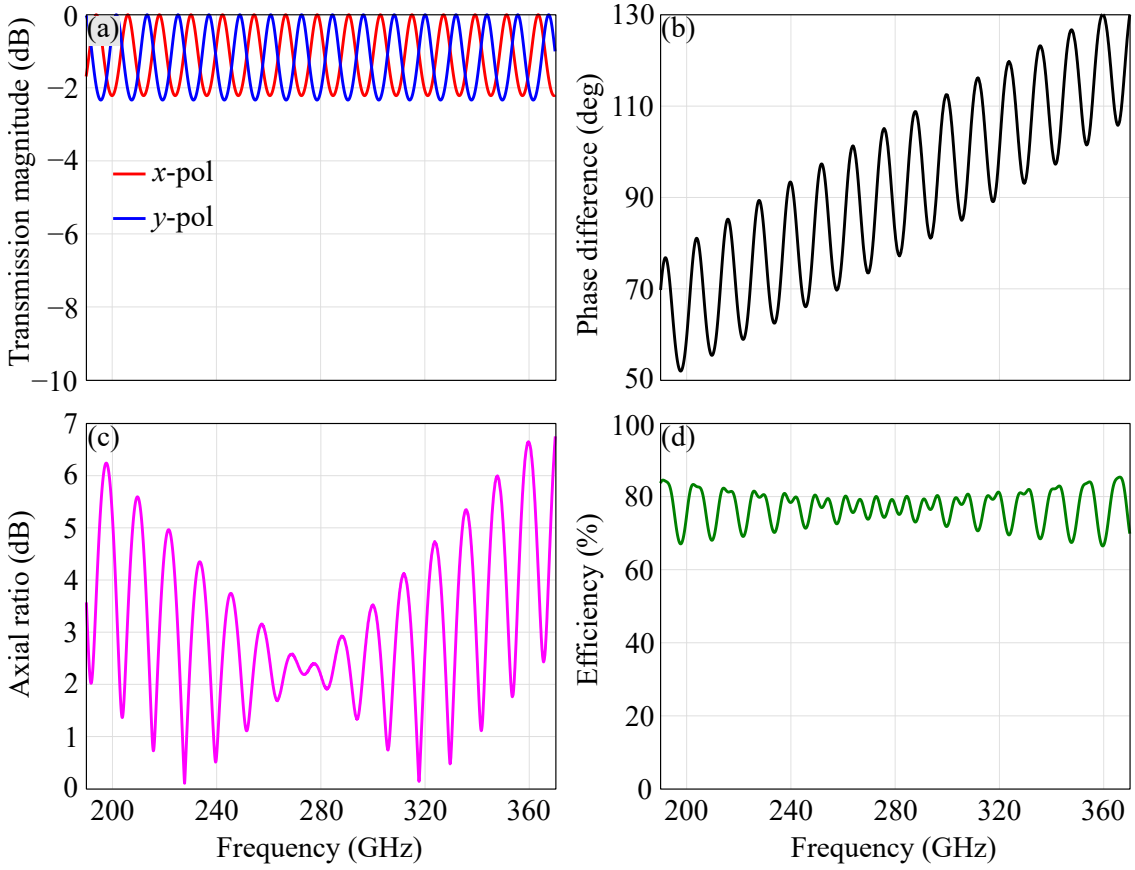

Figure 2.8. Quartz-based quarter-wave plate performance. Calculated results of a single-layer quartz-based quarter-wave plate, showing (a) transmission magnitude, (b) transmission phase difference between x- and y-polarisations, (c) axial ratio, and (d) efficiency. The efficiency accounts for the transmission powers of the x- and y-polarisations, i.e., $\left(|T_{xx}|^2 + |T_{yy}|^2\right)/2$, where T_{xx} and T_{yy} denote the transmission coefficients of the x- and y-polarisations, respectively. The quartz-based quarter-wave plate has a thickness of 5.88 mm. It should be noted that the quartz used here is assumed to be lossless.

reflections occur inside of the quartz, leading to Fabry-Pérot fringes, and these multiple reflections severely affect the performance of the quarter-wave plate. Figure 2.8(c) indicates that this quartz-based quarter-wave plate exhibits a limited 3-dB axial ratio fractional bandwidth of ∼14.4%, while Figure 2.8(d) suggests that an averaged efficiency of ∼77.2% can be obtained within the frequency band of operation. This limited 3-dB axial ratio relative bandwidth is due to the frequency-dependent phase difference and Fabry-Pérot interference, whilst the limited efficiency is due to reflection losses.

Another category of waveplates is the half-wave plate. Half-wave plates are capable of converting linearly polarised waves to their orthogonal counterparts, or transforming circularly polarised waves from one handedness to the other. A broadband and highly efficient half-wave plate working in the transmission mode is expected to deliver an identical and near-unity transmittance for the x- and y-polarisations and a constant phase difference of 180° between them over a wide bandwidth. The aforementioned birefringent materials used for quarter-wave plates are also capable of making half-wave plates. Figure 2.9 shows the calculated results of a single-layer quartz-based half-wave plate. The half-wave plate is assumed to be lossless and exhibits a substantial thickness of 11.76 mm at the design centre frequency of 275 GHz, corresponding to $10.78\lambda_0$, where λ_0 denotes the free-space wavelength. Figure 2.9(a) indicates Fabry-Pérot fringes happen inside of the quartz, while Figure 2.9(b) suggests that the required transmission phase difference of 180° between the two orthogonal polarisations can be only achieved at 275 GHz. Moreover, Figure 2.9(c) illustrates that this half-wave plate can effectively transform circularly polarised waves from one handedness to the other as intended. Hence, the circular polarisation purity of the transmitted wave can be determined by employing the co- and cross-polarisations transmission magnitudes. The axial ratio is widely implemented to quantitatively characterise the circular polarisation purity in the microwave literature, while the extinction ratio functions as its counterpart in optics. Typically, the axial ratio of 3 dB or less is deemed acceptable for the waves to considered circularly polarised, and the 3-dB axial ratio is equivalent to an extinction ratio of ∼15 dB (see Appendix A). Consequently, the 15-dB extinction ratio is used to characterise the half-wave plate. In Figure 2.9(d), the quartz-based half-wave plate enables a 15-dB extinction ratio fractional bandwidth of ∼19.1%, with an average efficiency of 76.5% within the frequency band of operation.

It is obvious that waveplates made of natural birefringent materials suffer from significant reflection losses and exhibit a limited relative bandwidth for operation. In addition,

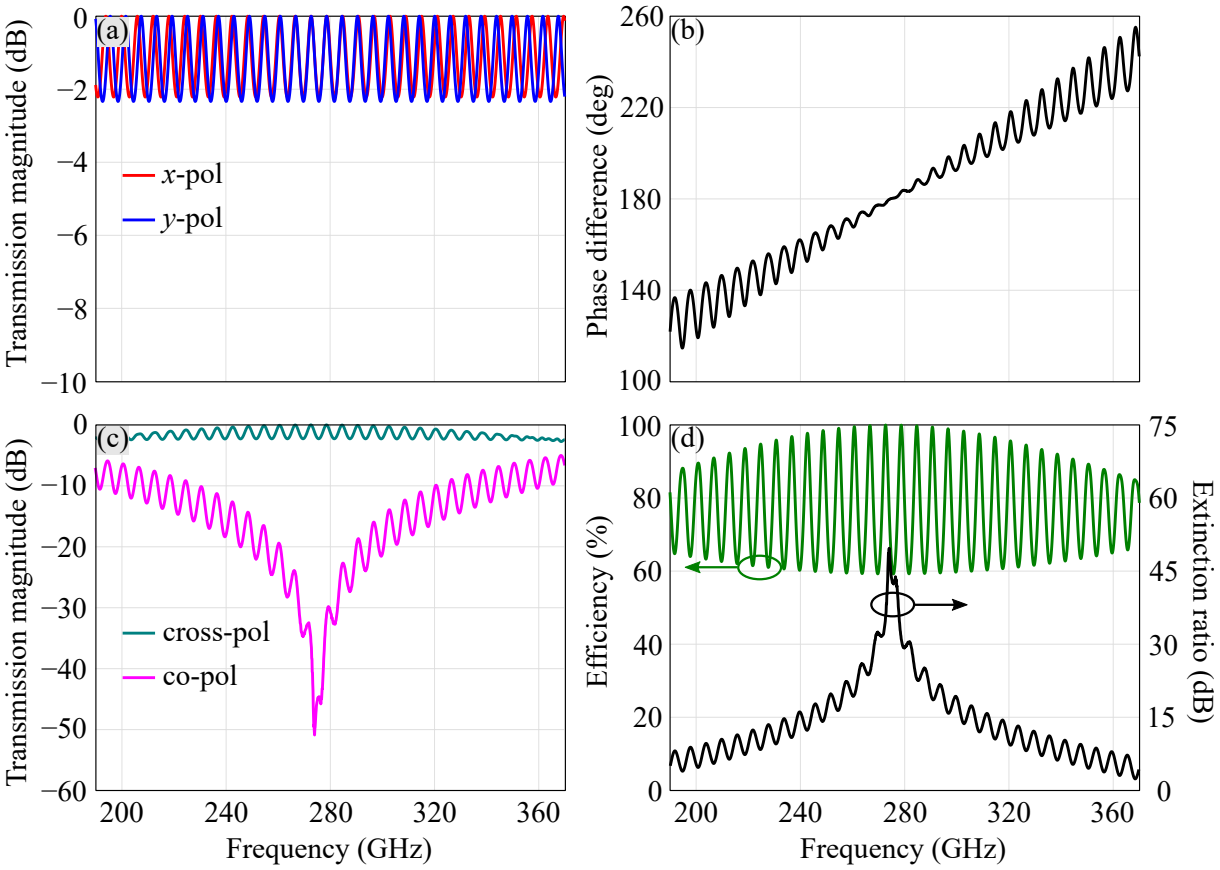

Figure 2.9. Quartz-based half-wave plate performance. Calculated results of a single-layer quartz-based half-wave plate, illustrating (a) transmission magnitudes for the x- and y-polarisations, (b) transmission phase difference between the x- and y-polarisations, (c) co- and cross-polarisations transmission magnitudes, (d) extinction ratio and efficiency. The extinction ratio is defined as $\mathrm{ER} = 10\log_{10}\left(|T_{\mathrm{cross}}|^2/|T_{\mathrm{co}}|^2\right)$, where T_{cross} and T_{co} represent the transmission coefficients of the cross- and co-polarisations, respectively. The efficiency accounts for the transmission power of the cross-polarisation, i.e., $|T_{\mathrm{cross}}|^2$. The quartz-based half-wave plate has a thickness of 11.76 mm. It should be noted that the quartz used here is assumed to be lossless.

the thickness-dependent phase accumulation makes them prohibitively difficult to be integrated into compact systems. Besides, there is a scarcity of naturally available birefringent materials for making waveplates at terahertz frequencies.

2.4.2 Circular polarisation filtering

Circular polarisation filtering is typically achieved by employing circular polarisers that selectively transmit one handedness of circular polarisation but block the other. At

terahertz frequencies, circular polarisation filtering is attractive for imaging platforms to detect chiral structures of different handednesses and for wireless communications systems to reduce cross-talks. At optical frequencies, circular polarisation selectivity is desired for applications in color display (Yoshioka *et al.*, 2005), microscopy and photography (Loksztejn and Dzwolak, 2010). To the best of the author's knowledge, there is no naturally existing material that achieves the circular polarisation selectivity function at terahertz frequencies. A conventional approach to filtering circular polarisation of one handedness is by using three-dimensional helical structures (Gansel *et al.*, 2009, 2012; Yang *et al.*, 2010a). Typically, helical structures block circularly polarised waves of the same handedness as their helices, but transmit the other. An example of circular polariser based on helix arrays is presented by Gansel *et al.* (2009), where a broadband performance at optical frequencies is achieved by combining the internal and Bragg resonances. However, one prominent drawback associated with the helix-array-based circular polariser is the increased fabrication complexity of a three-dimensional structure, making it challenging to realise at terahertz frequencies.

As a planar alternative to three-dimensional helical structures, metasurfaces are promising candidates for designing circular polarisers. To introduce the chirality as demanded by circular polarisation filtering, various bianisotropic metasurfaces were presented. For instance, an optical metasurface based on stacked nanorod arrays with a tailored rotational twist was presented by Zhao *et al.* (2012), which showed an advantage of relaxing the stringent alignment requirement that was common in nano-scale fabrications. Additionally, Huygens' metasurfaces provide a viable route to circular polarisers (Pfeiffer and Grbic, 2014). The chirality induced by Huygens' metasurfaces can be attributed to the interference of multiple reflections between the metallic layers that incur diverse phase discontinuities. However, most existing metasurface-based circular polariser designs in the literature do not involve systematic optimisation methods, leading to relatively vague design procedures and limited bandwidth (Pfeiffer and Grbic, 2014; Momeni Hasan Abadi and Behdad, 2016a)

2.5 Conclusion

This Chapter has firstly introduced wave generation and propagation models consisting of the Huygens-Fresnel principle and array theory. It has subsequently implemented the models to gain an insight into the field distributions of some representative wavefront

control operations. Moreover, polarisation manipulation and its associated challenges have been briefly discussed in this Chapter. Polarisation conversion can be realised by employing waveplates, while circular polarisation filtering can be achieved by implementing circular polarisers. However, conventional waveplates made of natural birefringent materials typically suffer from substantial thickness, narrow bandwidth, limited material availability, and significant reflection loss. Circular polarisers are typically realised by employing three-dimensional structures, thus raising challenges in micro-fabrication at terahertz frequencies. This Chapter has provided a necessary basis for the following Chapters involving metasurface-based wavefront control and polarisation manipulation.

Chapter 3

Terahertz reflectarray with enhanced bandwidth

REFLECTARRAYS offer unique potential for wavefront control at terahertz frequencies as they combine the advantages of low profile of phased arrays and high efficiency of parabolic antennas. However, one challenge associated with reflectarrays is their bandwidth limitation resulting from the non-linear phase response. To enhance bandwidth, a single-layer stub-loaded resonator is proposed for constructing reflectarrays. This resonator design shows a smooth and near-linear phase response with a complete 360° phase coverage at and around the design frequency. To demonstrate its capability in realising wavefront control, a focusing reflectarray is then constructed using the proposed resonator as a building block. The measured results reveal that the 3-dB relative bandwidths of the reflectarray for the transverse electric (TE)- and transverse magnetic (TM)-polarised excitations are 23.3% and 23.9%, respectively, while retaining an efficiency of 71.9% for the TE-polarisation and 71.0% for the TM-polarisation at the centre frequency of 1.00 THz. The simulation bandwidth of this proposed focusing reflectarray is over twice that of an existing dielectric resonator reflectarray. The proposed resonator has a potential to enhance the bandwidth of terahertz reflectarrays for various wavefront control functions.

3.1 Introduction

Wavefront control, also known as beamforming, is a process to customise field distributions in the near- or far-field (Al-Naib and Withayachumnankul, 2017; Headland *et al.*, 2017; Headland *et al.*, 2018a). Representative wavefront control functionalities include beam focusing (Headland *et al.*, 2016a; Yang *et al.*, 2017; Chang *et al.*, 2017), polarisation-dependent beam splitting (Niu *et al.*, 2014; Lee *et al.*, 2018b), beam deflection (Niu *et al.*, 2013), Bessel-beam generation (Meng *et al.*, 2014; Monnai *et al.*, 2015) and contoured beam synthesis (Zhou *et al.*, 2013, 2014). These operations are of particular significance to the terahertz regime, as they provide various radiation characteristics desired by emerging applications. For example, wavefront control techniques can be exploited for increasing antenna directivity and suppressing sidelobes. These characteristics are of importance for establishing point-to-point terahertz communications links. Conventional beamformers include lenses, parabolic mirrors, leaky-wave antennas (Tavallaee *et al.*, 2011), phased arrays (Sun *et al.*, 2013), and diffraction optics (Headland *et al.*, 2016b). As an alternative, metasurfaces can be applied for wavefront control as they feature flat profile, high efficiency, light weight, and low manufacturing complexity (Azad *et al.*, 2017).

Metasurfaces as the two-dimensional counterpart of metamaterials have been widely adopted in the terahertz region to control the magnitude, phase, and polarisation state of a reflected or transmitted beam (Luo, 2018; Jeong *et al.*, 2018; Wu *et al.*, 2019). One category of devices that is broadly related to metasurfaces is the reflectarray, which is an array of grounded resonators that locally alter the phase profile of an incident beam on reflection to form a predefined radiation pattern (Chen *et al.*, 2016a; Headland *et al.*, 2018a). The phase imposed to the reflected wave can be controlled at subwavelength scale by varying the geometrical parameters of each resonator. Typically, a complete phase coverage of 360° introduced by the resonators is necessary and a larger phase range can be obtained by employing phase wrapping. The main challenge associated with reflectarrays is their limited bandwidth performance that typically cannot go beyond 10.0% for moderate-size reflectarrays and even becomes narrower for larger reflectarrays (Huang and Encinar, 2007). Primarily, two factors contribute to this narrowband performance: First, the limited bandwidth of the resonant elements sets an intrinsic limit to the reflectarray operation. Second, the frequency-dependent spatial phase delay originating from the varying path lengths from the feed to each resonator on the reflectarray further restricts the bandwidth performance (Huang and Encinar, 2007).

It is however, possible to mitigate the first factor of limited resonator bandwidth. As illustrated in Figure 3.1, a broadband reflectarray is expected to present two distinctive features: the phase response curve of the resonator should vary smoothly and linearly as a function of one geometrical parameter, while on the other hand, the phase curves at different frequencies are supposed to be ideally parallel to each other with a constant gradient (Niu, 2015). An ideal phase profile that shows perfect linearity provides an equal phase difference at different frequencies so that the bandwidth can be improved. In the microwave community, overcoming the first bandwidth limiting factor led to intensive investigations, resulting in the development of topologies, such as aperture-coupled patches (Carrasco *et al.*, 2006; Carrasco *et al.*, 2007), stacked patches (Chaharmir *et al.*, 2003), multi-cross loop elements (Chaharmir *et al.*, 2010), parasitic dipoles (Li *et al.*, 2009), and various other novel elements (Chen *et al.*, 2012; Chen *et al.*, 2013a; Qu *et al.*, 2016). Among these reported studies, some employ multi-layer resonators, which are difficult to scale for fabrication at terahertz frequencies. For reported single-layer resonators, the linearity of the phase response curves requires further improvement and such structures exist only at microwave and millimetre wave frequencies.

In this Chapter, a reflectarray unit cell based on a single-layer stub-loaded resonator is presented for wideband operation. Relying on the concept of true-time delay, the proposed unit cell is capable of offering a smooth and near-linear phase response as a function of stub length, with a tunability range exceeding 360°. As a proof-of-concept,

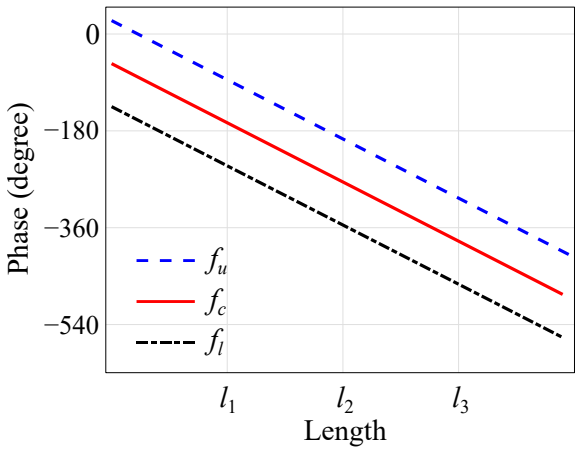

Figure 3.1. Ideal phase response of a broadband reflectarray. Ideal phase response characteristics of a broadband reflectarray at three different frequencies. Here, f_l, f_c, and f_u represent the lower, centre, and upper operation frequencies, respectively. The length is an abstract parameter representing one of the geometrical features of the resonator.

the designed unit cell is then exploited for constructing a terahertz reflectarray to focus an incident collimated beam into a point at a focal length of F = 150 mm. The performance of the reflectarray has been experimentally verified. It is noted that this bandwidth-enhanced focusing reflectarray design is only chosen as an illustrative example, and that the proposed unit cell has a potential to be configured for other beamforming functionalities.

3.2 Unit cell design

Figure 3.2 shows the proposed unit cell consisting a top resonator, a cyclic olefin copolymer (COC) spacer with a relative permittivity of $\epsilon_r = 2.33$ (Nielsen *et al.*, 2009) and loss tangent of $\tan\delta = 0.0007$ at ∼1.00 THz (Peytavit *et al.*, 2011), and a gold layer as a ground plane. In order to avoid unwanted grating lobes, the lattice constant is chosen as a = 120 μm, which corresponds to $0.4\lambda_0$ at the design frequency of 1.00 THz. The top resonator takes the form of a recessed square patch connected to four stubs working as phase delay lines. The recesses are implemented to realise impedance matching between the patch and stubs while T-junctions and stub bends are employed to prevent intersections of neighbouring stubs when their lengths l exceed 32 μm. The width of stubs is chosen as 5 μm based on the resonator efficiency and phase coverage performance. Simulations reveal that narrower stubs degrade the efficiency, while wider ones reduce the phase coverage. Additionally, chamfers of 5 μm are deployed to reduce the reflections introduced by the bends. The dielectric spacer thickness t_s is determined to

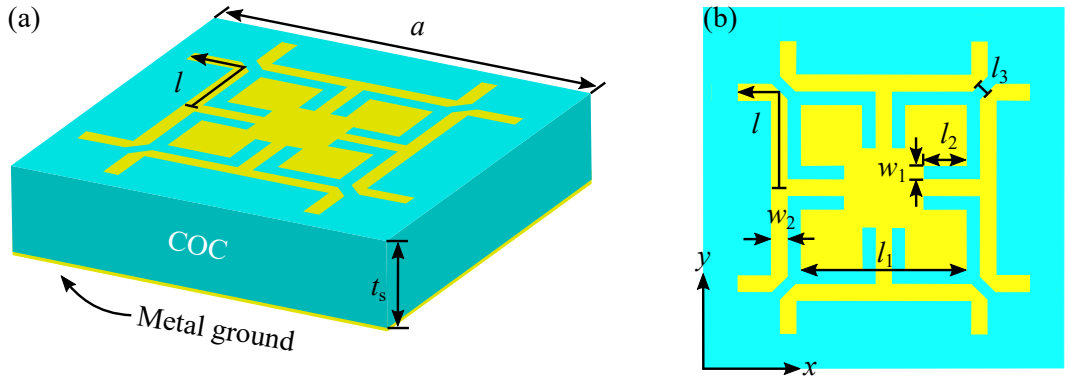

Figure 3.2. Unit cell geometry. (a) 3D view, and (b) top view. The detailed dimensions are as follows: a = 120 μm, t_s = 36 μm, l_1 = 55 μm, l_2 = 14.5 μm, $l_3 = 3\sqrt{2}$ μm, $w_1 = w_2$ = 5 μm, and l denotes the varying stub length.

be 36 μm as an acceptable trade-off between resonator efficiency, phase linearity, and fabrication constraints.

In the proposed resonator, the surface currents are mainly concentrated on the T-junctions and stubs rather than on the square patch as illustrated in Figure 3.3, demonstrating the impedance matching functionality of the recesses. Electromagnetic simulations are carried out with the commercial software ANSYS HFSS. The Drude-based surface impedance of gold at terahertz frequencies is used for computation (Lucyszyn, 2007).

The operation principle of the proposed reflectarray can be explained as follows. A plane wave illuminating the reflectarray surface couples with the stub-loaded square patches. The coupled wave travels along the corresponding pair of stubs, depending on polarisation, and gets reflected at their end. Subsequently, the reflected wave is re-radiated by the square patch with a phase delay that is roughly proportional to twice of the stub length (Huang and Encinar, 2007). Consequently, changing the length of the stubs alters the reflection phase accordingly. As illustrated in Figure 3.4, a smooth and near-linear reflection phase response with a maximum reflection loss of 1.5 dB at 1.00 THz can be achieved over the stub lengths of interest under a normally incident x-polarised excitation. Due to the symmetrical nature of the proposed structure, the reflection response of the unit cell is polarisation-independent under normal incidence. Phase curves with reasonable linearities at 0.90 THz and 1.10 THz are obtained, and importantly, the three phase curves are nearly parallel to each other as intended,

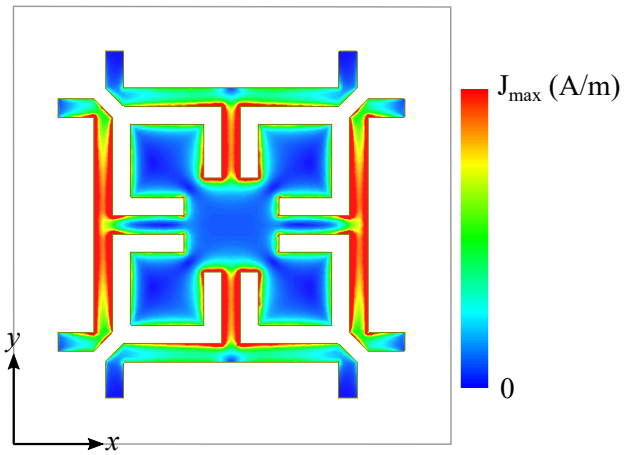

Figure 3.3. Top resonator surface currents distribution. Surface currents distribution on the top resonator under a normally-incident y-polarised excitation at 1.00 THz with $l = 44.5$ μm. The current is in linear scale and the outline box defines the unit cell size.

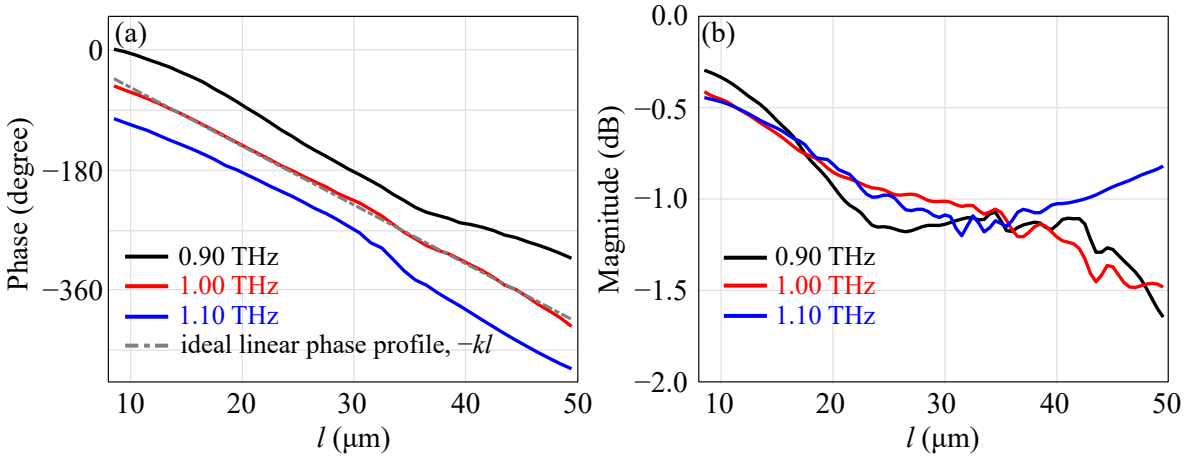

Figure 3.4. Simulated reflection responses under normal incidence. Simulated reflection responses under normal incidence against stub length l at frequencies of 0.90 THz, 1.00 THz, and 1.10 THz. (a) Reflection phases and (b) reflection magnitudes.

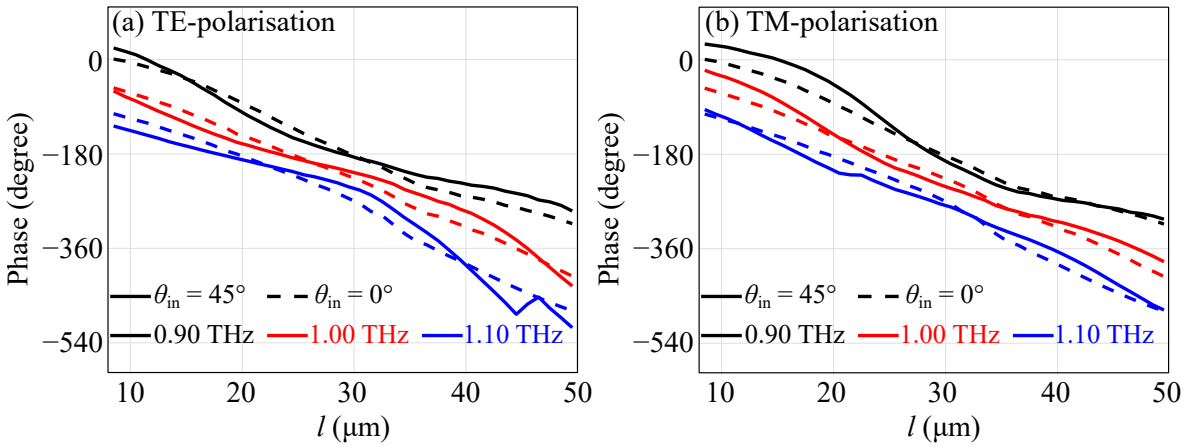

Figure 3.5. Simulated reflection phase responses under normal and oblique incidences. Simulated reflection phase responses against stub length l under normal and oblique incidences at 0.90 THz, 1.00 THz, and 1.10 THz. (a) TE-polarisation and (b) TM-polarisation. Solid lines are for oblique incidences with an angle of 45°, and dashed lines are for normal incidences.

demonstrating the potential of the elements for bandwidth enhancement. Moreover, Figure 3.5 indicates that the reflection phase responses of the proposed unit cell under an oblique incidence angle of 45° for both the transverse electric (TE)- and transverse magnetic (TM)-polarisations still show close agreement with the normal incidence case across three frequencies. This weak phase dependence on the incident angle is a result from the compact patch dimension ($l_1 = \sim 0.2\lambda_0$ at 1.00 THz) that leads to a limited phase difference between the patch edges when illuminated by an obliquely incident plane wave.

3.3 Array-level design

To demonstrate the performance of the designed unit cell, a reflectarray is constructed to transform a collimated beam into a focused beam. Each resonant element on the reflectarray surface is tailored to introduce an appropriate phase shift depending on its specific location. In accordance with Figure 3.6, the incident beam is set to an angle of $\theta = 45°$, $\phi = 0°$, while the reflected beam is determined to be focused at a point that is 150 mm away from the reflectarray centre towards the direction defined by $\theta = 45°$, $\phi = 180°$. The required phase delay introduced by each resonant element to realise beam focusing can be described as (Huang and Encinar, 2007; Headland *et al.*, 2018a)

$$\varphi(x_i, y_i) = k_0(d_i - (x_i \cos\phi + y_i \sin\phi)\sin\theta) + \varphi_0, \tag{3.1}$$

where k_0 denotes the wavenumber in free-space, d_i represents the distance between the focal spot and the centre of the i^{th} element located at (x_i,y_i,0) in the Cartesian coordinates, and φ_0 is the phase offset. Figure 3.7(a) illustrates the required phase distribution across the reflectarray surface and it is wrapped to 360°. The stub length distribution on the reflectarray surface can then be determined from the desired phase distribution across the surface calculated by Equation (3.1) and the relationship between the stub length and phase response at 1.00 THz as shown in Figure 3.4(a). Taking the fabrication feasibility into consideration, the stub length distribution is quantized into 42 levels from 8.5 μm to 49.5 μm with 1 μm increments, as shown in Figure 3.7(b).

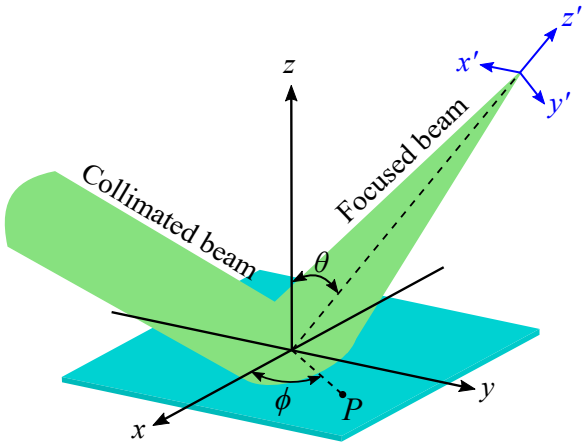

Figure 3.6. Reflectarray focusing operation. A collimated beam impinges on the reflectarray surface with an incidence angle of $\theta = 45°$, $\phi = 0°$, and converges to a point after interacting with the reflectarray, toward a direction given by $\theta = 45°$, $\phi = 180°$. Point P is randomly chosen on the reflectarray surface for illustration purpose.

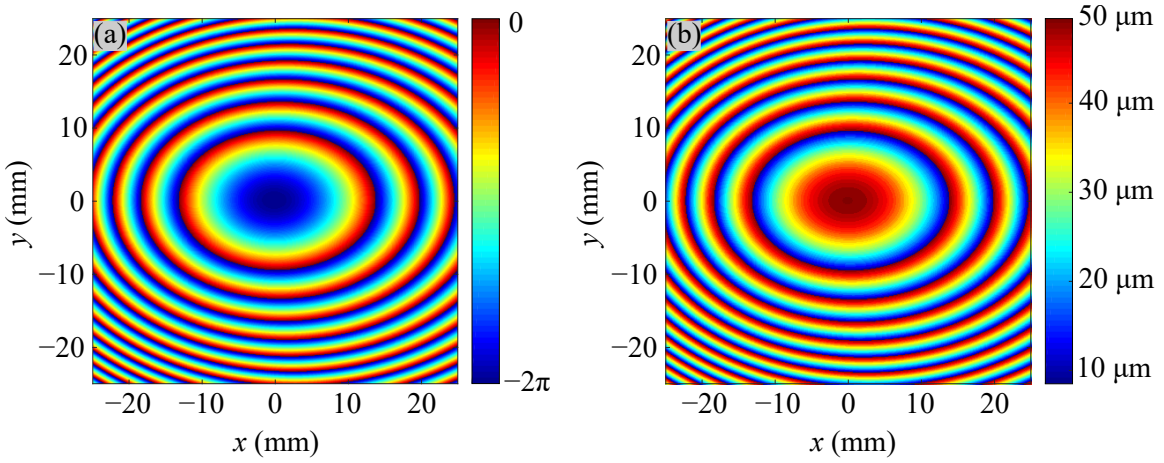

Figure 3.7. Distributions of desired phase response and stub length on the reflectarray surface for beam focusing. (a) Phase distribution and (b) stub length distribution.

In order to gain an insight into the focusing capability of the constructed reflectarray, a numerical calculation involving the Huygens-Fresnel principle is employed (Goodman, 2005). Due to the fact that a Gaussian beam cannot be of infinite extent in reality, beam aperture truncation is then applied. Since the lens employed in the experiment has a radius of 17 mm, a collimated beam excitation is represented in the calculations as a 2D Gaussian function, where the beam waist and truncation radius are equal to 17 mm. The calculated field distribution of the reflected beam for the TM-polarisation converges along the propagation z'-axis to a focal point that migrates as a function of frequency as shown in Figure 3.8. It is observed that the reflected beam magnitude at 1.00 THz

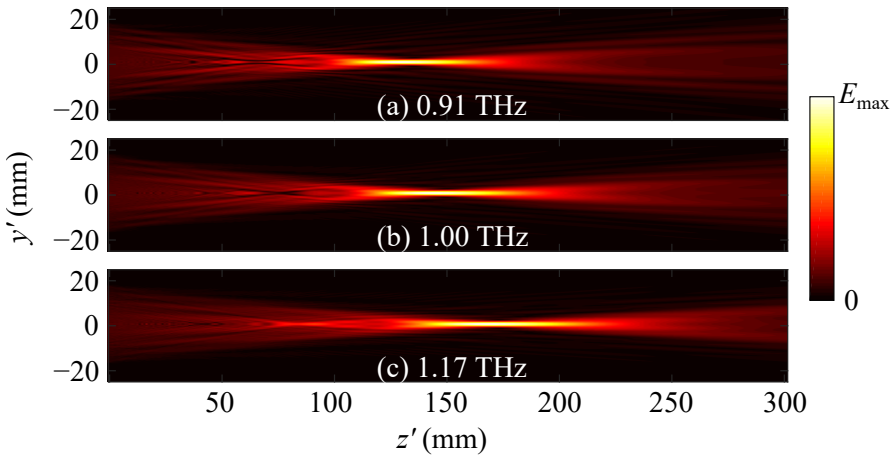

Figure 3.8. Frequency-dependent beam focusing operations. Calculated linear field distributions along propagation with a TM-polarised plane wave excitation at (a) 0.91 THz, (b) 1.00 THz, and (c) 1.17 THz.

is maximal at a focal length of $F = 150$ mm as intended. Further calculations for the TE-polarisation show comparable results with the TM-polarisation. Thus, the focusing capability of the proposed reflectarray is numerically verified.

3.4 Fabrication

A sample was fabricated by the Functional Materials and Microsystems Research Group and the Micro Nano Research Facility at RMIT University. The reflectarray is realised by commencing with a 200 nm thick gold (Au) layer deposited onto a standard 3 in. silicon (Si) wafer as a ground plane using electron beam evaporation (PVD75, Kurt J. Lesker). To realise better adhesion to the substrate, a 20 nm thick layer of chromium (Cr) is deposited prior and after the Au layer as illustrated in Figure 3.9(a). The Cr/Au/Cr coated wafer is then cleaned using standard cleanroom cleaning process with acetone, isopropyl alcohol and water followed by dehydration at 120 °C for 5 min. As depicted in Figure 3.9(b), to realise the dielectric layer, COC mr-I T85-5.0 and mr-I T85-20.0 are spun (Laurell spinner 650M) sequentially onto the ground plane at 3000 rpm for 30 s each to achieve a thickness of 36 $\pm$ 1 µm, measured with a stylus profilometer (Dektak XT - Bruker). The COC is dehydrated by ramping the temperature to 145 °C for 15 min on a hot plate, after every spin. Standard photolithography using UV exposure techniques (SUSS MA6 Mask Aligner/BS Alignment) with AZ5214E as the photoresist is employed to design patterns of the resonators on the COC dielectric layer. This is followed by a 20/200 nm Cr/Au deposition and resist dissolution (lift-off) in acetone, as shown in

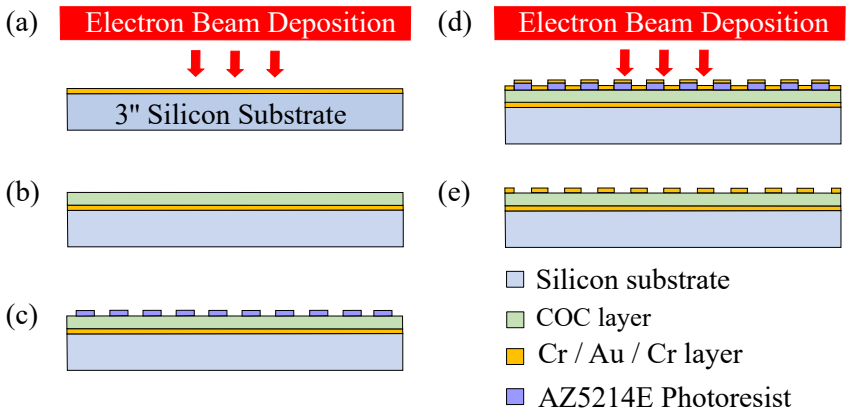

Figure 3.9. Fabrication process. (a) Electron beam deposition of Cr/Au/Cr on standard 3 in. silicon substrate, (b) spin-coating of COC onto substrate, (c) photolithography of reflectarray resonator patterns, (d) electron beam deposition of Cr/Au, and (e) lift-off process to achieve the gold resonators.

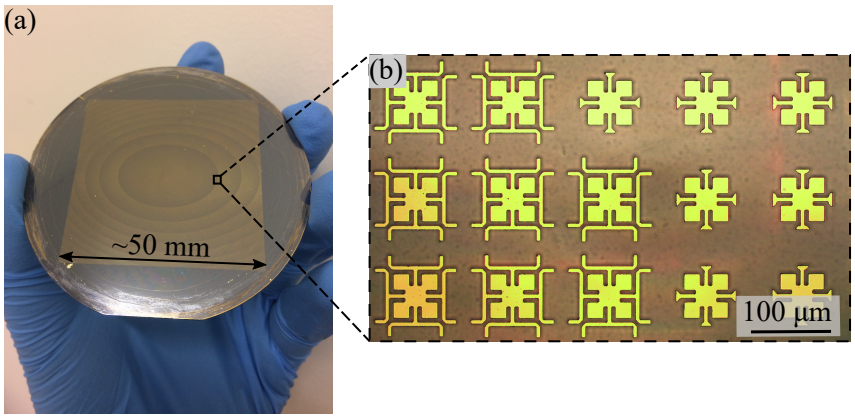

Figure 3.10. Reflectarray prototype. (a) Photograph of the fabricated sample, and (b) partial view of the reflectarray.

Figure 3.9(e). Images of the fabricated sample are shown in Figure 3.10. The fabricated reflectarray has a size of around 50 × 50 mm^2, corresponding to 416 × 416 elements across the reflectarray surface.

3.5 Measurement

A fibre-coupled terahertz time-domain spectroscopy (THz–TDS) system is employed to characterise the field profiles of the focal spot and the related quantities such as bandwidth and efficiency. The experimental setup is illustrated in Figure 3.11. A polymethylpentene (TPX) lens with a radius of 17 mm collimates the terahertz beam emerging from the source. The collimated beam (see Appendix B) obliquely impinges on the sample with an incidence angle of 45° and is then reflected towards the receiver. The

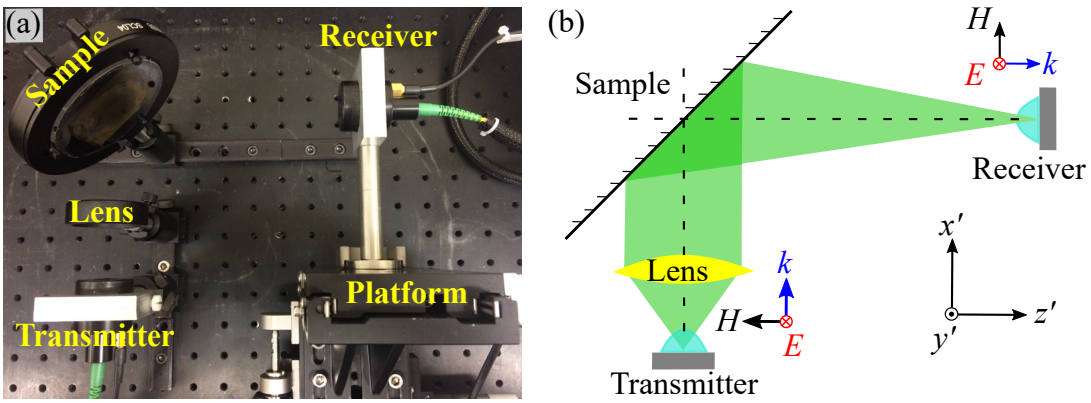

Figure 3.11. Focusing reflectarray characterisation. (a) Reflecctarray experimental setup, and (b) simplified schematic of the reflectarray characterisation setup.

receiver is mounted on a platform to raster scan the field profile of the focal spot in the $x'y'$-plane that is 150 mm away from the reflectarray centre. The overall scanning area is 6×6 mm^2 with a spatial resolution of 80 µm. The TE- or TM-polarisation can be obtained by rotating both the source and detector around their own axes.

Evaluation of the efficiency requires a reference measurement for normalisation. In this regard, an off-axis parabolic mirror is employed that has the same focal length and aperture size as the proposed reflectarray. This off-axis parabolic mirror replaces the sample in the experiment setup shown in Figure 3.11.

3.6 Results

The calculated and measured magnitude profiles of the focal spot at 1.00 THz for the TE- and TM-polarisations are given in Figure 3.12. A well-defined beam spot can be observed from the calculated and measured field amplitude distributions. Specifically, Table 3.1 shows the details of the calculated and measured beam waists of the focal spot at 1.00 THz, and thus close agreement is demonstrated.

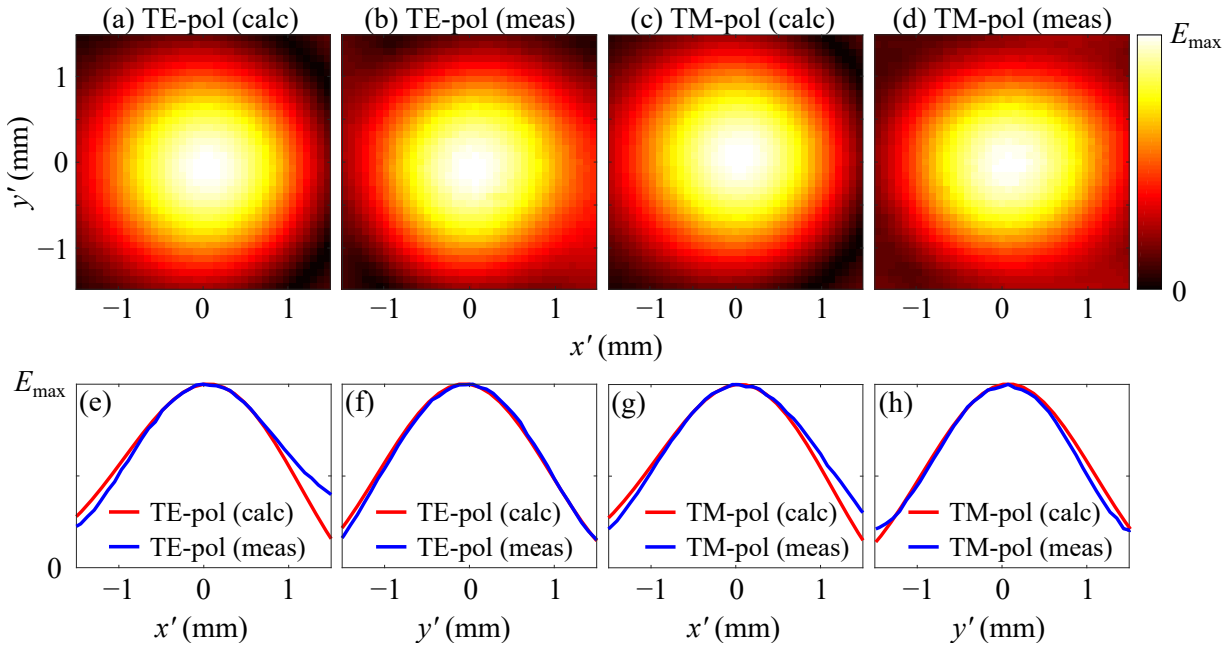

Figure 3.12. Linear beam profiles across the focal spot at 1.00 THz. [(a, b)] Calculated and measured field magnitude profiles with a TE-polarised excitation. [(c, d)] Calculated and measured field magnitude profiles with a TM-polarised excitation. [(e-h)] Linear transverse magnitudes corresponding to [(a-d)]. Both calculated and measured magnitudes are normalised to their own maxima.

Table 3.1. Beam waist comparison. Beam waists of the calculated and measured focal spot at 1.00 THz. The units are in mm.

	TE-polarisation		TM-polarisation	
	x'-axis	y'-axis	x'-axis	y'-axis
Calculation	1.3	1.2	1.3	1.3
Measurement	1.4	1.2	1.2	1.2

The measured field magnitude distributions at different frequencies for the TE- and TM-polarisations are depicted in Figure 3.13. It is shown that a clearly-defined focal spot can be sustained from 0.91 to 1.15 THz and from 0.92 to 1.17 THz for the TE- and TM-polarisations, respectively. Due to the fact that the beam waist is roughly proportional to the wavelength, the focal spot is expected to decrease when the operation frequency increases (Headland *et al.*, 2016a). However, the measured focal spot size is slightly increased when the operation frequency goes beyond 1.00 THz. This deviation can be ascribed to beam squint effect resulting from the frequency-dependent phase shift across the reflectarray surface (Targonski and Pozar, 1996). Moreover, the imperfection of the input collimated beam, whose calculated Gaussicity is 3.4% at 1.00 THz, also contributes to the discrepancy. Aberration effects are visible around the focal spots as shown in Figure 3.13. They are likely caused by rotational misalignment (Headland, 2017), i.e., the collimated beam incidence angle is slightly deviating from the predefined

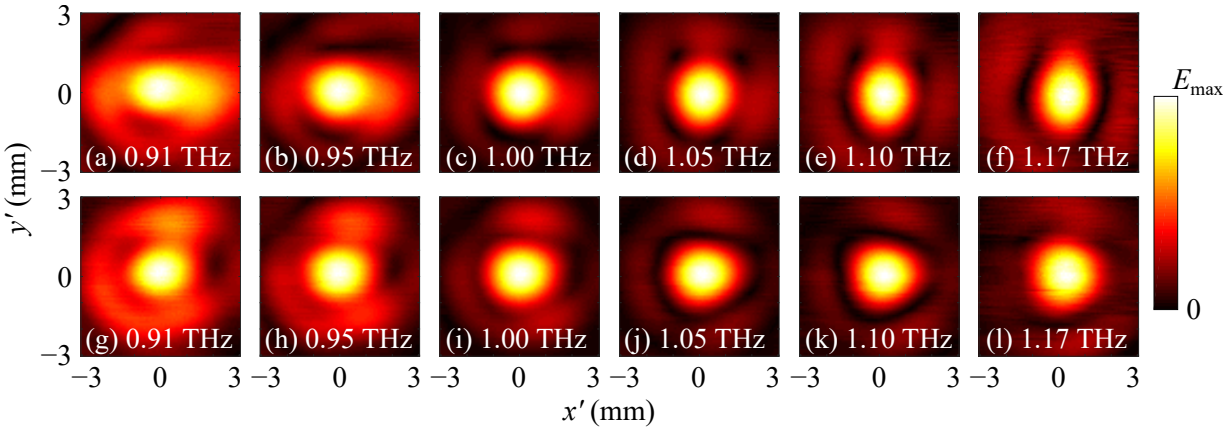

Figure 3.13. Linear magnitude profiles of the focal spot at different frequencies. [(a-f)] TE-polarisation, and [(g-l)] TM-polarisation. The measurements are taken at the fixed focal plane of $F = 150$ mm, and these beam profiles are normalised to their own maxima.

45°. The concentric rings around the focal spot known as Airy patterns can also be seen from Figure 3.13, resulting from the beam truncation.

Two important measures of the unit cell design are bandwidth and efficiency. This information can be inferred from the focusing capability of the reflectarray. The 3-dB bandwidth is calculated based on a single-pixel measurement of the frequency-dependent field power taken at the maximum field amplitude of the focal spot, $F = 150$ mm. As shown in Figure 3.14, the measured results reveal the 3-dB fractional bandwidths of 23.3% for the TE-polarisation and 23.9% for the TM-polarisation, within the range of 0.91 to 1.15 THz and 0.92 to 1.17 THz, respectively. Further simulations reveal that the proposed reflectarray exhibits over twice 3-dB simulation bandwidth compared with focusing reflectarrays formed by two existing resonator designs at terahertz frequencies (Niu *et al.*, 2013; Headland *et al.*, 2016a). In addition, the proposed reflectarray shows an improved measurement bandwidth compared with the measured 18.0% of a dielectric resonator reflectarray at the same efficiency (Headland *et al.*, 2016a).

The efficiency of the device can be estimated by integrating the total power over the focal plane of the proposed reflectarray and comparing the result with the corresponding power delivered by a reference off-axis parabolic mirror with the same aperture size and focal length. Figure 3.15 shows the measured efficiencies of the manufactured reflectarray for the TE- and TM-polarisations. It can be seen that the measured efficiency at the design frequency of 1.00 THz is 71.9% for the TE-polarisation and 71.0% for the TM-polarisation, and the highest efficiencies appear at 0.96 THz as 74.6% for the

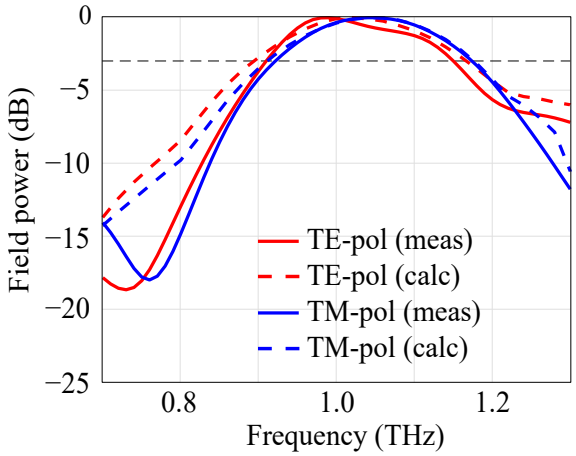

Figure 3.14. Focusing reflectarray bandwidth. Bandwidth of the reflectarray estimated based on the peak field power at the fixed focal spot that is 150 mm away from the reflectarray centre. Both calculated and measured results are normalised against their own maxima. The black dashed line denotes the −3 dB threshold.

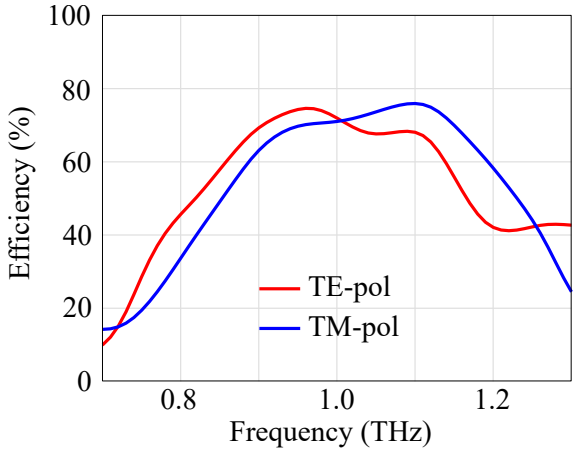

Figure 3.15. Measured efficiency of the focusing reflectarray. The efficiency is calculated by normalising the integrated power over the focal plane delivered by the reflectarray with that imparted by a reference off-axis parabolic mirror with the same aperture size and focal length.

TE-polarisation and 1.10 THz as 75.9% for the TM-polarisation. However, the dielectric resonator reflectarray exhibits a higher maximum measured efficiency from 0.99 THz to 1.16 THz compared with the proposed reflectarray, resulting from the low loss of dielectric resonators.

It is worth noting that metallic resonators are employed for the proposed unit cell design as they offer low profile and reduced fabrication complexity compared with dielectric resonators. However, metallic-resonator reflectarrays typically suffer from non-negligible conductor loss at terahertz frequencies (Headland *et al.*, 2015; Walia *et al.*, 2015). In contrast, dielectric resonators possess an advantage of being low loss, i.e. they can attain higher radiation efficiency. The main concerns when employing dielectric resonators are an increased manufacturing complexity and the strong mutual coupling between neighbouring dielectric resonators resulting from their non-negligible thicknesses (Headland *et al.*, 2017). Importantly, achieving linear phasing with dielectric resonators is challenging.

3.7 Conclusion

We propose a unit cell based on a single-layer stub-loaded resonator that can provide a smooth and near-linear phase response. The proposed unit cell has a potential to construct beamformers with enhanced bandwidth. A focusing reflectarray has been presented as a platform to demonstrate the performance of this proposed unit cell. The focusing capability of the constructed reflectarray has been experimentally verified,

showing a measured 3-dB relative bandwidth of 23.3% for the TE-polarisation spanning from 0.91 THz to 1.15 THz, and 23.9% for the TM-polarisation ranging from 0.92 THz to 1.17 THz. The reflectarray bandwidth can be further enhanced independently of the resonant element by employing a phase synthesis approach (Mao *et al.*, 2015). The constructed reflectarray can also transform an incident spherical wave into a collimated beam in accordance with the reciprocity theorem. Potential applications of the designed unit cell include terahertz communications, sensing and imaging. The proposed unit cell could also serve as a basic building element to realise dynamic scanning provided that a tuning mechanism is added to the stubs.

Chapter 4

Semi-analytical approach for broadband transmitarray design

In order to harness the capabilities of terahertz waves, various transmitarray-based devices have been developed recently. However, due to the absence of systematic optimisation methodologies, most existing designs leave room for further performance improvement. To facilitate the transmitarray design and optimisation, a broadband semi-analytical approach is developed on the basis of an existing narrowband methodology. The broadband approach incorporates network analysis and genetic algorithm to determine the optimal frequency-independent circuit parameters for transmitarrays, so that pre-specified transmission coefficients can be achieved over a wide bandwidth. As a proof-of-concept, a terahertz antireflection transmitarray is rigorously designed based on this approach. Simulation results indicate that the proposed transmitarray can effectively suppress the reflection at an air-silicon interface to a level below −20 dB from 203 GHz to 357 GHz at normal incidence, with a transmission efficiency above 96.1%. Moreover, further simulations suggest that the presented antireflection transmitarray is robust to obliquely incident waves. The broadband design approach is capable of configuring diverse transmitarrays for wavefront control and polarisation manipulation.

4.1 Introduction

This Chapter introduces a broadband semi-analytical approach for transmitarray designs in Section 4.2, which is an extension of the method presented by Pfeiffer and Grbic (Pfeiffer and Grbic, 2014). The original method targets optimal performance with a limited bandwidth. The broadband approach incorporates network analysis and genetic algorithm, in which the network analysis investigates the scattering characteristics of anisotropic transmitarrays, while the genetic algorithm determines the optimal circuit parameters to attain the desired transmission coefficients over a wide bandwidth.

In order to illustrate and verify the functionality of the broadband approach, Section 4.3 presents an antireflection transmitarray that is rigorously designed based on this approach. As a result of the systematic optimisation procedure, the presented antireflection transmitarray mitigates reflection and enhances transmission at an air-silicon interface over a wide bandwidth. The broadband approach presented in this Chapter provides a way to realise various wideband and highly efficient terahertz transmitarrays for wavefront control and polarisation manipulation, and some representative devices will be proposed and demonstrated with experimental validation in Chapters 5 – 7.

4.2 Broadband semi-analytical approach

To begin with, we consider a transmitarray cascading three metallic layers separated by two dielectric spacers made of the same material as illustrated in Figure 4.1. For each metallic layer, we can choose an anisotropic pattern that exhibits distinctive equivalent

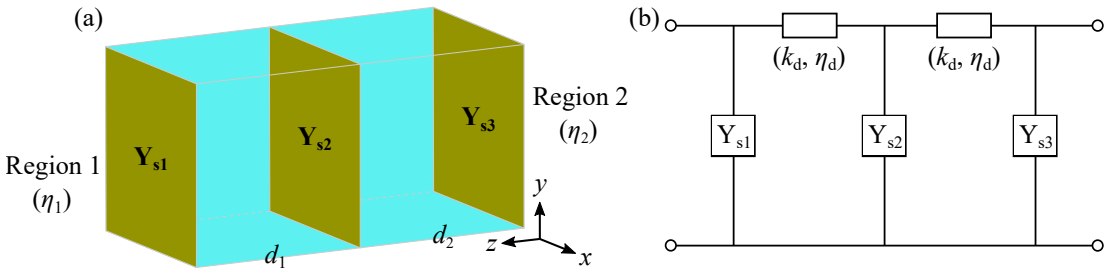

Figure 4.1. Schematic illustration of a transmitarray unit cell and its equivalent circuit model along one polarisation. (a) Transmitarray comprises three metallic layers and two subwavelength dielectric spacers made of the identical material. (b) Equivalent circuit model of the transmitarray under one specific polarisation. The transmitarray is hosted in between Regions 1 and 2, whose impedances are denoted as η_1 and η_2, respectively. The wavenumer and wave impedance of the dielectric spacer are represented as k_d and η_d, respectively.

LC circuit behaviors along the x- and y-axes. Here, we select an anisotropic pattern with equivalent parallel LC circuits as an illustrative example, but this pattern could also be in other forms including equivalent series LC circuit or purely inductive or capacitive circuits. For simplicity, it is assumed that all metals employed are lossless at this stage, thus the admittance tensor of each metallic layer is purely imaginary. Based on the assumptions above, the admittance tensor of an i^{th} metallic layer can be written as

$$\mathbf{Y_{si}} = \begin{bmatrix} \dfrac{1}{j\omega L_{\text{x}i}} + j\omega C_{\text{x}i} & 0 \\ 0 & \dfrac{1}{j\omega L_{\text{y}i}} + j\omega C_{\text{y}i} \end{bmatrix}, \tag{4.1}$$

where $(L_{\text{x}i}, C_{\text{x}i})$ and $(L_{\text{y}i}, C_{\text{y}i})$ are the pattern-equivalent inductance and capacitance along the x- and y-axes, respectively. The off-diagonal terms are equal to zero, indicating that there is no cross-coupling introduced by the pattern. Note that the analytical approach presented by Pfeiffer and Grbic (2014) solved for the optimal admittance at the design centre frequency, thus resulting in narrow-bandwidth designs. Moreover, the optimal admittance at the frequency of interest can be physically realised by a vast number of (L, C) combinations, and hence diverse metallic patterns. Nevertheless, only very few metallic patterns are capable of providing a large bandwidth and enhanced efficiency. Hence, here the frequency-dependent admittance is decomposed into the frequency-independent inductance and capacitance, so as to numerically explore the transmitarray dispersive performance within the frequency band of interest. The transfer matrix method is implemented to describe the scattering property of the mentioned anisotropic transmitarray configuration, which comprises three metallic layers separated by two subwavelength dielectric spacers. These dielectric spacers can be modeled as transmisson lines along the z-axis. Hence, the total 4×4 **ABCD** transfer matrix of the transmitarray is given by (Pfeiffer and Grbic, 2014)

$$\begin{aligned} \begin{bmatrix} \mathbf{A} & \mathbf{B} \\ \mathbf{C} & \mathbf{D} \end{bmatrix} = &\begin{bmatrix} \mathbf{I} & \mathbf{0} \\ \mathbf{nY_{s1}} & \mathbf{I} \end{bmatrix} \begin{bmatrix} \cos(k_{\text{d}}d_1)\mathbf{I} & -j\sin(k_{\text{d}}d_1)\eta_{\text{d}}\mathbf{n} \\ j\sin(k_{\text{d}}d_1)\eta_{\text{d}}^{-1}\mathbf{n} & \cos(k_{\text{d}}d_1)\mathbf{I} \end{bmatrix} \\ &\begin{bmatrix} \mathbf{I} & \mathbf{0} \\ \mathbf{nY_{s2}} & \mathbf{I} \end{bmatrix} \begin{bmatrix} \cos(k_{\text{d}}d_2)\mathbf{I} & -j\sin(k_{\text{d}}d_2)\eta_{\text{d}}\mathbf{n} \\ j\sin(k_{\text{d}}d_2)\eta_{\text{d}}^{-1}\mathbf{n} & \cos(k_{\text{d}}d_2)\mathbf{I} \end{bmatrix} \\ &\begin{bmatrix} \mathbf{I} & \mathbf{0} \\ \mathbf{nY_{s3}} & \mathbf{I} \end{bmatrix}, \end{aligned} \tag{4.2}$$

where $\mathbf{I}$ = [1 0;0 1] denotes the identity matrix and $\mathbf{n}$ = [0 −1;1 0] represents the 90° rotation matrix. The wavenumber and wave impedance of the dielectric spacer are

denoted by k_d and η_d, respectively, while d_1 and d_2 are the dielectric spacer thicknesses. Each element in the final **ABCD** matrix is a 2×2 tensor corresponding to the x- and y-polarisations. It should be emphasised that here only propagating modes are accounted for. Evanescent modes resulting from the near-field coupling are assumed to be negligible, which is a valid approximation provided that electrically large spacings between the metallic layers are adopted. A small unit cell size together with a reasonably large layer spacing are beneficial to the accuracy of the analytical model (Pfeiffer and Grbic, 2014). Once the **ABCD** matrix is established, the S-parameters of the anisotropic transmitarray under linearly polarised incident waves at normal incidence can be written as

$$\begin{bmatrix} \mathbf{S}_{11} & \mathbf{S}_{12} \\ \mathbf{S}_{21} & \mathbf{S}_{22} \end{bmatrix} = \begin{bmatrix} -\mathbf{I} & \frac{\mathbf{Bn}}{\eta_2} + \mathbf{A} \\ \frac{\mathbf{n}}{\eta_1} & \frac{\mathbf{Dn}}{\eta_2} + \mathbf{C} \end{bmatrix}^{-1} \begin{bmatrix} \mathbf{I} & \frac{\mathbf{Bn}}{\eta_2} - \mathbf{A} \\ \frac{\mathbf{n}}{\eta_1} & \frac{\mathbf{Dn}}{\eta_2} - \mathbf{C} \end{bmatrix}, \tag{4.3}$$

where **S** is a 2×2 tensor for the x- and y-polarisations, while η_1 and η_2 are the wave impedances of Regions 1 and 2, respectively. At this stage, the S-parameters of the anisotropic transmitarray for two orthogonal linear polarisations can be readily calculated based on the equivalent inductances and capacitances of each metallic layer. Conversely, a stipulated S-parameter specification can be obtained by implementing a genetic algorithm to determine the optimal circuit parameters fitting the requirements. Specifically, the genetic algorithm starts from an initial group that consists of various individuals with genes formed by circuit parameters. Since the circuit parameters implemented here are frequency-independent, the scattering characteristics of the transmitarray can then be numerically investigated over the frequency range of interest using Equations (4.1)-(4.3). Thus, the fitness of each parameter set is evaluated based on its scattering characteristics using an application-defined cost function. As such, the optimal circuit parameters are eventually selected to collectively achieve a transmission performance that closely approximates the objectives over the targeted frequency band.

Once the optimal inductances and capacitances are determined, their physical realisations can be implemented by designing specific metallic patterns. To realise each metallic layer, the simulation starts from a pattern with arbitrary dimensions but with equivalent circuits along the x- and y-axes are predominately parallel LC circuits. The pattern is then evolved to reproduce the optimal circuit parameters provided by the broadband semi-analytical approach. The metallic pattern equivalent inductance and capacitance along the x- or y-polarisation can be calculated based on the simulated admittances. For each metallic layer, the corresponding admittance tensor can be extracted

from the simulated reflection coefficients by (Pfeiffer and Grbic, 2014)

$$\mathbf{Y_s} = \left[\frac{\mathbf{I} - \mathbf{S_{11}}}{\eta_1'} - \frac{\mathbf{I} + \mathbf{S_{11}}}{\eta_2'}\right][\mathbf{I} + \mathbf{S_{11}}]^{-1}, \tag{4.4}$$

where η_1' and η_2' are the wave impedances of the adjoining media. Hence, for each metallic layer and each polarisation, the two unknowns of (L, C) can be analytically solved by retrieving the Y-parameters at two different frequencies. The equivalent inductance and capacitance are then compared with the optimal values from the semi-analytical approach, and the metallic pattern is altered accordingly until the obtained simulated values match the optimal ones. Note that the physical realisations of the three metallic layer are carried out separately.

4.3 Terahertz antireflection transmitarray

Owing to the advantages of high transparency and ultra-low dispersion, some dielectric materials such as high-resistivity silicon have been widely utilised for various components, for example, antennas (Headland *et al.*, 2018b; Withayachumnankul *et al.*, 2018), windows (Wagner-Gentner *et al.*, 2006), waveguides (Gao *et al.*, 2019; Yu *et al.*, 2019b; Headland *et al.*, 2019, 2020b; Gao *et al.*, 2021), beam splitters (Homes *et al.*, 2007), and lenses (Kononenko *et al.*, 2020; Headland *et al.*, 2020a). For silicon to function as terahertz windows, substrates, and lenses, one inherent challenge is the relatively high refractive index that leads to a strong Fresnel reflection at a silicon-air interface. Silicon exhibits a refractive index of 3.42 at terahertz frequencies (Dai *et al.*, 2004), resulting in a reflection magnitude as high as -5.2 dB or 30% of incident power at normal incidence. Hence, it is of significance to mitigate reflection at the air-dielectric interface to minimise the power loss in various systems.

Conventionally, quarter-wavelength antireflection coatings made of a single-layer dielectric film with a matched refractive index can be employed to reduce reflection in a narrow bandwidth. Their operation mechanism can be explained in term of destructive interference of electromagnetic waves at one wavelength, where waves reflected at an air-coating interface and coating-dielectric interface experience a phase difference of an odd multiple of 180°. To enhance bandwidth, multi-layer dielectric films with carefully selected refractive indices and thicknesses can be implemented for reflection reduction (Hosako, 2005). However, very few low-loss materials present the desired refractive

indices at terahertz frequencies. Alternative approaches to realising antireflection include surface relief structures (Brückner *et al.*, 2007) and all-dielectric moth-eye coatings (Yu *et al.*, 2019a), which have been shown to exhibit an improved bandwidth however at the cost of a complicated fabrication process.

In addition to the aforementioned methodologies, a myriad of transmitarray-based devices have been reported to function as antireflection coatings (Zhang *et al.*, 2014; Zhao *et al.*, 2018b; Pecora *et al.*, 2018). For instance, an antireflection transmitarray employing split-ring resonators and metal meshes exhibited a relatively strong robustness to obliquely incident waves, but merely enabled a reflectance below -20 dB under normal incidence over a fractional bandwidth of 5.2% (Chen *et al.*, 2010). To enhance bandwidth, a bi-layer transmitarray based on cross-resonators was presented and a -20-dB reflectance was demonstrated over a relative bandwidth of 21.9% (Huang *et al.*, 2017). There is a room for further performance improvement that could be achieved by enhancing the design process with a systematic optimisation approach.

In this Section, a wideband and highly efficient terahertz antireflection transmitarray is designed as a proof-of-concept for the broadband approach proposed in Section 4.2. The presented antireflection transmitarray is designed to cover the WR-3.4 waveguide frequency range from 220 GHz to 330 GHz (Hesler *et al.*, 2007), corresponding to a relative bandwidth of at least 40%. This frequency band of interest is designated for point-to-point terahertz communications (IEEE 802 LAN/MAN Standards Committee, 2017). The proposed transmitarray cascades three metallic layers that are separated by two dielectric spacers, and its isotropic response to incident waves at normal incidence can be described by using Equations (4.2)–(4.3). The broadband approach can facilitate the antireflection transmitarray design by providing optimal circuit parameters. Subsequently, physical realisations of the three metallic layers are carried out separately to reproduce their corresponding circuit parameters. Lastly, 3D full-wave simulations are conducted to evaluate the performance of the antireflection transmitarray.

4.3.1 Design

To minimise the reflection at an air-dielectric interface, we consider a transmitarray that comprises three metallic layers and two dielectric spacers as depicted in Figure 4.2. Here we employ silicon as the substrate for illustration purpose, and the substrate can be other dielectrics or semiconductors such as gallium arsenide, germanium, and indium tin oxide. A tri-layer structure promises more degrees of freedom than a single- or bi-layer

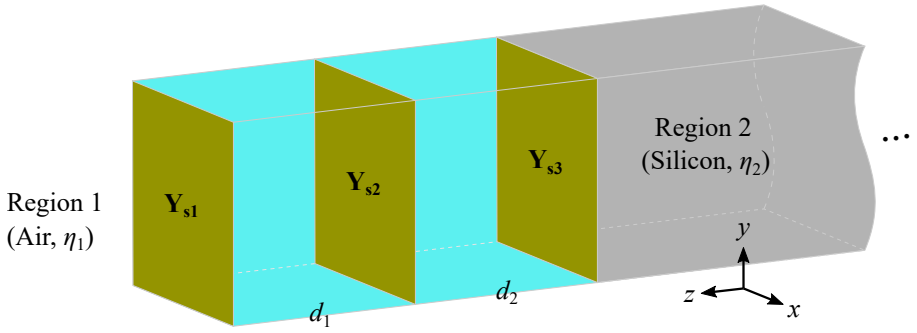

Figure 4.2. Schematic illustration of a tri-layer antireflection transmitarray unit cell bonded to a silicon substrate. The transmitarray is composed of three metallic layers that are separated by two dielectric spacers made of the same material, and it is hosted in between air and silicon. The considered high-resistivity silicon has a relative permittivity of $\epsilon_{si} = 11.68$ and loss tangent of $\tan\delta_{si} \approx 0.00002$ at terahertz frequencies (Dai *et al.*, 2004). The wave impedances of air and silicon are $\eta_1 = 377\ \Omega$ and $\eta_2 = 377/\sqrt{\epsilon_{si}}\ (\Omega)$, respectively.

design, so that the bandwidth can be broadened. In order to achieve a polarisation-insensitive response at normal incidence, a pattern of four-fold symmetry is expected for each metallic layer. Thus, the equivalent circuits of each metallic layer along the x- and y-polarisations are identical, and they can be parallel LC or series LC circuits. To illustrate the admittance tensor of each metallic layer, we assume here that the responses of an i^{th} metallic layer along the x- and y-axes can be described by an equivalent series LC circuit and its corresponding admittance tensor can be expressed as

$$\mathbf{Y_{si}} = \begin{bmatrix} \dfrac{1}{j\omega L_i + \dfrac{1}{j\omega C_i}} & 0 \\ 0 & \dfrac{1}{j\omega L_i + \dfrac{1}{j\omega C_i}} \end{bmatrix}, \tag{4.5}$$

where L_i and C_i are the pattern-equivalent inductance and capacitance along the x- or y-axis. To enhance efficiency, ultra-low loss cyclic olefin copolymer (COC) layers with a relative permittivity of $\epsilon_{coc} = 2.33$ and loss tangent of $\tan\delta_{coc} = 0.0005$ from 220 GHz to 330 GHz are implemented as dielectric spacers (Nielsen *et al.*, 2009). A spacer can be modeled as a transmission line section as indicated in Equation (4.2), while its wavenumber k_d and wave impedance η_d are determined based on the complex relative permittivity to account for its material loss. Consequently, the S-parameters of the whole structure can be calculated by inserting Equations (4.5) and (4.2) into Equation (4.3). Since the incident and reflected waves propagate in the same medium, hence the reflectance can be denoted as $\mathbf{R} = |\mathbf{S}_{11}|^2$. However, the incident and transmitted

waves travel in two different media, thus the transmittance under normal incidence in Region 2 can be expressed as $\mathbf{T} = |\mathbf{S}_{21}|^2 \left(\eta_1/\eta_2\right)$ (Hecht, 2002). It is noted that the reflectance $\mathbf{R}$ and transmittance $\mathbf{T}$ are both 2×2 tensors for the x- and y-polarisations.

In order to employ the semi-analytical approach to facilitate and optimise the transmitarray design, an objective is set for the device performance. We aim at designing an antireflection transmitarray that is capable of suppressing the reflection magnitude to be lower than -20 dB, while maintaining the transmission magnitude to a level above -0.5 dB from 220 GHz to 330 GHz. As a constraint, the achievable ranges of inductance and capacitance within a unit cell of a certain lattice constant are explored by employing 3D full-wave simulations, and the implemented patterns can be modeled as equivalent series LC circuits along the x- and y-polarisations. Furthermore, a COC thickness range from 50 μm to 200 μm is assigned, where the fabrication feasibility is accounted for. From an equivalent circuit model of the entire structure, the broadband approach is able to find the optimal frequency-independent circuit parameters of (L_i, C_i) for the i^{th} metallic layer and thickness profiles of (d_1, d_2) for the dielectric spacers. It is noted that parallel LC circuits have been attempted but their performance is inferior to series LC circuits for this application. Table 4.1 shows the optimal circuit parameters provided by this approach, while the optimal dielectric spacer thicknesses are $d_1 = 162$ μm and $d_2 = 57$ μm.

Once the optimal circuit parameters are determined, a pattern simulation is conducted to physically realise the corresponding circuit parameters for each metallic layer. Full-wave simulations are carried out with the commercial software ANSYS HFSS. Figures 4.3(a-c) illustrate the simulation settings for the three metallic layers, where a periodic and infinite array is assumed via master-slave boundary conditions to bound the transverse planes of a unit cell. An excitation is provided by Floquet ports, where port

Table 4.1. Calculated optimal circuit parameters provided by the broadband semi-analytical approach for the antireflection transmitarray. Distinctive equivalent series LC circuits are employed for the three metallic layers, while the circuit models of each metallic layer along the x- and y-polarisations are identical. The units for inductances and capacitances are pH and fF, respectively.

Top layer		Middle layer		Bottom layer	
L_1	C_1	L_2	C_2	L_3	C_3
5.5	0.5	33.4	2.0	84.5	0.7

de-embedding to the pattern surfaces are applied to extract the intrinsic responses of the patterns without propagation effects in the media. In order to minimise the metal loss, gold is utilised for metallic layers, while its surface impedance at terahertz frequencies is detailed by a Drude model (Lucyszyn, 2007).

A physical realisation of each metallic layer is carried out by developing patterns of four-fold symmetry. To avoid diffraction and to obtain a relatively strong robustness to obliquely incident waves, a subwavelength unit cell size of $a = 120$ µm is chosen, which corresponds to $0.13\lambda_0$ or $0.45\lambda_{si}$ at 330 GHz, where λ_0 and λ_{si} denote the wavelengths in free-space and silicon, respectively. The admittance tensor of each metallic layer can

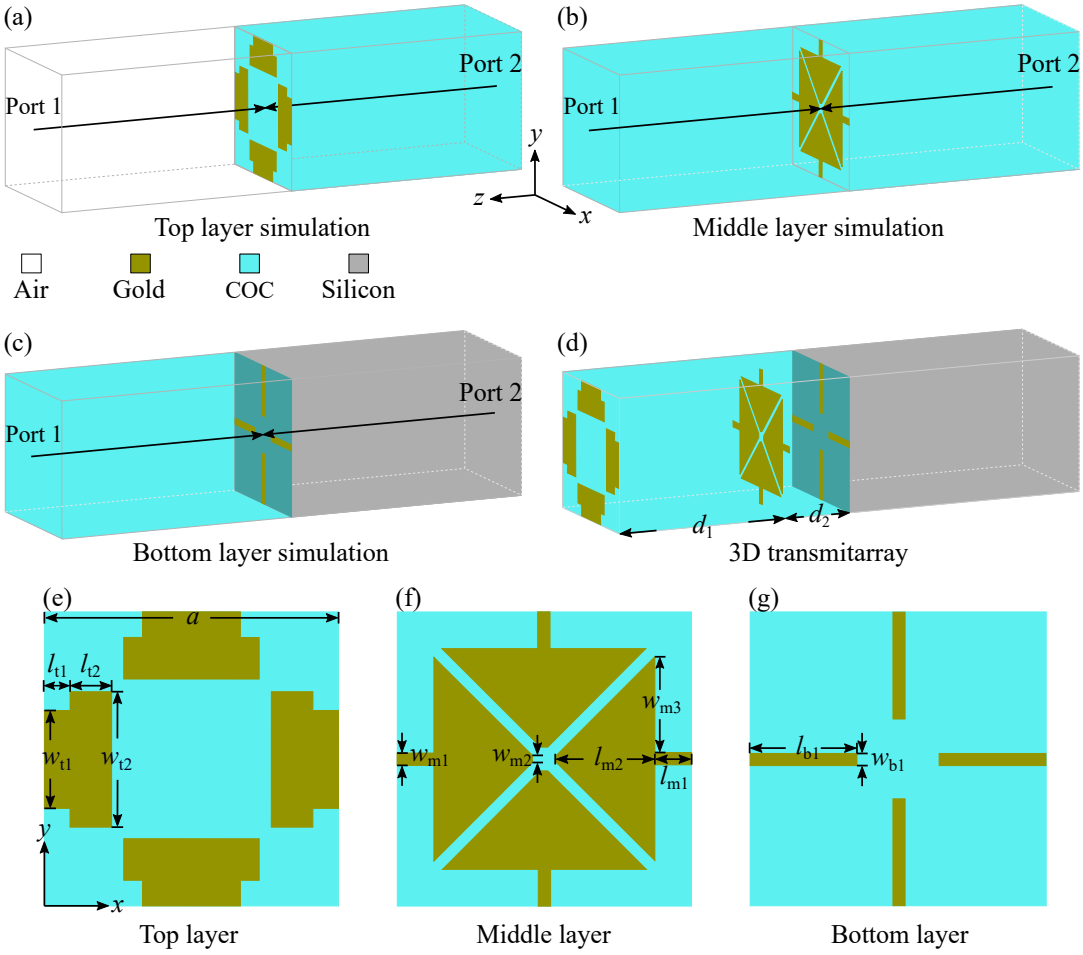

Figure 4.3. Full-wave simulation settings and unit cell geometry of the proposed antireflection transmitarray. (a) Top layer, (b) middle layer, and (c) bottom layer simulation settings. Master-slave boundary conditions are employed in the unit cell transverse planes to mimic a periodic and infinite array. Floquet ports are implemented as an excitation, while the arrows in (a-c) depict port phase de-embedding to acquire the intrinsic responses from the patterns. (d) 3D view of a complete transmitarray unit cell, (e) top, (f) middle, and (g) bottom metallic layers.

be extracted based on the simulated reflection coefficients by using Equation (4.4). Thereafter, the equivalent inductance and capacitance of each layer derived based on the simulated admittance tensor are then compared to the optimal circuit parameters as presented in Table 4.1, and the metallic pattern is adjusted accordingly to match the optimal values.

Figures 4.3(d-g) show the physically realised unit cell geometry of the antireflection transmitarray, and its detailed structural parameters are presented in Table 4.2. Typically, a wide metallic strip provides a relatively low equivalent inductance, hence a strip width of $w_{t1} = 40$ μm is employed for the top metallic layer to meet the required inductance of $L_1 = 5.5$ pH. On the other hand, thin metallic strips of $w_{b1} = 5$ μm are implemented for the bottom metallic layer to obtain the desired relatively high inductance of $L_3 = 84.5$ pH. For the middle metallic layer, a high equivalent capacitance of $C_2 = 2.0$ fF is demanded, and thus isosceles-trapezoid metallic patches are closely arranged.

Table 4.2. Physical dimensions of the transmitarray unit cell. The units are in μm.

Parameter	Value	Parameter	Value
a	120	l_{m1}	15
d_1	162	l_{m2}	40
d_2	57	w_{m1}	5
l_{t1}	10	w_{m2}	3
l_{t2}	17	w_{m3}	39
w_{t1}	40	l_{b1}	43
w_{t2}	55	w_{b1}	5

4.3.2 Simulation results

The calculated and simulated results of the proposed transmitarray, conventional antireflection coating, and bare silicon are given in Figure 4.4. The simulated results of the proposed transmitarray show an excellent agreement with the calculated ones provided by the optimal circuit model, thus suggesting negligible near-field couplings between metallic layers. Further simulations reveal that the slight deviation between them is mainly contributed from metal loss, which has been accounted for in the 3D full-wave simulation but assumed to be negligible in the circuit model. Simulation results reveal

that the proposed structure maintains a reflection magnitude below −20 dB and a transmission magnitude above −0.17 dB from 203 GHz to 357 GHz, corresponding to a relative bandwidth of 55.0% and a minimum efficiency of 96.1%. COC has a refractive index of $n_{coc} = 1.53$ that approximates an optimal refractive index value of $\sqrt{n_{air} n_{si}} = 1.85$ for constructing an antireflection coating at the air-silicon interface. Hence, a conventional antireflection coating made of COC with a quarter-wavelength thickness of 179 μm is considered as a comparison. Simulation results indicate that the COC-based antireflection coating enables a minimum reflection magnitude of −14.46 dB at the design centre frequency of 275 GHz. It can be inferred from Figure 4.4 that the proposed antireflection transmitarray shows a remarkable reflection suppression and significant transmission enhancement compared to the COC-based antireflection coating.

Figure 4.5 depicts the simulated performance of the transmitarray and conventional COC-based antireflection coating in response to obliquely incident waves. For the antireflection transmitarray, a −20-dB reflection magnitude can be sustained in a limited range up to an incidence angle of 30° for the TE-polarisation and an angle of 45° for the TM-polarisation. Further, in order to maintain a reflection magnitude below −20 dB

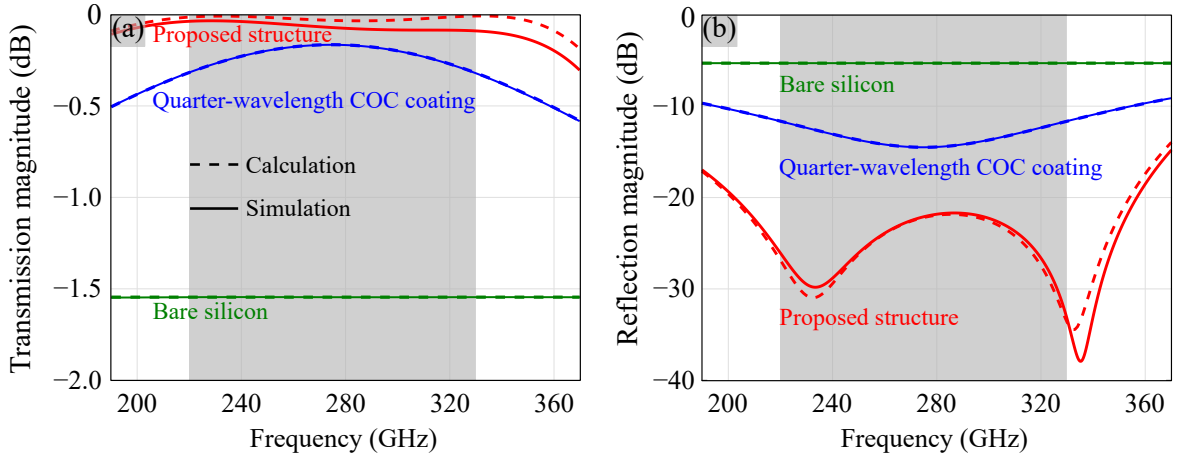

Figure 4.4. Calculation and simulation results of the proposed structure, quarter-wavelength COC coating, and bare silicon. (a) Transmission magnitude and (b) reflection magnitude. The calculated results of the proposed structure and quarter-wavelength COC coating are provided by the corresponding circuit models, while the calculated performance of the bare silicon are obtained by using Fresnel equations. The simulated results of the three structures are presented by 3D full-wave simulations. The COC-based antireflection coating is designed at 275 GHz, and it has a thickness of 179 μm. It is found that 30% of the incident power is reflected at the air-silicon interface for a bare silicon slab. The shaded area marks the frequency range of interest from 220 GHz to 330 GHz, defined for the WR-3.4 waveguide band.

from 220 GHz to 330 GHz for the transmitarray, additional simulations reveal that the incidence angle should be confined to 25° for the TE-polarisation and 30° for the TM-polarisation. The transmission magnitude is less affected by the incidence angle for both TE- and TM-polarisations. The relatively strong robustness of the transmitarray at oblique incidence can be explained in terms of the implemented subwavelength unit cell size ($a = 0.13\lambda_0$ at 330 GHz). A small unit cell is beneficial to achieving a limited phase difference between unit cell edges under oblique incidence. Further, reducing the total dielectric spacer thickness from the employed $d_1 + d_2 = 219$ µm ($0.24\lambda_0$ at 330 GHz) to a smaller value is expected to obtain an increased robustness to obliquely incident waves. Importantly, Figure 4.5 further demonstrates the significant antireflection performance improvement of the transmitarray compared to the conventional antireflection coating made of COC.

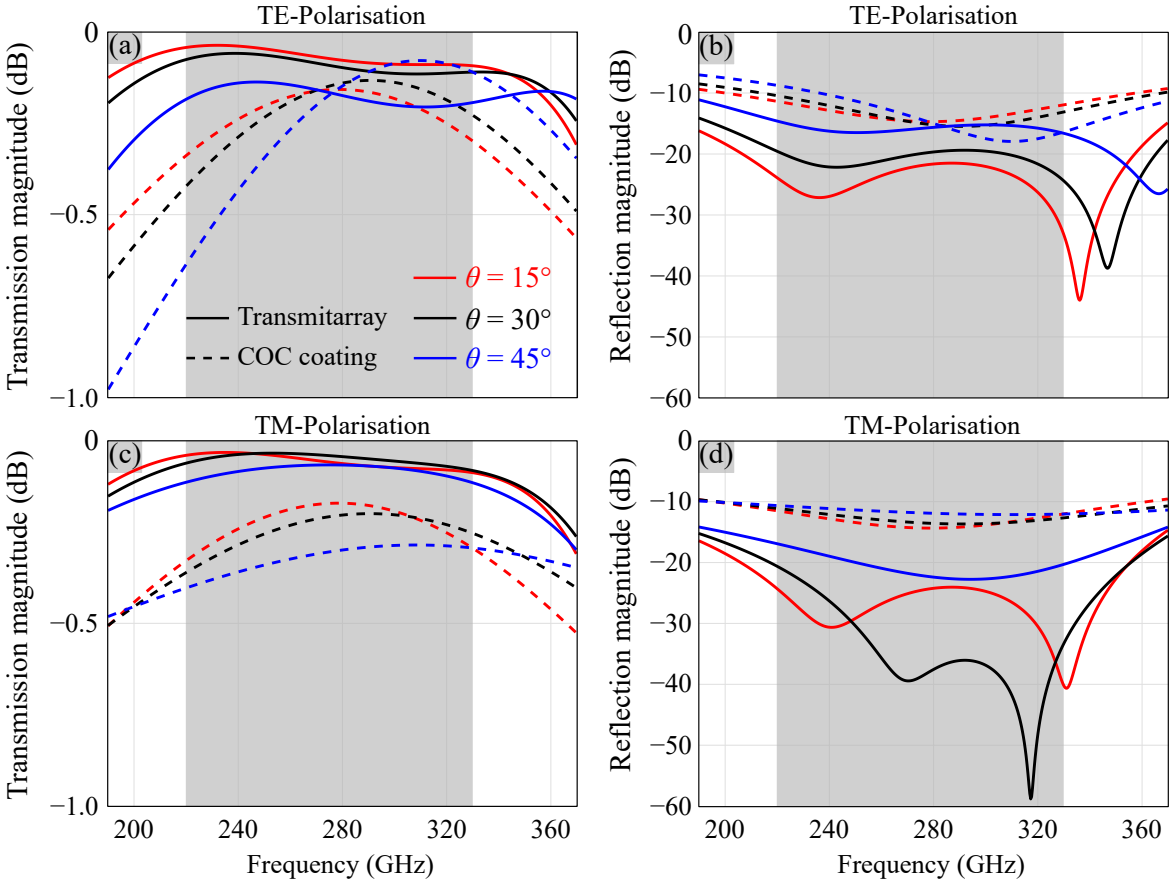

Figure 4.5. Simulation results of the antireflection transmitarray and quarter-wavelength COC coating under oblique incidence. (a) Transmission magnitude and (b) reflection magnitude for the TE-polarisation. (c) Transmission magnitude and (d) reflection magnitude for the TM-polarisation. The shaded area marks the frequency range of interest from 220 GHz to 330 GHz, defined for the WR-3.4 waveguide band.

Table 4.3. Performance comparison between the proposed antireflection transmitarray and representative existing designs. Simulation and measurement bandwidths are defined based on reflection magnitude below −20 dB. GaAs indicates gallium arsenide, and it has a refractive index of 3.56.

Structure	Centre frequency (GHz)	Dielectric interface	Metallic layers	Simulation bandwidth (%)	Measurement bandwidth (%)	Reference
Cross-resonators	880	Silicon	2	4.6	21.9	Huang *et al.* (2017)
Circular cylinders	910	Silicon	2	4.4	4.1	Chang *et al.* (2018)
Split-ring resonators	1545	GaAs	2	5.8	5.2	Chen *et al.* (2010)
Square holes	5040	Silicon	Tri-layer all-dielectric	8.3	13.7	Chen and Zhang (2014)
This work	280	Silicon	3	55.0	–	

The performance of the proposed antireflection transmitarray is compared to notable designs from the literature as shown in Table 4.3. Simulation results suggest that the proposed structure exhibits an advantageous performance over the existing designs in terms of the relative bandwidth defined by $R < -20$ dB. Bi-layer antireflection structures employing cross-resonators (Huang *et al.*, 2017) and circular cylinders (Chang *et al.*, 2018) were developed based on etched silicon. Despite of their advantages of reduced structure complexity, both designs exhibited a limited fractional bandwidth. An array of split-ring resonators and metal meshes were implemented to construct an antireflection transmitarray, and it showed an excellent robustness to obliquely incident waves (Chen *et al.*, 2010). However, due to the absence of a magnetic response, this transmitarray maintained a near-zero reflection in a narrow bandwidth. Besides, an all-dielectric structure relying on gradient index theory was presented to suppress reflection at the air-silicon interface, but the obtained −20-dB simulation reflection relative bandwidth was confined to 8.3%, and fabrication challenges arose resulting from the employment of tri-layer square holes. The enhanced bandwidth of the proposed transmitarray can be attributed to the involved systematic procedure for performance optimisation.

4.4 Conclusion

This Chapter has introduced a broadband semi-analytical approach incorporating network analysis and genetic algorithm for transmitarray designs. In this approach, the network analysis aids rapid calculation of the scattering characteristics of the anisotropic transmitarray, while the genetic algorithm as an optimisation algorithm is employed to

determine the optimal frequency-independent circuit parameters to achieve a desired performance. As a proof-of-concept, a wideband and highly efficient antireflection transmitarray is rigorously designed with the aid from the broadband approach. Simulation results suggest that the proposed transmitarray is able to suppress reflection at the air-silicon interface to a level below -20 dB from 203 GHz to 357 GHz, while a transmission magnitude above -0.17 dB can be maintained. To achieve a wider bandwidth, the broadband approach can readily account for more metallic layers at a minimum computational cost. Importantly, this proposed approach is capable of configuring transmitarrays with enhanced bandwidth and efficiency for various functionalities.

Chapter 5

Broadband terahertz quarter-wave transmitarray

POLARISATION conversion devices are key components in spectroscopy and wireless communications systems. Conventional terahertz waveplates made of natural birefringent materials typically suffer from low efficiency, narrow bandwidth, and substantial thickness. To overcome the limitations associated with conventional waveplates, a terahertz quarter-wave transmitarray with enhanced efficiency and wide bandwidth is proposed. The quarter-wave transmitarray is rigorously designed based on a broadband semi-analytical approach employing network analysis and genetic algorithm. Simulation results suggest that the design can achieve linear-to-circular polarisation conversion with a 3-dB axial ratio relative bandwidth of 53.3%, spanning 205 GHz to 354 GHz. The measurement results confirm that the proposed design enables a 3-dB axial ratio from 205 GHz to at least 340 GHz with a total efficiency higher than 70.2%, where the upper frequency bound is limited by the available experimental facility. This quarter-wave transmitarray can cover an entire terahertz electronics band, and can be scaled to cover other nearby bands, which are technologically significant for future portable systems.

5.1 Introduction

Birefringent materials such as crystalline dielectrics (Grischkowsky *et al.*, 1990; Chen *et al.*, 2013b) and wood (Reid and Fedosejevs, 2006) provide distinct refractive indices to electric field components along two orthogonal directions, thus lead to different phase accumulations. By carefully controlling the thickness of a birefringent material, a prescribed phase difference between the two electric field components can be achieved at a given frequency. However, waveplates made of quartz using one single-layer typically feature narrow bandwidth of $\sim$14.4% and significant reflection and absorption losses. A multi-layer quartz-based waveplate was presented to improve the relative bandwidth to 32%, but exhibited a bulky configuration for an efficiency of 50% (Chen *et al.*, 2013b). Alternative wave-plate construction methods involving the effective medium theory (Levy and Fainman, 2004; Nagai *et al.*, 2014) or the form-birefringence methodology (Hu *et al.*, 2018; Shi and Hao, 2018) demand further efficiency and bandwidth enhancement. As a substitute, polarisation conversions can be implemented by employing transmitarrays.

Transmitarrays formed by periodically arranged subwavelength resonators can be exploited to locally manipulate the amplitude, phase, and polarisation state of transmitted waves. Transmitarrays have demonstrated their extraordinary electromagnetic properties in wavefront shaping (Pfeiffer *et al.*, 2014; Chang *et al.*, 2017) and polarisation control (Pfeiffer and Grbic, 2013a; Fan *et al.*, 2015). More specifically relevant to this Chapter, transmitarrays are also capable of providing designable birefringence to realise quarter-wave plates for conversion between linear and circular polarisations. In the microwave engineering community, strip gratings were employed in a quarter-wave plate design (Blanco and Sauleau, 2018), with a limited 3-dB axial ratio relative bandwidth of 20%. A quarter-wave plate based on reactive impedance surfaces exhibited a relative bandwidth of 40%, but the six layers of metal would be prohibitively difficult to fabricate at terahertz frequencies (Momeni Hasan Abadi and Behdad, 2016b). In the millimetre-wave region, a tri-layer quarter-wave plate exhibited a simulated 3-dB axial ratio fractional bandwidth of 40% and an efficiency above 59.2% (Pfeiffer and Grbic, 2013c). However, the quarter-wave plate design did not involve optimisation algorithms, which leaves room for performance improvement. In the terahertz domain, split ring resonators (Han *et al.*, 2018) and metal slots (Wang *et al.*, 2015a) have been reported to realise linear-to-circular polarisation conversion with an efficiency of 62% and 30%, respectively, requiring further efficiency improvement. In the optics region,

waveplates typically show low transmittance, resulting from the relatively high metal losses at optical frequencies (Yu *et al.*, 2012; Yang *et al.*, 2013).

In this Chapter, we propose a broadband quarter-wave transmitarray with enhanced efficiency. The proposed design targets coverage of the WR-3.4 waveguide frequency range from 220 GHz to 330 GHz, which is foreseen for point-to-point terahertz communications (IEEE 802 LAN/MAN Standards Committee, 2017). The quarter-wave transmitarray consists of three metallic layers separated by two dielectric spacers. Each metallic layer can be modeled as a parallel *LC* circuit along the *x*- or *y*-polarisation, while the dielectric spacers are represented by transmission lines in the *z*-direction. Thus, the broadband semi-analytical approach presented in Chapter 4 is implemented to optimise the quarter-wave transmitarray via an equivalent circuit model, so that a low axial ratio and high transmission can be maintained over a wide bandwidth. The transmitarray is then physically realised by designing a particular pattern for each metallic layer, which reproduces the calculated optimal circuit parameters.

5.2 Design

Here, we design a quarter-wave transmitarray that comprises three metallic layers separated by two dielectric spacers. Figure 5.1(a) illustrates a transmitarray structure with identical top and bottom layers, and the two dielectric spacers having the same thickness. The induced currents on the middle layer generated by the –*x*-directed quasi-static magnetic field are cancelled out due to the symmetric nature of the structure

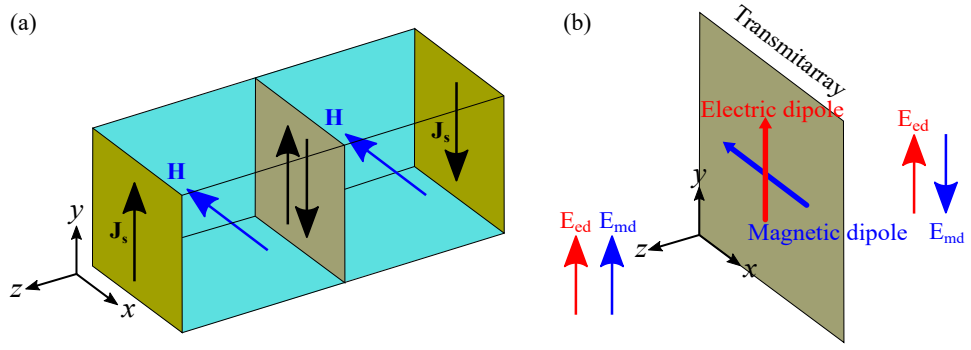

Figure 5.1. Induced currents and electric field distributions of the transmitarray. (a) Schematic diagram of the induced currents on the transmitarray generated by a quasi-static magnetic field along the –*x*-axis. The top and bottom layers are identical, and the dielectric spacers share the same thickness. (b) Sketch of the electric field distributions contributed from the electric and magnetic dipoles of equal strength.

(Pfeiffer and Grbic, 2013c). As a result, the three metallic layers collectively interact with the electric field, while the magnetic response is shaped only by the top and bottom layers. Therefore, design priority is given to the top and bottom layers to manipulate the magnetic response firstly, while the middle layer is subsequently tailored for the electric response without affecting the magnetic field. Consequently, the electric and magnetic responses are controlled separately, and thus each unit cell acts as a Huygens' source that consists of crossed electric and magnetic dipoles of equal strength. Figure 5.1(b) depicts the electric fields generated by the electric and magnetic dipoles, where electric fields present equal strength and opposite signs in the $z < 0$ space but the same sign in the $z > 0$ space. As a result, a destructive interference occurs in the $z < 0$ space that leads to a reduced reflection from the transmitarray, while a constructive interference happens in the $z > 0$ space that results in an improved transmission (Decker *et al.*, 2015). Therefore, a large transmission phase tuning range can be accomplished simultaneously with a high transmittance by properly controlling electric and magnetic dipole responances, leading to an efficiency-enhanced transmitarray (Pfeiffer and Grbic, 2013c; Jia *et al.*, 2015; Shalaev *et al.*, 2005).

In order to facilitate the design process and optimise the device performance, the quarter-wave transmitarray is designed with an aid from the broadband semi-analytical approach. When the quarter-wave transmitarray is illuminated by an incident wave that is linearly polarised at 45° with respect to the major principal axis, the x- and y-polarisations are equally excited. Hence, we can choose a pattern for each metallic layer that exhibits distinctive equivalent parallel LC circuit behaviors along the x- and y-axes. It should be noted that here the equivalent parallel LC circuit is chosen as an illustrative example, and the metallic pattern could also be in other forms including equivalent series LC circuit, or purely inductive or capacitive circuits. For simplicity, it is assumed that all materials employed are lossless at this stage. Based on the assumptions above, the admittance tensor of an i^{th} metallic layer can be written as Equation 4.1. In order to reduce the material loss, ultra-low loss cyclic olefin copolymer (COC) is applied for the dielectric spacers. COC shows a relative permittivity of $\epsilon_{\text{r}} = 2.33$ and loss tangent of $\tan\delta = 0.0005$ from 220 GHz to 330 GHz (Nielsen *et al.*, 2009). The dielectric spacers can be modeled as transmisson lines along the z-axis. Hence, the total 4×4 **ABCD** transfer matrix of the transmitarray that comprises three metallic layers separated by two subwavelength dielectric spacers can be expressed as Equation 4.2. Once the **ABCD** matrix is established, the S-parameters of the anisotropic transmitarray under linearly polarised incident waves at normal incidence can be obtained by using Equation 4.3.

To achieve circular polarisation with high efficiency and high purity, the quarter-wave transmitarray requires near-unity transmittances for the two orthogonal electric field components, and a constant quadrature phase difference between them. Therefore, the design objectives can be expressed as

$$|S_{21}^{xx}|^2 = |S_{21}^{yy}|^2 = 1, \tag{5.1a}$$

$$\angle S_{21}^{xx} - \angle S_{21}^{yy} = 90^\circ. \tag{5.1b}$$

Possible range for the inductance and capacitance within a certain unit cell size are estimated based on the simulations of metallic patterns with equivalent parallel LC circuits along the x- and y-polarisations. Considering the feasibility for fabrication of a dielectric spacer and the assumption of negligible evanescent modes, a spacer thickness range from 100 to 200 μm is specified for the targeted frequency range between 220 GHz and 330 GHz. With the constraints identified, a cost function is assigned in the genetic algorithm to find the optimal (L_{xi}, C_{xi}, L_{yi}, C_{yi}) for the i^{th} metallic layer and the desired thickness d for the dielectric spacers, with the aim of satisfying the objectives over a wide bandwidth. Table 5.1 shows the calculated optimal inductances and capacitances for the quarter-wave transmitarray provided by the outlined broadband semi-analytical approach, while the thickness of each dielectric spacer is found to be d = 195 μm.

Once the optimal set of (L_{xi}, C_{xi}, L_{yi}, C_{yi}) is determined for the i^{th} metallic layer, a search for the corresponding physical structure is conducted by following the procedure presented in Chapter 4. Electromagnetic simulations are performed with the commercial software ANSYS HFSS. To minimise the metal loss, gold is utilised for the metallic layers, and its surface impedance at terahertz frequencies is described by a Drude model (Lucyszyn, 2007). In order to avoid diffraction, a lattice constant of 540 μm is chosen,

Table 5.1. Calculated optimal frequency-independent circuit parameters for the quarter-wave transmitarray, provided by the broadband semi-analytical approach. The equivalent inductance and capacitance of the i^{th} metallic layer along the x- and y-axes are denoted as (L_{xi}, C_{xi}) and (L_{yi}, C_{yi}), respectively. The units for inductances and capacitances are pH and fF, respectively.

Top/bottom layer				Middle layer			
x-axis		y-axis		x-axis		y-axis	
L_{x1}	C_{x1}	L_{y1}	C_{y1}	L_{x2}	C_{x2}	L_{y2}	C_{y2}
170.5	0.9	265.6	1.9	123.1	0.7	212.6	2.7

which corresponds to $0.5\lambda_0$ at the design centre frequency of 275 GHz. Figure 5.2 shows the physically realised structure of a quarter-wave transmitarray unit cell. As mentioned, the top and bottom metallic layers are identical to enhance the efficiency, while the equivalent circuit of each metallic layer under the x- or y-polarisation is basically a parallel LC circuit as implemented in the broadband semi-analytical approach. Detailed dimensions of the structure are illustrated in Table 5.2. Notably, a strip width of 4 μm ($w_{t1} = w_{m1} = 2$ μm) is desired at the unit cell borders to provide the optimal equivalent inductance under the y-polarisation. Simulations suggest that the transmitarray exhibits a large tolerance to the strip width variation up to $w_{t1} = w_{m1} = 10$ μm.

Figures 5.3(a) and 5.3(b) show the transmission coefficients of the quarter-wave transmitarray as calculated using the broadband semi-analytical approach and the 3D full-wave simulation. Since the calculation does not account for near-field coupling, the close agreement between the simulation and calculation results implies negligible coupling effects. Within the frequency range of interest from 220 GHz to 330 GHz, the maximum simulated insertion losses for the x- and y-polarisations are 1.45 dB and 1.04 dB,

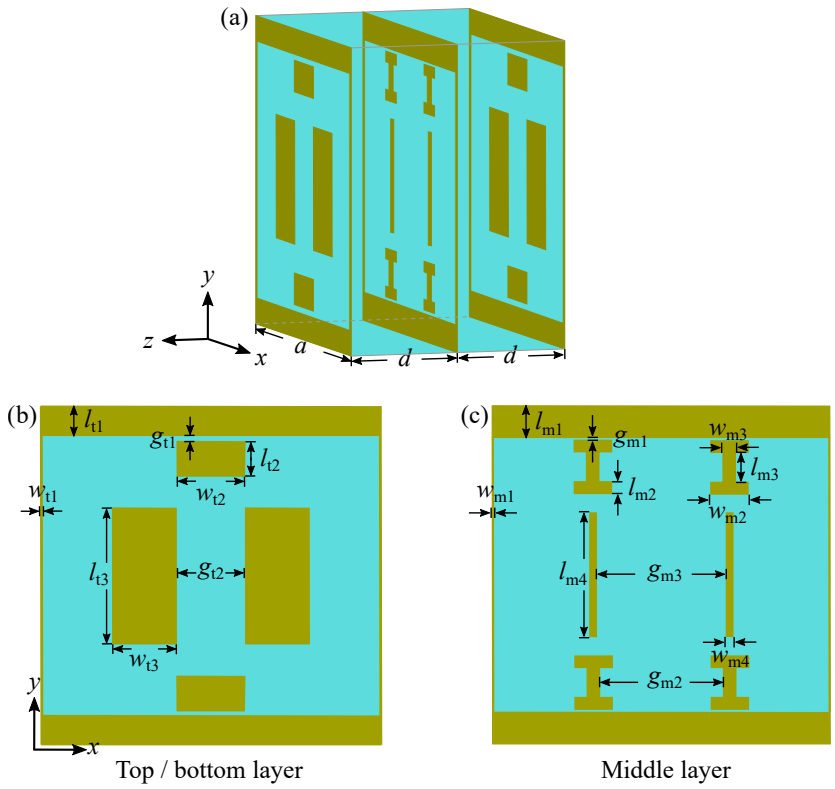

Figure 5.2. Unit cell geometry of a complete quarter-wave transmitarray. (a) 3D view, (b) top and bottom layers, and (c) middle layer. The top and bottom layers are identical to enhance the transmitarray efficiency.

Table 5.2. Detailed dimensions of the quarter-wave transmitarray unit cell. The units are in µm.

Parameter	Value	Parameter	Value	Parameter	Value
a	540	w_{t3}	101	l_{m3}	49
d	195	g_{t1}	10	w_{m3}	20
l_{t1}	47	g_{t2}	111	l_{m4}	198
w_{t1}	2	l_{m1}	50	w_{m4}	10
l_{t2}	54	w_{m1}	2	g_{m1}	5
w_{t2}	108	l_{m2}	18	g_{m2}	199
l_{t3}	216	w_{m2}	60	g_{m3}	209

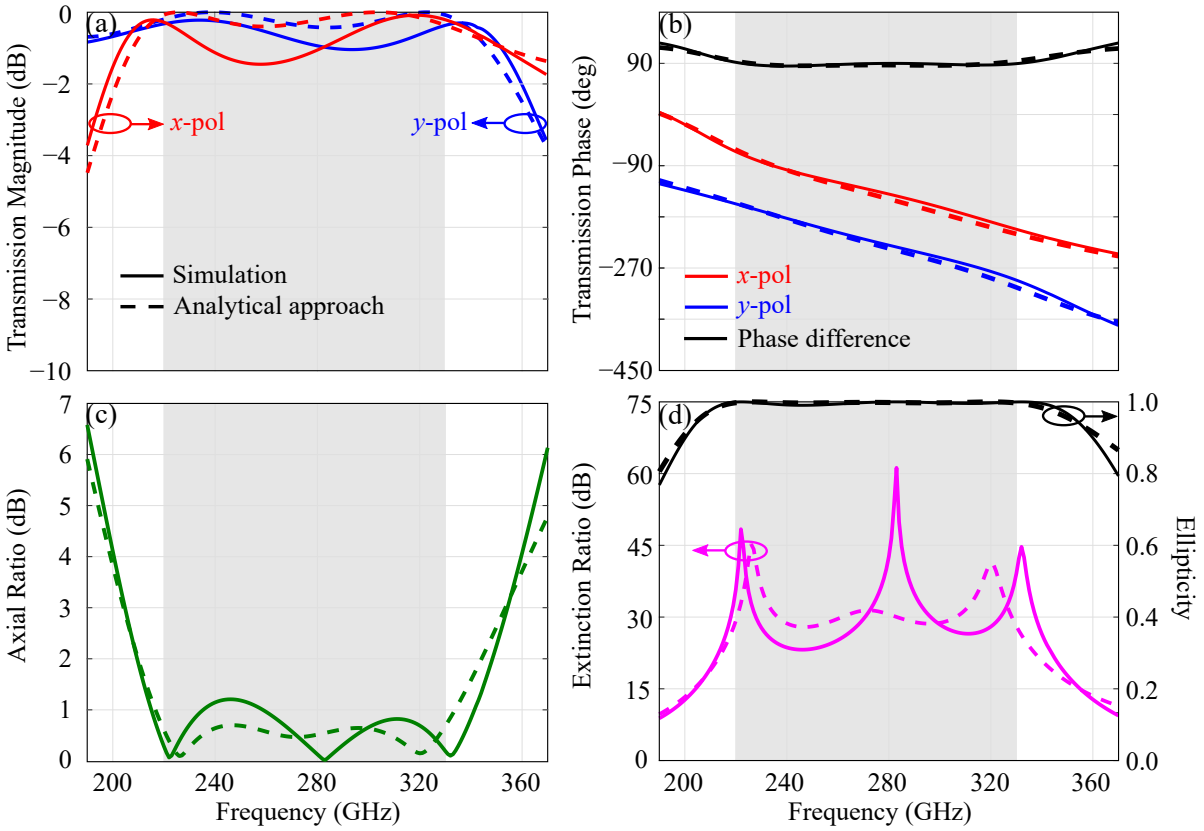

Figure 5.3. Transmission coefficients and transmitted wave circular polarisation purity of the quarter-wave transmitarray. (a) Transmission magnitude, (b) transmission phase, (c) axial ratio, and (d) extinction ratio and ellipticity. The calculated results are provided by the semi-analytical approach, while the simulated results are obtained from 3D full-wave simulation. The shaded area marks the frequency range of interest from 220 GHz to 330 GHz.

respectively, while the phase difference between the two components remains close to 90°. Moreover, simulations reveal that the reflection magnitudes for the x- and

y-polarisations from 220 GHz to 330 GHz are less than -5.75 dB and -7.41 dB, respectively. Thus, the transmitarray power loss is mainly from reflections instead of material losses. However, the material losses considered in the simulation, together with the deviation between the optimal and obtained equivalent inductances and capacitances collectively contribute to the discrepancy between the calculated and simulated results.

The complex transmission coefficients presented by the semi-analytical approach and the 3D full-wave simulation suggest that the quarter-wave transmitarray realises linear-to-circular polarisation conversion upon transmission. In order to rigorously quantify the performance of the quarter-wave transmitarray, the axial ratio of the transmitted wave is evaluated. The axial ratio refers to the ratio of the major axis to the minor axis of the transmitted wave polarisation ellipse, which can be written as (Balanis, 2016)

$$\mathrm{AR} = \sqrt{\frac{E_{xo}^2 + E_{yo}^2 + \left[E_{xo}^4 + E_{yo}^4 + 2E_{xo}^2 E_{yo}^2 \cos(2\Delta\phi)\right]^{1/2}}{E_{xo}^2 + E_{yo}^2 - \left[E_{xo}^4 + E_{yo}^4 + 2E_{xo}^2 E_{yo}^2 \cos(2\Delta\phi)\right]^{1/2}}}, \tag{5.2}$$

where $E_{xo} = |S_{21}^{xx}|$ and $E_{yo} = |S_{21}^{yy}|$ are the transmission amplitudes of the x- and y-polarisations, respectively, and $\Delta\phi = \angle S_{21}^{xx} - \angle S_{21}^{yy}$ is the phase difference between them. It is possible to relate the axial ratio to the extinction ratio and the detailed derivation is shown in Appendix A. It is noted that the commonly used 3-dB axial ratio criterion corresponds to an extinction ratio of $\sim$15 dB. To further evaluate the transmitarray polarisation conversion performance, the Stokes parameters of the transmitted wave is calculated using (McMaster, 1954)

$$\begin{aligned} S_0 &= |E_{xo}|^2 + |E_{yo}|^2 \\ S_1 &= |E_{xo}|^2 - |E_{yo}|^2 \\ S_2 &= 2|E_{xo}||E_{yo}|\cos(\Delta\phi) \\ S_3 &= 2|E_{xo}||E_{yo}|\sin(\Delta\phi). \end{aligned} \tag{5.3}$$

The output wave ellipticity is defined as $\chi = S_3/S_0$, where $\chi = 1$ indicates an ideal left-handed circularly polarised (LHCP) output wave, while $\chi = -1$ denotes a perfect right-handed circularly polarised (RHCP) output wave. Figures 5.3(c) and 5.3(d) depict the axial ratio, extinction ratio, and ellipticity of the transmitted wave obtained from the semi-analytical approach and simulation, revealing that a simulated 3-dB axial ratio fractional bandwidth of 53.3% can be sustained over a frequency range extending from 205 GHz to 354 GHz. Additionally, the simulated ellipticity from 220 GHz to 330 GHz is above 0.99, while the axial ratio remains lower than 1.21 dB that corresponds to an extinction ratio above 23.16 dB.

5.3 Fabrication

A sample manufacture was undertaken by the Functional Materials and Microsystems Research Group and the Micro Nano Research Facility at RMIT University. The three-layer quarter-wave transmitarray is fabricated using a micro fabrication approach that involves multiple steps of photolithography and polymer bonding. This process is applied due to the limitations associated with the COC processing (Ako *et al.*, 2020b,a). Figure 5.4 shows the simplified illustration of the fabrication process. The bottom metallic layer of Au resonators are printed onto a 5 μm-thick COC (mr-I T85-20.0) supporting layer using standard photolithography (MLA150 Maskless Aligner, Heidelberg Instruments) and metal evaporation (Kurt J. Lester E-beam Evaporator Deposition PVD75, at 0.5 A/s) techniques. Poly (methyl methacrylate) (PMMA) is employed as a sacrificial layer to ease the release of COC from the supporting Si wafer. To realise the first spacer, a free-standing COC film is prepared separately by spin-coating COC (mr-I T85-20.0) on a separate wafer with PMMA sacrificial layer. Herein, a COC film thickness of 190 ± 10 μm is obtained by spin-coating COC (mr-I T85-20.0) 6 times at 3000 rpm. The COC is properly dehydrated after every spin. The released COC film is then bonded to the bottom metallic layer using a wafer bonder (Hot Embosser/Bonder/Thermal NIL EVG) at 100 °C and 600 N. The middle metallic layer is then printed onto the bonded spacer. The second spacer is also prepared in a similar way as the first spacer, and bonded to the middle metallic layer using the same bonding conditions. This is followed by the printing of the top metallic layer onto the second spacer. The metallic pattern alignment is conducted with the aid of cross alignment markers on each layer. Images of the fabricated free-standing prototype are given in Figure 5.5.

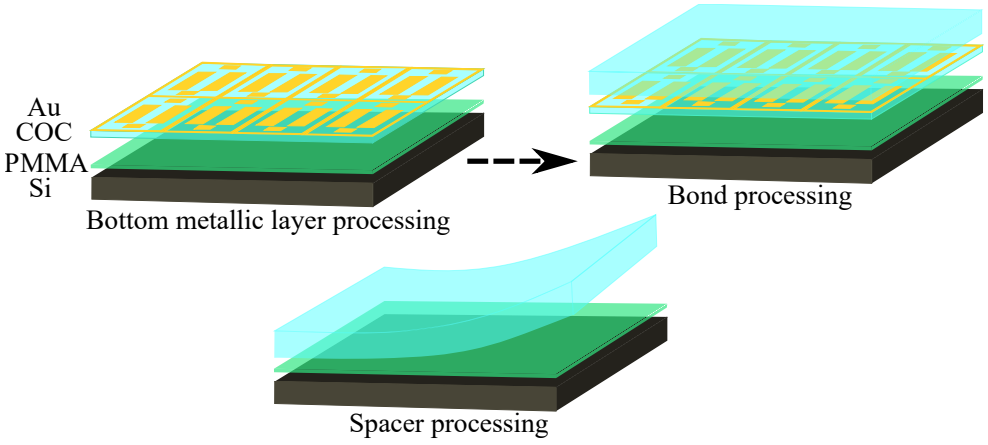

Figure 5.4. Fabrication process. The three-layer quarter-wave transmitarray employs two subwavelength COC spacers.

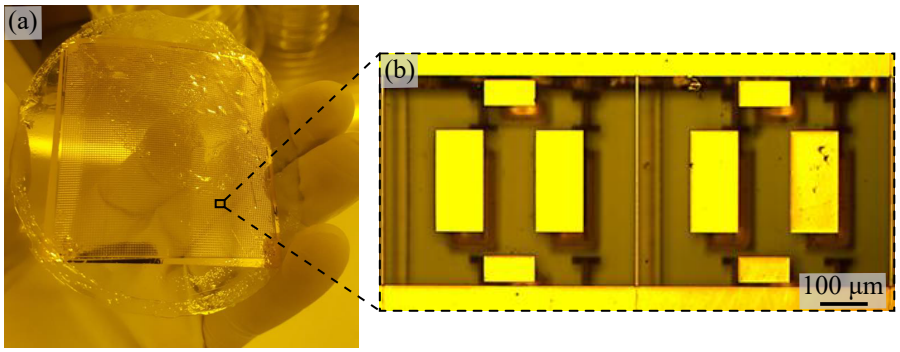

Figure 5.5. Fabricated quarter-wave transmitarray prototype. (a) Photograph of the fabricated sample, and (b) magnified view containing two unit cells. The wrinkle part shown in (a) contains air bubbles introduced during the fabrication. The top layer is shifted -24 μm (4% of the unit cell size) along the x-axis and 48 μm along the y-axis relative to the middle and bottom layers.

5.4 Measurement

To validate its performance, the manufactured quarter-wave transmitarray is characterised using a Keysight Precision Network Analyzer (PNA) together with VDI WR-3.4 Extension Modules. We configure the extension modules so that they operate from 205 GHz to 340 GHz, which is beyond their typical frequency coverage of 220 GHz to 330 GHz (Hesler *et al.*, 2007). As illustrated in Figure 5.6(a), a vertically polarised incident wave is collimated by Lens 1 and then focused onto the sample after propagating through Lens 2. Lens 3 collimates the transmitted wave, while Lens 4 focuses the collimated wave onto the receiver. As a result, the fabricated sample with a size of 50 mm$\times$50 mm is illuminated by the incident beam with a focal spot of $\sim$1 mm in diameter. In addition, the Rayleigh range of the incident beam equals 0.72 mm at the design centre frequency of 275 GHz, and the three metallic layers are therefore included inside of the Rayleigh range of the focused beam. Thus, a normally incident plane wave illumination is assumed over the entire measurement frequency range. The employed WR-3.4 metallic waveguides have a length of 25.4 mm, and in this waveguide, the cross-polarised wave manifested as the TE_{01} mode is below its cutoff frequency. As a consequence, no polarisers are required to screen the cross-polarisation component that experiences an attenuation of 31 dB/mm at 300 GHz in this waveguide. The transmission coefficients of the quarter-wave transmitarray under the x- and y-polarisations are measured separately by rotating the sample. As a reference, a measurement is taken without the presence of sample.

5.5 Results

Figures 5.6(b) and 5.6(c) depict the simulated and measured transmission coefficients of the quarter-wave transmitarray, where a good agreement is confirmed. The measured

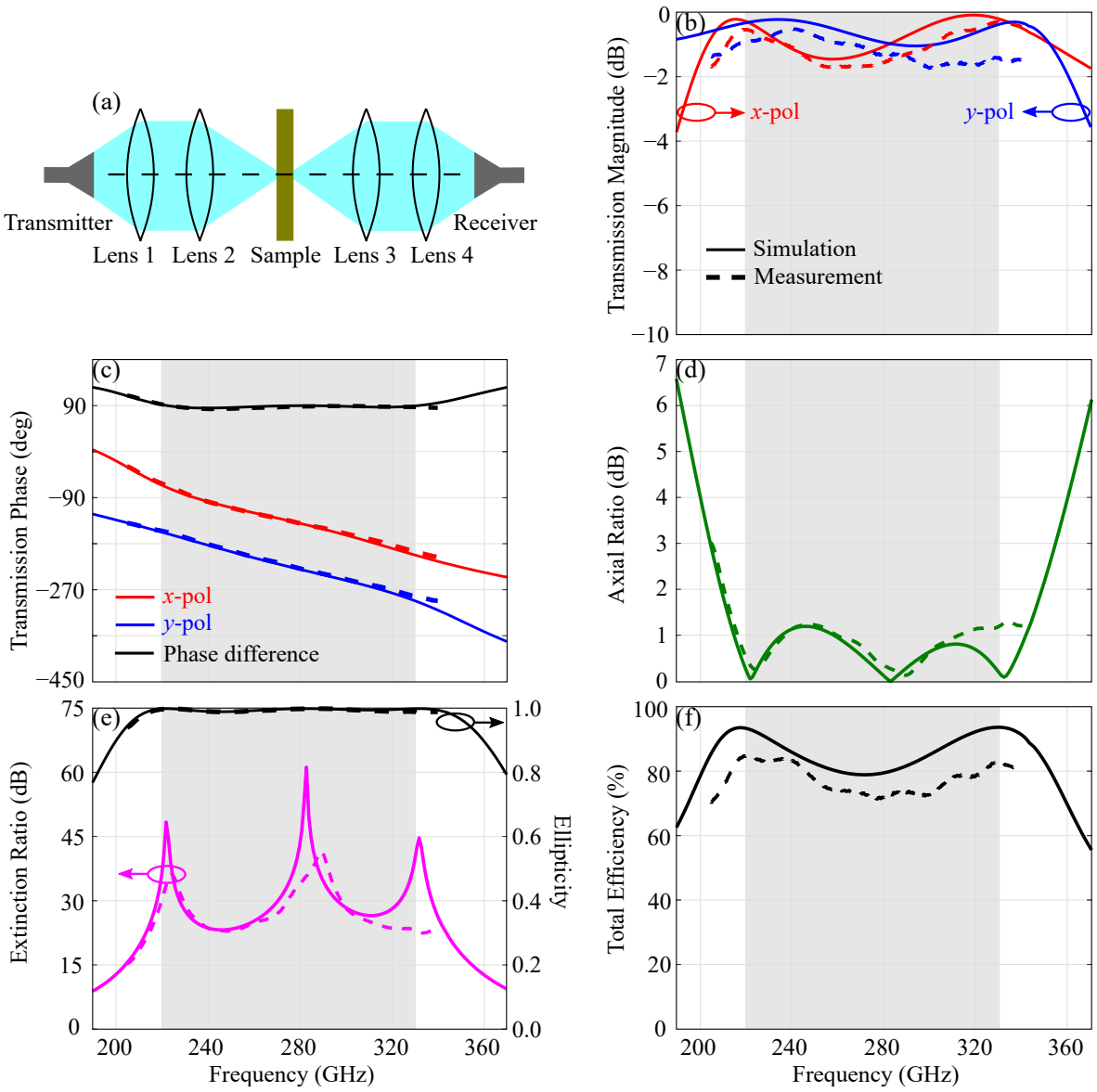

Figure 5.6. Experimental setup and comparison between the simulated and measured results. (a) Schematic of the experimental setup using Keysight PNA and VDI WR-3.4 Extension Modules. Four lenses are used for collimating and focusing the beam. The measurement frequency band ranges from 205 GHz to 340 GHz. (b) Transmission magnitude, (c) transmission phase, (d) axial ratio, (e) extinction ratio and ellipticity, and (f) total efficiency. All transmission measurements are normalised against the reference measurement taken without the sample. The measured phase profiles for the x- and y-polarisations are offset by a constant value to coincide with simulations. The shaded area marks the frequency range of interest from 220 GHz to 330 GHz.

results reveal that the maximum transmission loss is limited to 1.75 dB, and the phase difference between the x- and y-polarisations remains very close to 90°, leading to an axial ratio below 3 dB, an extinction ratio higher than 15 dB, and an ellipticity above 0.94 from 205 GHz to 340 GHz as shown in Figures 5.6(d) and 5.6(e), respectively. More specifically, the measured axial ratio from 220 GHz to 330 GHz is lower than 1.25 dB that corresponds to a measured extinction ratio above 22.88 dB, while the measured ellipticity is above 0.99. The maximum frequency in the measurements is constrained by the available characterisation facility, but a general agreement with the simulation results is expected. The slight deviations between the measured and simulated results can be attributed to the unavoidable fabrication and experiment tolerances, the former of which could be dominant as suggested by further simulations. Moreover, Figure 5.6(f) illustrates the total efficiency of the proposed design, accounting for the total transmittance of the x- and y-polarisations, i.e., $(|S_{21}^{xx}|^2 + |S_{21}^{yy}|^2)/2$. The simulated total efficiency from 205 GHz to 354 GHz is higher than 77.4%, whilst the measured total efficiency from 205 GHz to 340 GHz is above 70.2%, corresponding to a measured insertion loss below 1.54 dB. It is noted that the 45° polarised incident wave with respect to the x-axis gives LHCP output waves. RHCP waves can be obtained by rotating this structure by 90° around the z-axis. Importantly, the measured results further confirm that the proposed design is robust to the metallic layer shift.

A performance comparison of the proposed work with notable existing designs from the literature is given in Table 5.3. To simplify the comparison, a figure of merit is included to quantify the bandwidth and total efficiency collectively. It can be seen that the existing designs exhibit a modest figure of merit. In general, microwave-based quarter-wave plates basically show a higher figure of merit than those at terahertz frequencies, as a result of a relatively low material loss and ease of fabrication at microwave frequencies. In the terahertz domain, most reported waveplates have limited bandwidth or efficiency, resulting in a remarkably low figure of merit. Comparing with the existing quarter-wave plates, our proposed design involves a systematic optimisation methodology and provides an advantageous bandwidth, efficiency, and figure of merit. Importantly, the design can cover a full WR-3.4 waveguide frequency band from 220 GHz to 330 GHz (Hesler *et al.*, 2007), which is technologically significant and foreseen for point-to-point terahertz communications (IEEE 802 LAN/MAN Standards Committee, 2017). Despite the restrictions in material and fabrication, the bandwidth and total efficiency of the transmitarray are the highest amongst other broadband terahertz quarter-wave plates. In addition, a high output wave polarisation purity with an axial ratio lower than

Table 5.3. Comparison between the proposed design and notable transmissive quarter-wave plates. FoM is the abbreviation of "Figure of Merit", representing the product of bandwidth and total efficiency. PEN indicates polyethylene naphthalate, while BCB denotes bisbenzocyclobutene.

Structure	Metallic Layers	Spacer Material	Centre Frequency (GHz)	Bandwidth (AR $<$ 3 dB) (%)	Minimum Efficiency (%)	FoM (%)
Microwave-based						
Meander line and loop (Fei *et al.*, 2015)	1	Duroid 5880	24	47	50	24
Cross strips (Wang *et al.*, 2020)	2	Taconic TLY-5	24	74	47	35
Strip gratings (Blanco and Sauleau, 2018)	5	Duroid 5880	27	20	93	19
Reactive surfaces (Momeni Hasan Abadi and Behdad, 2016b)	6	Duroid 6010	10	40	74	30
Terahertz-based						
Split slot ring (Euler *et al.*, 2010)	1	Silicon	325	12	45	5
Metal slots (Wang *et al.*, 2015a)	1	PEN	870	5	30	2
Metal gratings (Cong *et al.*, 2014)	2	Polyimide	1180	44	42	19
Split ring resonators (Han *et al.*, 2018)	2	BCB	980	12	62	7
This work	3	COC	280	53	70	37

1.25 dB is achieved within the frequency band of interest. The transmitarray bandwidth and efficiency enhancement can be attributed to the optimal frequency-independent circuit parameters provided by the broadband semi-analytical approach, which can deliver a constant quadrature phase difference and high transmittances for the two orthogonal electric field components over a wide bandwidth. In addition, the tri-layer transmitarray manipulates the electric and magnetic dipoles separately, further contributing to the efficiency improvement that cannot be achieved by the single- and bi-layer designs as presented in Table 5.3.

5.6 Robustness to fabrication and oblique incidence

In order to further investigate the performance of the proposed structure, this Section presents its robustness in response to spacer thickness variations, metallic layer misalignments, and obliquely incident waves.

5.6.1 Spacer thickness tolerance

Figure 5.7 illustrates the transmitarray tolerance to the spacer thickness variations. It can be seen that an axial ratio lower than 1.7 dB and a total efficiency higher than 64.6% can be sustained from 220 GHz to 330 GHz when the spacer thickness d deviates

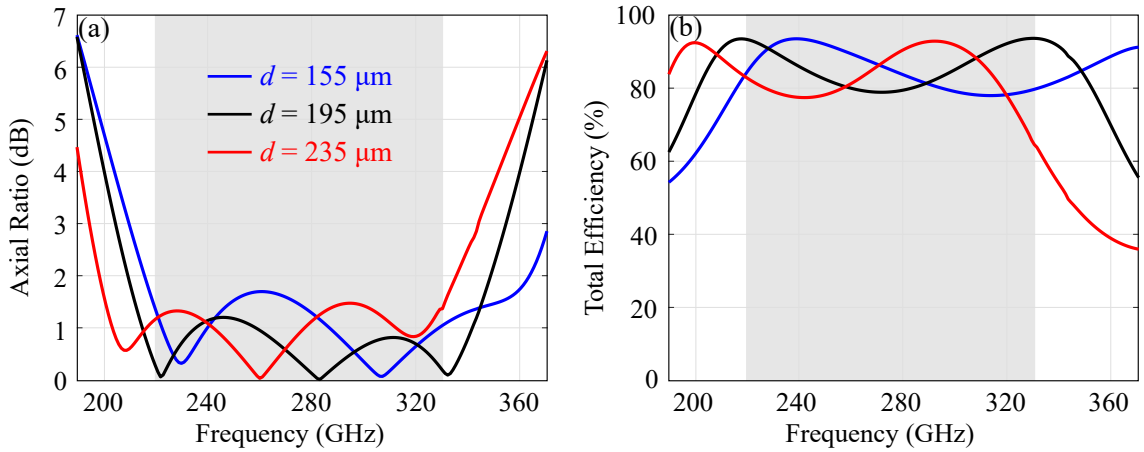

Figure 5.7. Simulated performance of the quarter-wave transmitarray with different spacer thicknesses. (a) Axial ratio and (b) total efficiency. The shaded area marks the frequency range of interest from 220 GHz to 330 GHz.

± 40 μm ($\pm 20.5\%$) from the optimal value of $d = 195$ μm. However, decreasing the spacer thickness would lead to a blue shift of the operation frequency. Figure 5.7 suggests that the proposed structure is relatively insensitive to tolerances in spacer thickness. This can be explained by the relatively large electrical spacing between the metallic layers that leads to a negligible near-field coupling.

5.6.2 Misalignment tolerance

It can be inferred from Figure 5.5 that the top metallic layer of the fabricated prototype is misaligned with respect to the middle and bottom layers, which is shifted -24 μm (4% of the unit cell size) and 48 μm along the x- and y-axes, respectively. Figure 5.8 shows the simulated transmission coefficients of the aligned and misaligned transmitarrays and confirms that the proposed structure is relatively insensitive to such a misalignment. This robustness is as a result of the homogeneity of each layer and the minimal near-field coupling among different layers. To further explore the misalignment tolerance of the transmitarray, two possible shifts of the top and bottom layers are investigated in simulations. Figure 5.9 suggests that an axial ratio below 3 dB and a total efficiency above 79.2% can be effectively maintained from 220 GHz to 330 GHz for the two scenarios, indicating that the presented transmitarray relaxes the alignment requirement in multilayer structure fabrications.

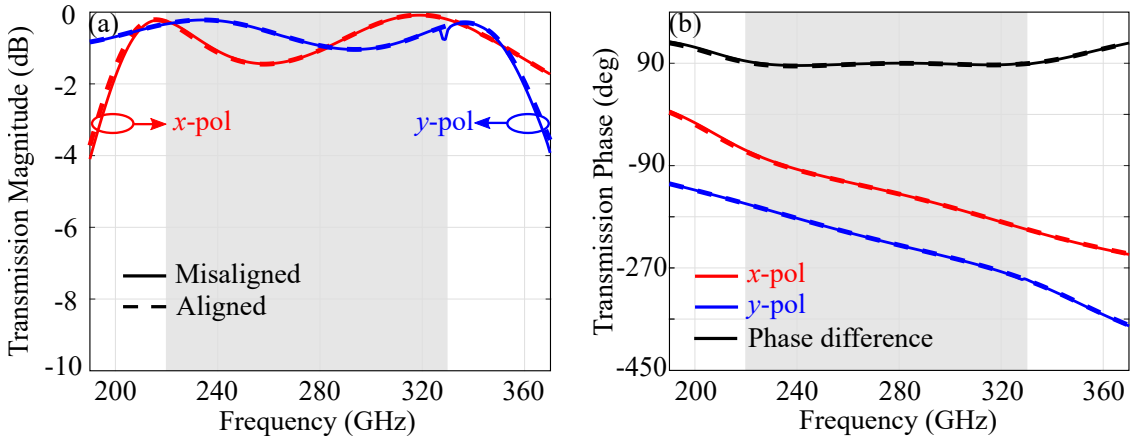

Figure 5.8. Simulated transmission coefficients of the transmitarray with and without the top layer misalignment. (a) Transmission magnitude, and (b) transmission phase. The top layer of the fabricated prototype is shifted −24 µm (4% of the unit cell size) along the x-axis and 48 µm along the y-axis, relative to the middle and bottom layers. The shaded area marks the frequency range of interest from 220 GHz to 330 GHz.

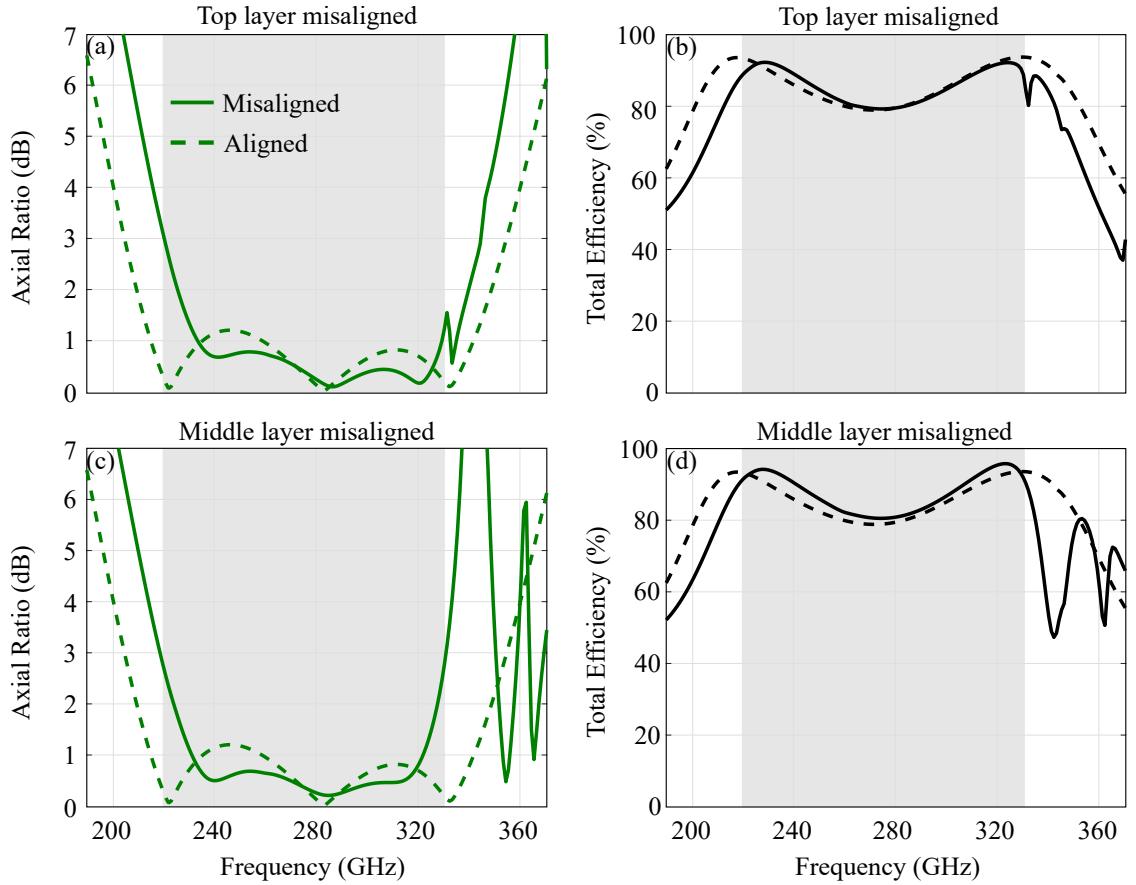

Figure 5.9. Simulated axial ratio and total efficiency of the quarter-wave transmitarray with and without misalignment. [(a, b)] Top layer shifts along the x- and y-axes are both 200 µm (37% of the unit cell size). [(c, d)] Middle layer shifts along the x- and y-axes are both 120 µm (22% of the unit cell size). The shaded area marks the frequency range of interest from 220 GHz to 330 GHz.

5.6.3 Oblique incidence

Figure 5.10 illustrates the simulated performance of the transmitarray in response to obliquely incident waves of $\theta = 10°$ in the xoz and yoz planes. It can be seen that the axial ratio is less than 2.2 dB over the frequency range of interest from 220 GHz to 330 GHz, while the minimum efficiencies in the xoz and yoz incident planes are 72.7% and 62.6%, respectively.

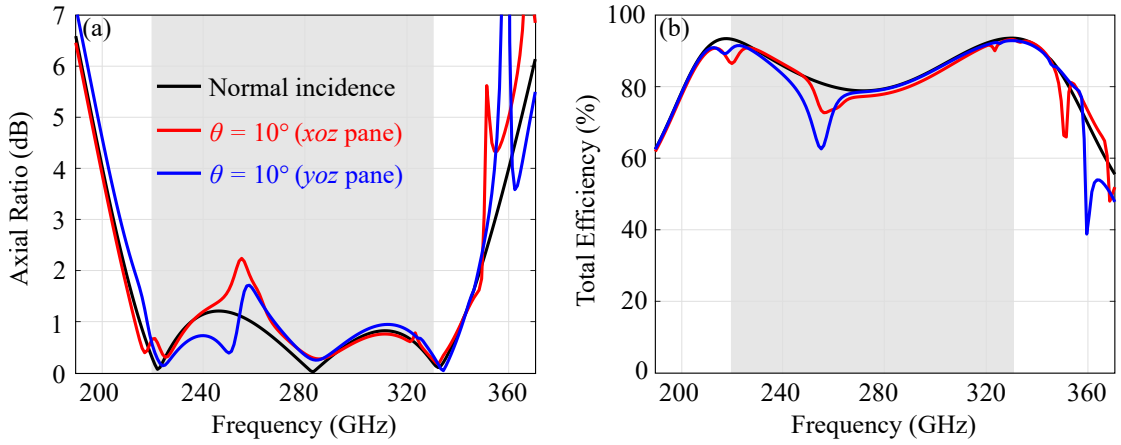

Figure 5.10. Simulated performance of the transmitarray at normal and oblique incidences. (a) Axial ratio and (b) total efficiency. The shaded area marks the frequency range of interest from 220 GHz to 330 GHz.

5.7 Conclusion

A broadband terahertz quarter-wave plate that allows linear-to-circular polarisation conversion is constructed on the basis of a three-layer transmitarray configuration. The device is developed and optimised using a broadband semi-analytical approach that targets broadband and high-efficiency performance. A measured axial ratio of less than 3 dB can be sustained from 205 GHz to at least 340 GHz, where the highest frequency is limited by the measurement facility. In addition, the proposed design demonstrates its robustness to the metallic layer misalignments. A misaligned fabricated prototype with its top layer shifted -4% of the unit cell size along the x-axis and 8% of the unit cell size along the y-axis shows a close transmission performance with the aligned structure. As such, the proposed transmitarray relaxes the fabrication requirements at terahertz frequencies. This quarter-wave transmitarray design can be readily integrated into compact terahertz systems for diverse applications.

Chapter 6

Broadband terahertz half-wave transmitarray

IN this Chapter, we numerically and experimentally demonstrate a terahertz half-wave transmitarray. To overcome the bandwidth and efficiency limitations associated with conventional bulky wave-plates, the concept of Huygens' surface is adopted for this design. The transmitarray is designed to emulate the optimal frequency-independent circuit parameters provided by a broadband semi-analytical approach. Simulation results of an optimal design suggest that a 15-dB extinction ratio can be sustained from 219 GHz to 334 GHz, corresponding to a fractional bandwidth of 41.6% or an entire terahertz electronics band, while the cross-polarisation transmission efficiency is above 72.3%. The measured results indicate that the fabricated structure enables a 15-dB extinction ratio from 220 GHz to 303 GHz with a cross-polarisation transmission efficiency beyond 76.7%. This half-wave transmitarray design can be useful for studies of chiral structures in biology and chemistry, and for polarisation diversity in communications.

6.1 Introduction

We presented a terahertz quarter-wave transmitarray in Chapter 5, which is capable of realising linear-to-circular polarisation conversion upon transmission over a wide bandwidth. The presented quarter-wave transmitarray was designed with an assistance from the broadband semi-analytical approach presented in Chapter 4, and it overcomes the limitations set by conventional bulky waveplates made of natural birefringent materials. In order to further investigate the capability of the broadband approach and to develop functional devices for imaging and communications, we present a half-wave transmitarray design in this Chapter. The design can convert linearly or circularly polarised incident waves into their orthogonal counterparts.

Despite the fact that various transmitarray-based half-wave plates have been developed across the electromagnetic spectrum, from microwave (Khan and Tahir, 2017), terahertz (Ako *et al.*, 2020a; Moreno-Peñarrubia *et al.*, 2020), to optical frequencies (Kruk *et al.*, 2016; Liu *et al.*, 2017), most existing designs merely manipulate the electric field of incident waves, resulting in a limited efficiency. In addition to that, challenges associated with fabrication complexity and high material losses further contribute to efficiency degradation at terahertz frequencies. To enhance efficiency and transmission phase coverage, the concept of "Huygens' surface" was introduced by Pfeiffer and Grbic (Pfeiffer and Grbic, 2013b; Pfeiffer and Grbic, 2013c; Pfeiffer *et al.*, 2014). Each unit cell of a Huygens' surface can be considered as a combination of orthogonally arranged infinitesimal electric and magnetic dipoles. By controlling the resonance of these electric and magnetic dipoles, a large transmission phase coverage accompanied with high transmittance can be obtained (Decker *et al.*, 2015).

In this Chapter, we present a three-layer terahertz half-wave transmitarray with enhanced bandwidth and efficiency. The presented half-wave transmitarray aims to cover the WR-3.4 waveguide frequency band, spanning 220 GHz to 330 GHz (Hesler *et al.*, 2007), which is foreseen for point-to-point terahertz communications (IEEE 802 LAN/MAN Standards Committee, 2017). Relying on the concept of Huygens' surface, the proposed structure cascades three metallic layers to form circulating electric currents, so as to generate a magnetic response. The three metallic layers in combination can be represented by equivalent circuit models, which describe the response to orthogonal linearly-polarised incident waves. The broadband approach of Chapter 4 is employed to facilitate design and optimisation by providing frequency-independent circuit parameters. A physical realisation of each metallic layer is subsequently carried

out to reproduce these optimal circuit parameters. To verify the design, the half-wave transmitarray has been fabricated and experimentally evaluated.

6.2 Design

We consider a transmitarray cascading three metallic layers separated by two dielectric spacers as illustrated in Figure 6.1. A minimum of three metallic layers are needed to gain a full control over the electric and magnetic responses (Pfeiffer *et al.*, 2014), so that the transmitarray can produce an arbitrary transmission phase together with high transmittance. Two equivalent circuits are required for each metallic layer to describe the responses to the x- and y-polarisations. The equivalent circuits can be purely inductive or capacitive, or series or parallel combination between them. In order to simplify the design, metals are assumed to be lossless. To illustrate the admittance tensor of each metallic layer, we assume here an i^{th} metallic layer that provides purely inductive and capacitive responses for the x- and y-polarisations, respectively. Therefore, its corresponding admittance tensor can be written as

$$\mathbf{Y_{si}} = \begin{bmatrix} 1/(j\omega L_{\text{x}i}) & 0 \\ 0 & j\omega C_{\text{y}i} \end{bmatrix}, \tag{6.1}$$

where $L_{\text{x}i}$ and $C_{\text{y}i}$ are the equivalent inductance and capacitance along the x- and y-axes, respectively. For a mirror-symmetric pattern, the cross-coupling of each metallic layer is negligible, hence the off-diagonal elements are equal to zero. Ultra-low loss cyclic olefin copolymer (COC) is employed for the dielectric spacers in the design to minimise the material loss. These dielectric spacers can be represented by transmission line sections with permittivity-determined wavenumber and wave impedance in the

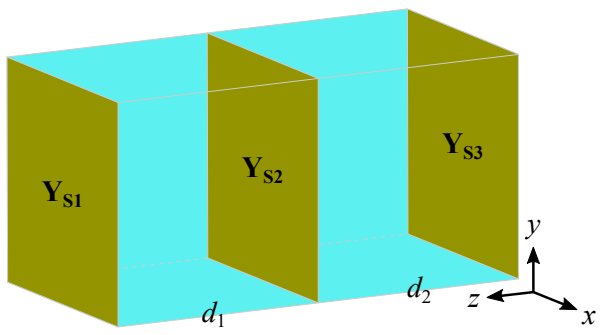

Figure 6.1. Schematic illustration of a three-layer transmitarray unit cell. The transmitarray is comprised of three metallic layers and two subwavelength dielectric spacers.

analytical approach. COC presents a relative permittivity of $\epsilon_r = 2.33$ and loss tangent of $\tan\delta = 0.0005$ from 220 GHz to 330 GHz (Nielsen *et al.*, 2009). The cumulative response of the entire transmitarray can be calculated by using Equations (6.1), (4.2), and (4.3).

As an objective, a broadband and highly efficient half-wave transmitarray is anticipated to provide an identical and near-unity transmittance for the x- and y-polarisations, and a constant phase difference of 180° between them over a wide bandwidth. To set a constraint, the possible range of achievable inductance and capacitance within a unit cell of certain size is explored via 3D full-wave simulations, where metallic patterns of different equivalent circuits under a specific polarisation are implemented. To minimise the near-field coupling between the metallic layers and taking fabrication feasibility into consideration, a dielectric spacer thickness range between 100 μm and 200 μm is specified within the frequency band of interest from 220 GHz to 330 GHz. With objectives and constraints identified, the outlined broadband semi-analytical approach is employed to find the optimal frequency-independent circuit parameters (L_{xi}, C_{yi}) for the i^{th} metallic layer, as well as the thicknesses of dielectric spacers. Optimisation of the circuit model reveals that the desired performance can be achieved by employing metallic layers that provide purely inductive and capacitive responses for the x- and y-polarisations, respectively. Table 6.1 details the optimal frequency-independent circuit parameters provided by this approach for an optimal half-wave transmitarray, and the dielectric spacer thicknesses are determined to be $d_1 = d_2 = 115$ μm.

In order to realise the half-wave transmitarray, patterns that provide near purely inductive responses for the x-polarisation and near purely capacitive responses for the y-polarisation are designed following the procedure presented in Chapter 4. Electromagnetic simulations are carried out with the commercial software ANSYS HFSS. Gold is implemented for each metallic layer to minimise the metal loss and its surface impedance at terahertz frequencies is described by a Drude model (Lucyszyn, 2007). In order to avoid diffraction and to make the structure relatively insensitive to obliquely incident

Table 6.1. Calculated optimal frequency-independent circuit parameters provided by the broadband semi-analytical approach. The units for inductances and capacitances are pH and fF, respectively.

Top layer		Middle layer		Bottom layer	
L_{x1}	C_{y1}	L_{x2}	C_{y2}	L_{x3}	C_{y3}
193.9	2.4	321.1	4.6	270.7	2.8

waves, a subwavelength lattice constant of $a = 300$ µm is selected, which is equal to $0.33\lambda_0$ at 330 GHz. Figure 6.2 illustrates the unit cell geometry of the proposed optimal half-wave transmitarray, while its dimensions are detailed in Table 6.2. In Figure 6.2, a thin metallic strip oriented along the x-axis is determined for each metallic layer to provide a relatively high equivalent inductance, while metallic patches are in parallel along the y-axis to introduce a high equivalent total capacitance but a minimised total inductance. Moreover, the metallic patches are in series along the x-axis, so that the corresponding equivalent capacitance can be minimised. The mentioned optimal thickness of 115 µm suggested from circuit optimisation for each dielectric spacer was determined based on the assumption of negligible near-field coupling between the metallic layers. However, 3D full-wave simulation reveals that a weak near-field coupling exists and leads to a blue shift of the operation frequency. Hence, 125 µm-thick COC spacers are adopted for the physically realised structure to alleviate the coupling effect and shift the centre operation frequency to ∼275 GHz.

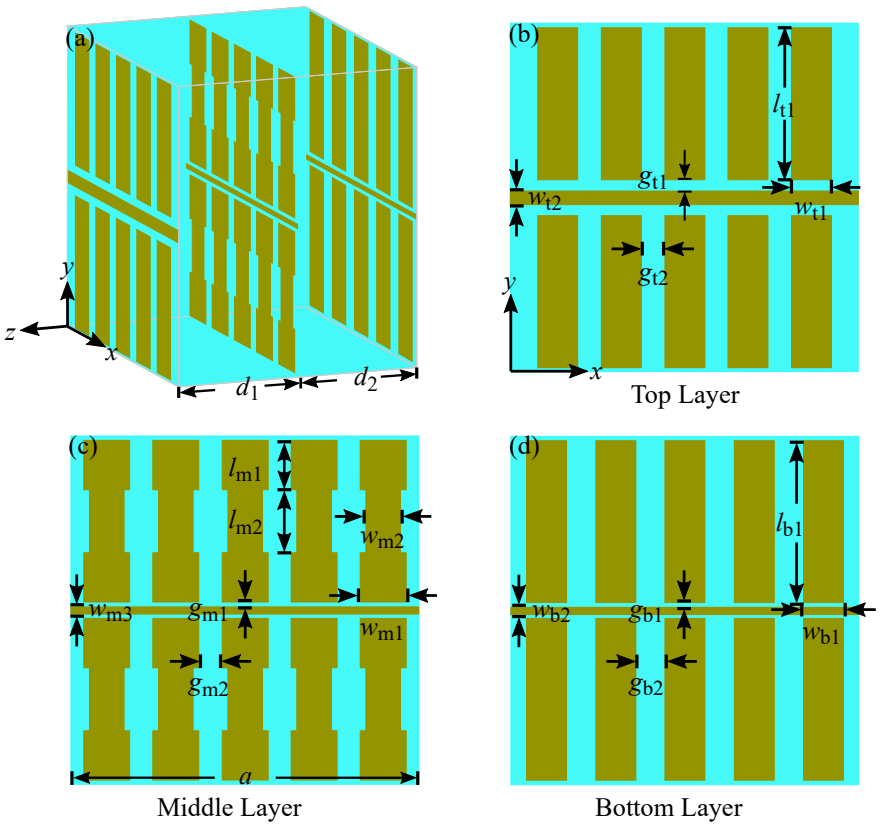

Figure 6.2. Unit cell geometry of the optimal half-wave transmitarray. (a) 3D schematic view of a complete unit cell, (b) top, (c) middle, and (d) bottom metallic layers.

Table 6.2. Geometrical parameters of the optimal half-wave transmitarray unit cell. The units are in μm.

Parameter	Value	Parameter	Value	Parameter	Value	Parameter	Value
a	300	w_{t2}	11	w_{m1}	40	l_{b1}	140
d_1	125	g_{t1}	9	w_{m2}	28	w_{b1}	35
d_2	125	g_{t2}	20	w_{m3}	4	w_{b2}	5
l_{t1}	132	l_{m1}	43	g_{m1}	5	g_{b1}	5
w_{t1}	35	l_{m2}	54	g_{m2}	20	g_{b2}	25

Figure 6.3 shows the complex transmission coefficients provided by the broadband semi-analytical approach and the 3D full-wave simulation. A reasonable agreement between the calculated and simulated results is achieved, while the slight deviation between them can be attributed to a weak near-field coupling between the metallic layers, and the non-negligible capacitances and inductances along the x- and y-polarisations, respectively. Figure 6.3(a) indicates that the maximum simulated insertion losses from 220 GHz to 330 GHz for the x- and y-polarisations are 2.84 dB and 1.02 dB, respectively, while Figure 6.3(b) suggests that the simulated transmission phase difference between the two orthogonal polarisations remains close to 180° within the targeted band. These results suggest that the optimisation can reasonably satisfy the objectives to realise a

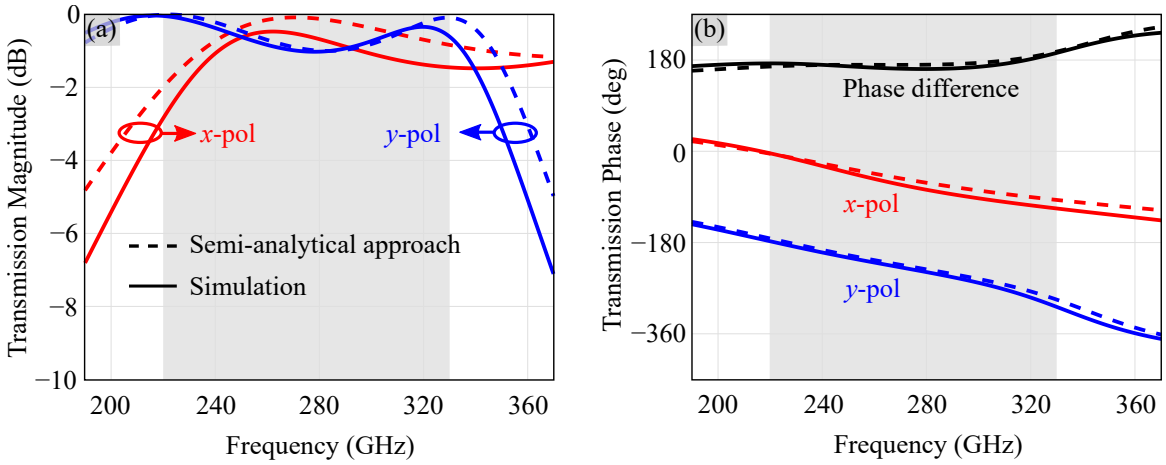

Figure 6.3. Calculated and simulated complex transmission coefficients of the optimal half-wave transmitarray provided by the broadband semi-analytical approach and the 3D full-wave simulation. (a) Transmission magnitude and (b) transmission phase. The shaded area marks the frequency range of interest from 220 GHz to 330 GHz, defined for the WR-3.4 waveguide band.

broadband half-wave transmitarray. In order to further validate the performance of the proposed structure, a half-wave transmitarray is fabricated.

6.3 Fabrication and measurement

Images of the fabricated sample are shown in Figure 6.4. The sample was manufactured by the Functional Materials and Microsystems Research Group and the Micro Nano Research Facility at RMIT University. The fabrication process is described in Section 5.3, while the half-wave transmitarray experimental setup is similar to that provided in Section 5.4. It is noted that the transmission coefficients of the sample under the x- and y-polarisations are measured by rotating the sample by 90° and 0° around the propagation axis, respectively. For the co- and cross-polarisations transmission measurements, the sample is rotated by 45°, and a twist waveguide is attached to the receiver for the cross-polarisation measurement. Additionally, a reference measurement is taken for normalisation in the absence of the sample.

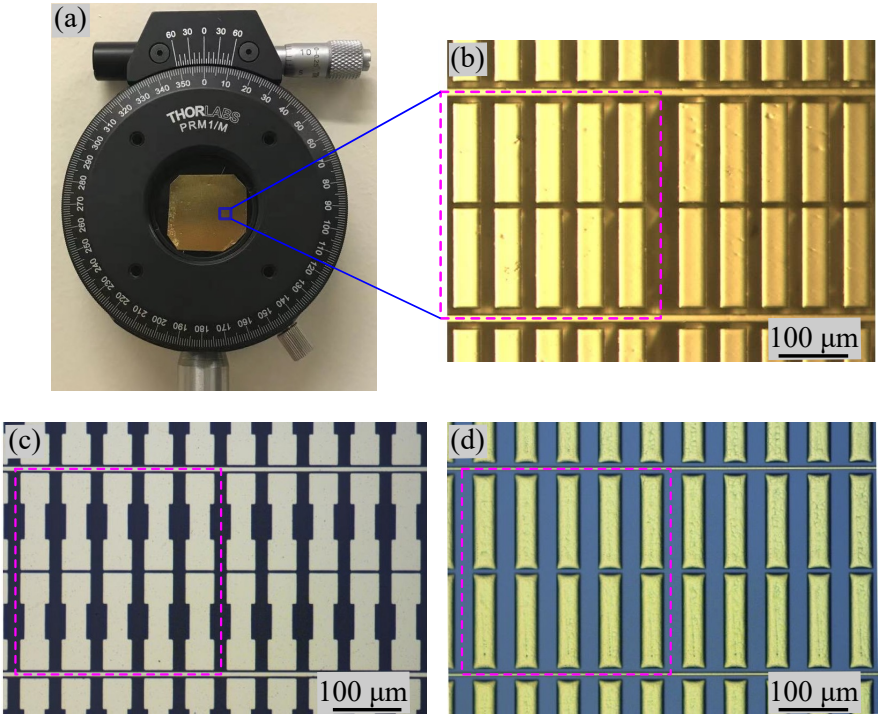

Figure 6.4. Fabricated three-layer half-wave transmitarray prototype. (a) Photograph of the fabricated sample. Magnified view of (b) top, (c) middle, and (d) bottom metallic layers. All metallic layers are made of gold, and the color difference in three layers is due to lighting condition. The bottom metallic layer in (d) is covered by COC. The dashed lines outline an area containing a unit cell.

6.4 Results

Figure 6.5 illustrates the performance comparison between the simulated responses of the optimal design and the measured results of the fabricated half-wave transmitarray. Figure 6.5(a) suggests that the maximum measured insertion losses from 220 GHz to 330 GHz for the x- and y-polarisations are 2.76 dB and 4.77 dB, respectively. In Figure 6.5(b), the transmission phase difference between the x- and y-polarisations remains close to 180°. To rigorously quantify the performance of the fabricated structure, its co- and cross-polarisations transmission magnitudes are measured directly and also are reconstructed based on the independently measured complex transmission coefficients of the x- and y-polarisations. In Figures 6.5(c-f), a close agreement between the directly measured and reconstructed results can be obtained, while the deviation between them can be attributed to the experimental misalignments. In Figure 6.5(c), the maximum simulated and directly measured cross-polarisation insertion losses from 220 GHz to 330 GHz are 1.37 dB and 2.98 dB, respectively. In Figure 6.5(d), the directly measured co-polarisation transmission magnitude remains lower than -13.0 dB.

The simulated and measured results imply that the proposed half-wave transmitarray is also capable of inverting the handedness of circularly polarised waves. The circular polarisation purity of the transmitted waves can be determined indirectly by employing the transmission magnitudes of the linear co- and cross-polarisations. It is worth noting that the axial ratio is commonly adopted to characterise the circular polarisation purity in the microwave literature, while the extinction ratio serves the same purpose in optics. Moreover, an acceptable maximum 3-dB axial ratio corresponds to an extinction ratio of $\sim$15 dB (see Appendix A). Hence, the 15-dB extinction ratio criterion is employed to characterise the half-wave transmitarray. In Figures 6.5(e) and 6.5(f), a simulated 15-dB extinction ratio relative bandwidth of 41.6% can be maintained from 219 GHz to 334 GHz, while the simulated cross-polarisation transmission efficiency is beyond 72.3%. The extinction ratio evaluated based on the directly measured results reveals that the fabricated half-wave transmitarray enables a 15-dB extinction ratio fractional bandwidth of at least 31.7% from 220 GHz to 303 GHz, where the lower frequency bound is limited by the available measurement facility. Moreover, a minimum measured efficiency of 76.7% can be sustained from 220 GHz to 303 GHz. It is noted that the evaluated extinction ratio quantities are the same for both linearly and circularly polarised transmitted waves.

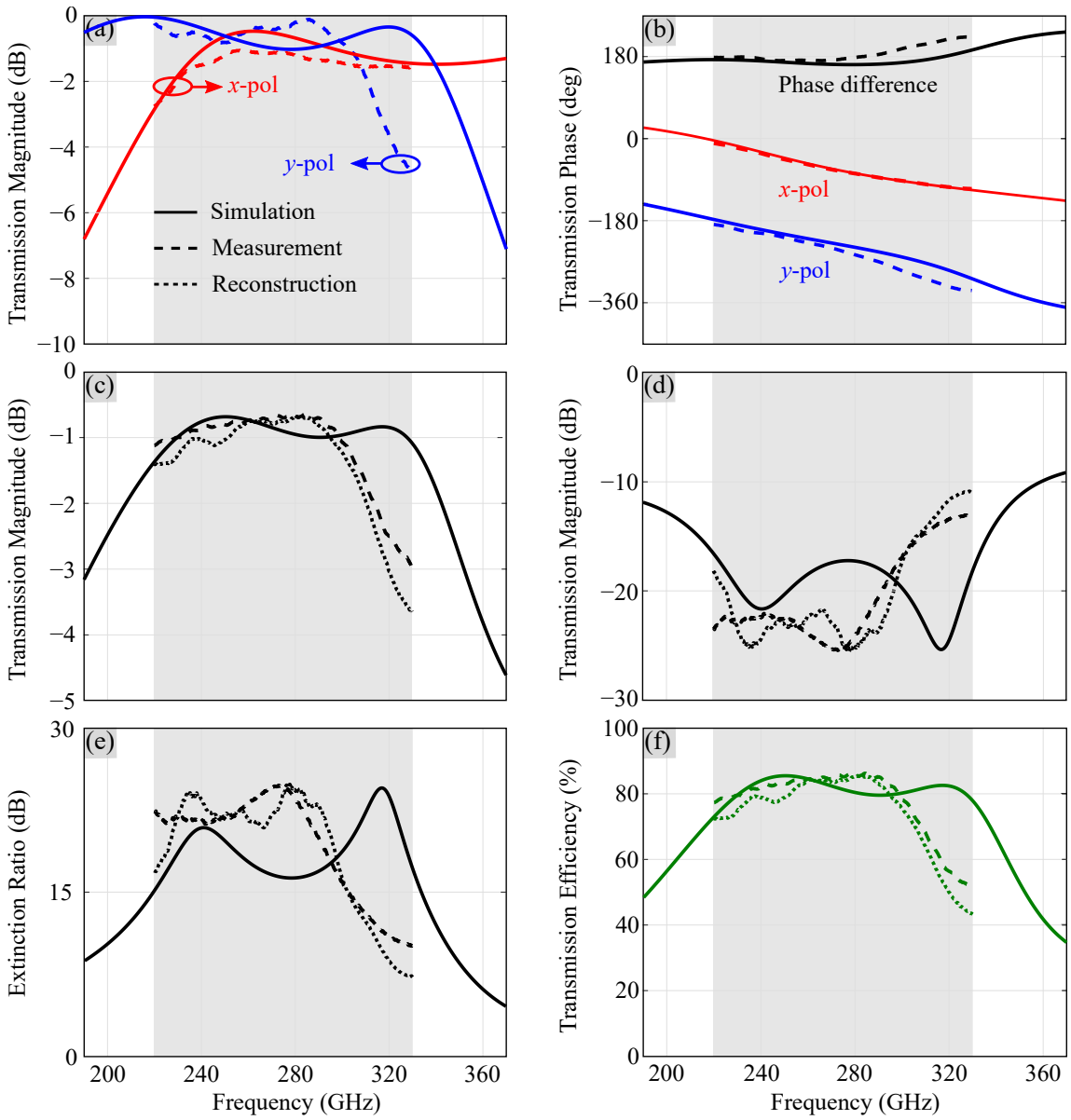

Figure 6.5. Performance comparison between the simulated responses of the optimal design and the measured results of the fabricated transmitarray. (a) Transmission magnitudes and (b) transmission phases for the x- and y-polarisations, (c) cross-polarisation transmission magnitude, (d) co-polarisation transmission magnitude, (e) extinction ratio, and (f) cross-polarisation transmission efficiency. The measured transmission coefficients are normalised to a reference measurement conducted without the presence of the sample. Reconstruction indicates that the results are evaluated based on the measured complex transmission coefficients of the x- and y-polarisations, i.e., $T_{\text{cross}} = \left(T_{\text{xx}} - T_{\text{yy}}\right)/2$ and $T_{\text{co}} = \left(T_{\text{xx}} + T_{\text{yy}}\right)/2$, where T_{xx}, T_{yy}, T_{cross} and T_{co} are the complex transmission coefficients of the x-, y-, cross-, and co-polarisations, respectively. The extinction ratio is defined as $\text{ER} = 10\log_{10}\left(|T_{\text{cross}}|^2/|T_{\text{co}}|^2\right)$, which yields the same value for both linear and circular polarisations. The efficiency accounts for the transmittance of cross-polarisation, i.e., $|T_{\text{cross}}|^2$.

A performance comparison between the fabricated half-wave transmitarray and existing representative transmissive half-wave plates from the literature is given in Table 6.3. The fabricated half-wave transmitarray provides a superior performance over the existing designs in term of the 15-dB extinction ratio relative bandwidth and the cross-polarisation transmission efficiency. The metal-mesh achromatic half-wave plate employed six layers to provide similar bandwidth and efficiency at around 90 GHz (Pisano *et al.*, 2012). However, multilayer structures pose additional complexities for micro-fabrication at terahertz frequencies. In other reports, all-dielectric structures were implemented to function as half-wave plates, but exhibited a substantial thickness and a limited relative bandwidth (Chen *et al.*, 2016b; Zi *et al.*, 2018). Due to the fact that a single- or bi-layer transmitarray cannot achieve full control of the electric and magnetic responses, the designs presented by Moreno-Peñarrubia *et al.* (2020) and Nakata *et al.* (2017) exhibited a limited relative bandwidth. The superior performance of the fabricated half-wave transmitarray can be ascribed to the involvement of a systematic optimisation methodology and a complete control of the electric and magnetic responses.

Figure 6.6 shows the simulated performance of the optimal half-wave transmitarray in response to obliquely incident waves. Both the 15-dB extinction ratio relative bandwidth and efficiency decrease with a larger angle of incidence. However, reasonable performance can be maintained up to an incidence angle of 45°. The robustness of the optimal half-wave transmitarray to obliquely incident waves can be attributed to the

Table 6.3. Comparison between the fabricated half-wave transmitarray and notable existing transmissive half-wave plates. The structures operate around the same frequency range. All results are experimentally confirmed values.

Structure	Centre frequency (GHz)	Dielectric material	Metallic layers	Bandwidth (ER $>$ 15 dB) (%)	Minimum efficiency (%)
Metal mesh (Pisano *et al.*, 2012)	90	Polypropylene	6	31.4	71.3
Zigzag transmitarray (Moreno-Peñarrubia *et al.*, 2020)	150	Polypropylene	2	4.8	74.4
Cut-wire pairs (Nakata *et al.*, 2017)	500	COC	2	0.6	66.3
Elliptical pillar array (Zi *et al.*, 2018)	999	Silicon	Bi-layered all-dielectric	5.5	58.8
Gradient gratings (Chen *et al.*, 2016b)	1074	Silicon	Single-layered all-dielectric	4.5	68.1
This work	262	COC	3	$>$ 31.7	76.7

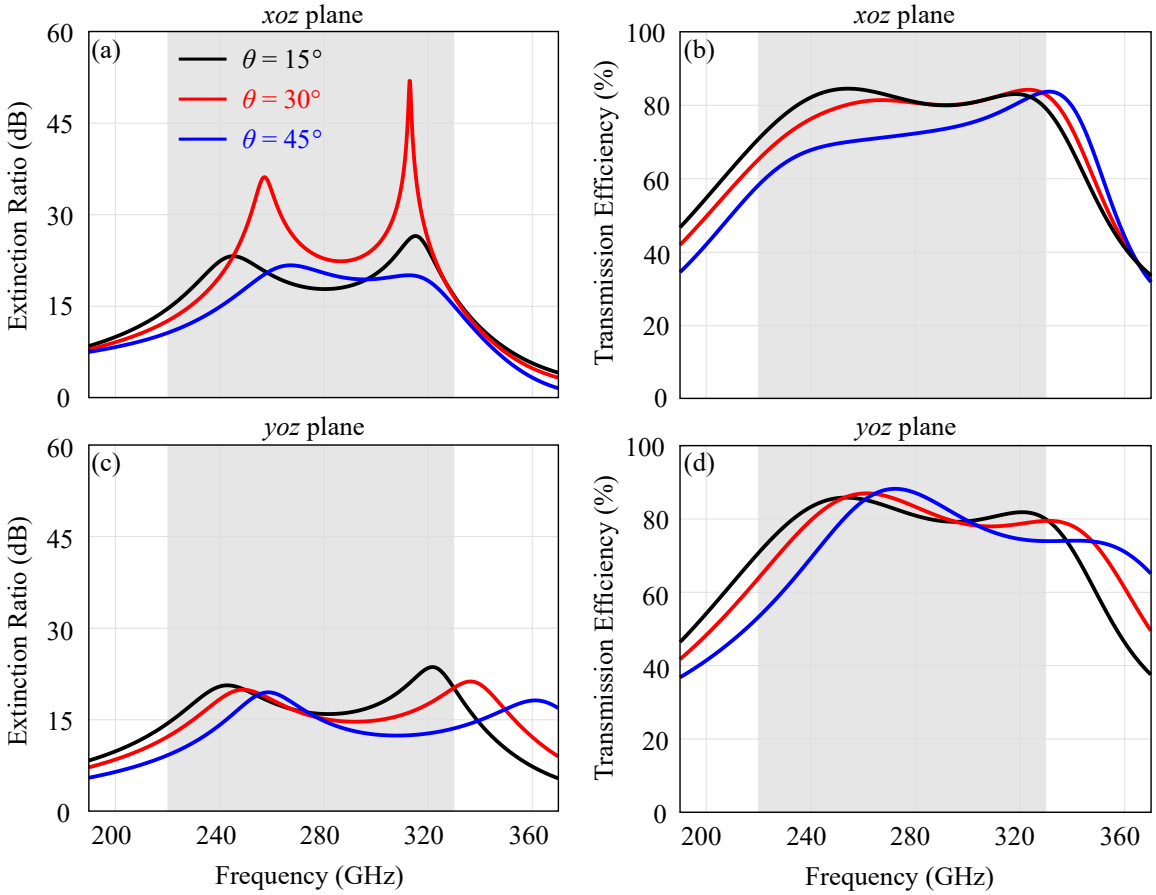

Figure 6.6. Simulated extinction ratio and cross-polarisation transmission efficiency of the optimal half-wave transmitarray in response to obliquely incident waves. [(a, b)] in the *xoz*-plane and [(c, d)] in the *yoz*-plane. The shaded area marks the frequency range of interest from 220 GHz to 330 GHz, defined for the WR-3.4 waveguide band.

implementation of a relatively small unit cell ($a = 0.33\lambda_0$ at 330 GHz) together with thin dielectric spacers ($d_1 = d_2 = 0.14\lambda_0$ at 330 GHz). A small unit cell leads to a limited phase difference between the unit cell edges under obliquely incident waves, while thin dielectric spacers result in a small path length variation at oblique incidence.

6.5 Fabrication tolerance

In order to explain the performance discrepancy between the simulated responses of the optimal design and the measured results shown in Figure 6.5, further simulations are carried out with unit cell dimensions taken from the fabricated sample. Figure 6.7 shows the simulated and measured results of the fabricated structure, and a reasonable

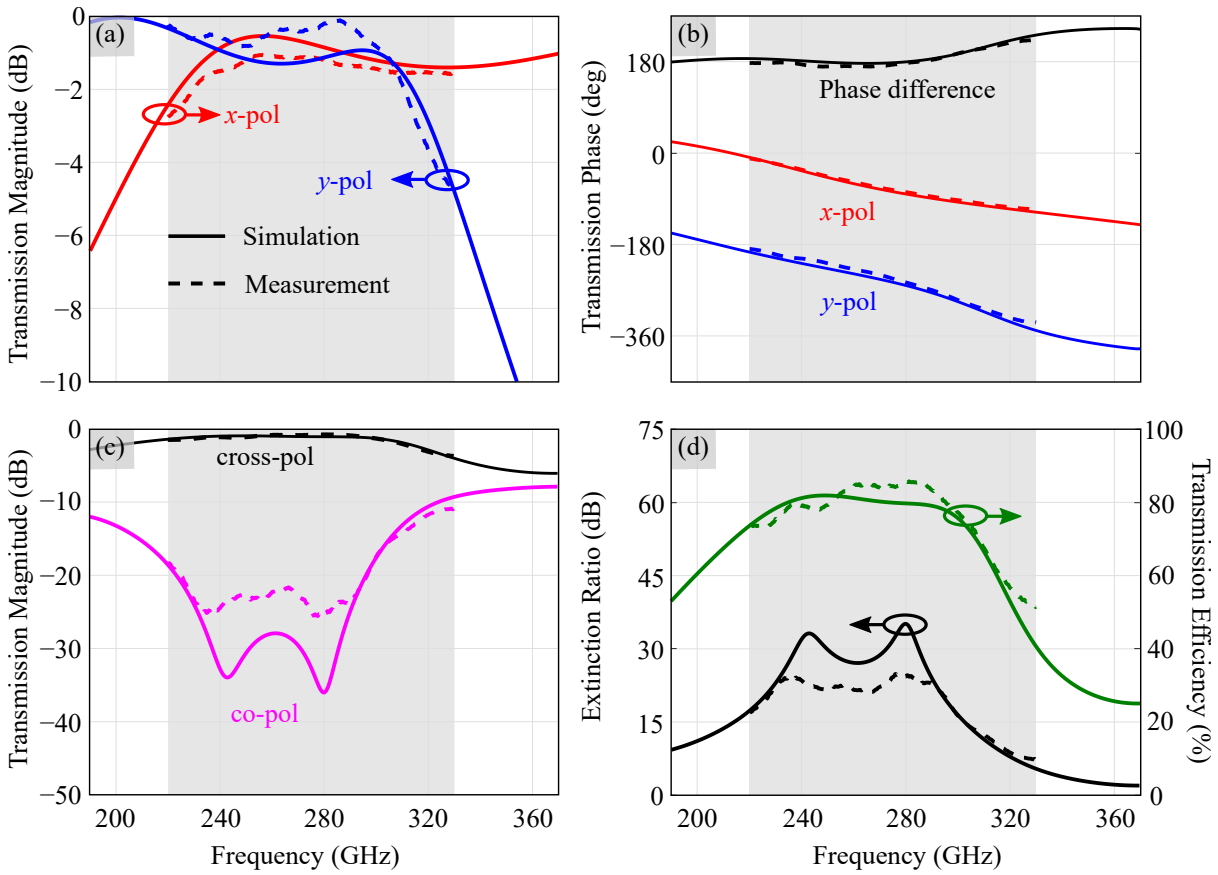

Figure 6.7. Simulated and measured performance of the fabricated half-wave transmitarray. (a) Transmission magnitudes and (b) transmission phases for the x- and y-polarisations, (c) co- and cross-polarisations transmission magnitudes, (d) extinction ratio and cross-polarisation transmission efficiency. The shaded area marks the frequency range of interest from 220 GHz to 330 GHz, defined for the WR-3.4 waveguide band. The altered unit cell geometrical parameters are detailed as follows: $l_{m2} = 56$ µm, $d_1 = 129$ µm, and $d_2 = 129$ µm.

agreement between them is achieved. It can be inferred from Figure 6.7 that the performance deviation between the optimal design and the fabricated structure is likely caused by the fabrication tolerances.

6.6 Conclusion

We have numerically and experimentally demonstrated a terahertz half-wave transmitarray that is capable of converting linearly or circularly polarised waves into their orthogonal counterparts. For the optimal design, a simulated 15-dB extinction ratio relative bandwidth of 41.6% can be achieved, namely from 219 GHz to 334 GHz. The superior performance of the half-wave transmitarray over the existing representative

designs can be ascribed to the involvement of a systematic optimisation approach and a complete control of the electric and magnetic responses. Owing to the employment of a relatively small unit cell ($0.33\lambda_0$ at 330 GHz) and thin dielectric spacers ($0.14\lambda_0$ at 330 GHz), the optimal half-wave transmitarray is robust to obliquely incident waves up to an angle of 45°. The half-wave transmitarray can be scaled to operation at nearby frequency bands, and has potential applications in imaging, spectroscopy, and wireless communications.

Chapter 7

Mechanically tunable terahertz circular polariser

CIRCULAR polarisers that selectively transmit only one handedness of circular polarisation are useful for imaging and wireless communications. Conventional ways of realising circular polarisers involve three-dimensional chiral structures, which typically introduce strong bianisotropic responses only over a narrow bandwidth, and also impose fabrication challenges. To overcome the limitations associated with conventional non-planar designs, we present here a three-layer transmitarray-based planar circular polariser exhibiting designable bianisotropy. The proposed circular polariser design involves a systematic procedure similar to that presented in Chapter 4. Specific to this design, a pattern rotation is implemented to introduce magneto-electric coupling, so as to create bianisotropic responses. Simulation results reveal that a 15-dB extinction ratio can be sustained from 251 GHz to 298 GHz leading to a fractional bandwidth of 17.1% with a transmission magnitude higher than −0.45 dB. This simulated 15-dB extinction ratio relative bandwidth is nearly twice that of a previously published transmitarray-based corresponding device. Importantly, the presented circular polariser can operate at nearby frequency bands by mechanically tuning the air gap spacings between the three metallic layers. Furthermore, the proposed structure can function as a quasi-half-wave plate by simply rotating the top or bottom metallic layer.

7.1 Introduction

In nature, a myriad of biological molecules such as glucose, amino acids, and enzymes provide unique signatures in response to different handednesses of incident circular polarisations. Different optical responses can be explained in terms of the circular dichroism and bianisotropy, which are commonly found in chiral molecules. Inspired by the functionalities of chiral molecules, artificial three-dimensional chiral structures such as helices (Yang *et al.*, 2010b), metafoils (Wu *et al.*, 2014), and microcoils (Waselikowski *et al.*, 2010) have been employed to introduce chirality for various novel applications, including optical activity (Wu *et al.*, 2013), negative refractive index (Zhang *et al.*, 2009), polarisation-dependent absorption (Cheng *et al.*, 2018), and polarisation conversion (Cheng and Cheng, 2019). Among those bianisotropic devices, circular polarisers are utilised to filter the circular polarisation of one handedness, and they are highly demanded in spectroscopy (Ranjbar and Gill, 2009), imaging (Patty *et al.*, 2018), and space applications (Sanz-Fernández *et al.*, 2015).

In optics, circular polarisers can be realised by implementing cholesteric liquid crystals (De Vries, 1951) that utilise Bragg reflection, and helical arrays (Gansel *et al.*, 2009, 2012) that exhibit inherent chirality as a result of their three-dimensional chiral structures. However, circular polarisers made of such structures typically feature narrow bandwidth and a relatively low extinction ratio, defined as a difference in the transmission between the two handednesses. Stacking multiple circular polarisers is beneficial to bandwidth enhancement, but at the expense of a high transmission loss, bulky structure, and complicated fabrication processes (Huang *et al.*, 2007).

Instead of non-planar chiral structures, it was shown that planar multilayer structures are a viable alternative for realising designable bianisotropy with low profile and reduced fabrication complexity. However, despite the fact that various planar structures were developed to act as circular polarisers, their performance remains to be further improved. In the microwave engineering community, a miniaturised-element frequency-selective surface designed with the help of equivalent circuit models was proposed as a circular polariser, which maintained a simulated 15-dB extinction ratio relative bandwidth of only 2.0% (Momeni Hasan Abadi and Behdad, 2016a). Moreover, this circular polariser employed fourteen metallic layers and ten substrates, making it difficult for scaling to operate at higher frequencies due to the fabrication constraints. In the millimetre-wave domain, a tri-layer transmitarray-based circular polariser was designed using a systematic approach, and exhibited a simulated 15-dB extinction ratio

fractional bandwidth of 9.0% (Pfeiffer and Grbic, 2014). In the optics region, a broadband bianisotropic response was obtained by stacking nanorod arrays with a tailored rotational twist (Zhao *et al.*, 2012). This twisted optical structure involved a generalised Bloch analysis in combination with transmission-line theory to determine the metallic layer rotation angles, while its extinction ratio demanded further enhancement.

To overcome the limitations associated with the existing designs. We propose here a transmitarray-based circular polariser that enables an extinction ratio higher than 15 dB from 251 GHz to 298 GHz, equivalent to a relative bandwidth of 17.1% with a transmission magnitude above -0.45 dB. The presented circular polariser is developed with an aid from the broadband semi-analytical approach presented in Chapter 4, and resulting in wideband anisotropic responses without involving complicated fabrication processes. Importantly, frequency tunability covering the entire WR-3.4 waveguide frequency band from 220 GHz to 330 GHz (Hesler *et al.*, 2007) can be achieved by mechanically adjusting the air gap spacings between the metallic layers. Moreover, the proposed structure can function as a transmissive quasi-half-wave plate by rotating the top or bottom metallic layer.

7.2 Design

As illustrated in Figure 7.1, we consider a transmitarray composed of three metallic layers on three subwavelength dielectric substrates that are separated by two air gaps. The employment of three metallic layers allows a complete control of the electric and magnetic responses to incident waves, so as to enhance the transmission phase coverage

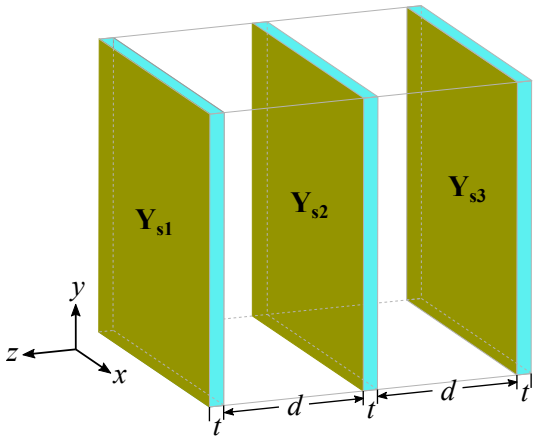

Figure 7.1. Schematic of a tri-layer transmitarray unit cell. The transmitarray consists of three metallic layers each on a substrate, and they are separated by two air gaps.

and transmission efficiency (Pfeiffer *et al.*, 2014). In order to facilitate the transmitarray design and optimisation, we employ the broadband semi-analytical approach. Hence, we choose a particular category of pattern for each metallic layer, whose electromagnetic responses to the x- and y-polarised incident waves can be described by two distinct equivalent circuit models. The circuit model for one specific polarisation can be a parallel LC circuit, a series LC circuit, purely inductive or capacitive circuits. Metals are assumed to be lossless to simplify the analysis. To illustrate the admittance tensor of each layer, we assume here an i^{th} metallic layer provides purely inductive and capacitive responses to the x- and y-polarised waves, respectively. Thus, its admittance tensor can be expressed as

$$\mathbf{Y_{si}} = \begin{bmatrix} 1/(j\omega L_{\text{x}i}) & 0 \\ 0 & j\omega C_{\text{y}i} \end{bmatrix}, \tag{7.1}$$

where $L_{\text{x}i}$ and $C_{\text{y}i}$ are the equivalent inductance and capacitance along the x- and y-polarisations, respectively. To introduce the magneto-electric coupling, the i^{th} metallic layer is anti-clockwise rotated by an angle of φ_i, and the rotation angle is limited to an integer multiple of 45° to avoid losing pattern connectivity with the neighbouring unit cells. The admittance tensor of the i^{th} metallic layer then becomes (Zhao *et al.*, 2011)

$$\mathbf{Y'_{si}} = \mathbf{R_i}\mathbf{Y_{si}}\mathbf{R_i^{\text{T}}}, \tag{7.2}$$

where $\mathbf{R_i}$ is the rotation matrix that can be written as

$$\mathbf{R_i} = \begin{bmatrix} \cos\varphi_i & \sin\varphi_i \\ -\sin\varphi_i & \cos\varphi_i \end{bmatrix}. \tag{7.3}$$

Each dielectric substrate and air gap can be represented by a transmission line section along the wave propagation direction as indicated in Equation (4.2). Therefore, the **ABCD** transfer matrix of the structure shown in Figure 7.1 can be written as

$$\begin{aligned} \begin{bmatrix} \mathbf{A} & \mathbf{B} \\ \mathbf{C} & \mathbf{D} \end{bmatrix} = {} & \begin{bmatrix} \mathbf{I} & \mathbf{0} \\ \mathbf{nY'_{s1}} & \mathbf{I} \end{bmatrix} \begin{bmatrix} \cos(k_{\text{d}}t)\mathbf{I} & -j\sin(k_{\text{d}}t)\eta_{\text{d}}\mathbf{n} \\ j\sin(k_{\text{d}}t)\eta_{\text{d}}^{-1}\mathbf{n} & \cos(k_{\text{d}}t)\mathbf{I} \end{bmatrix} \begin{bmatrix} \cos(k_0 d)\mathbf{I} & -j\sin(k_0 d)\eta_0\mathbf{n} \\ j\sin(k_0 d)\eta_0^{-1}\mathbf{n} & \cos(k_0 d)\mathbf{I} \end{bmatrix} \\ & \begin{bmatrix} \mathbf{I} & \mathbf{0} \\ \mathbf{nY'_{s2}} & \mathbf{I} \end{bmatrix} \begin{bmatrix} \cos(k_{\text{d}}t)\mathbf{I} & -j\sin(k_{\text{d}}t)\eta_{\text{d}}\mathbf{n} \\ j\sin(k_{\text{d}}t)\eta_{\text{d}}^{-1}\mathbf{n} & \cos(k_{\text{d}}t)\mathbf{I} \end{bmatrix} \begin{bmatrix} \cos(k_0 d)\mathbf{I} & -j\sin(k_0 d)\eta_0\mathbf{n} \\ j\sin(k_0 d)\eta_0^{-1}\mathbf{n} & \cos(k_0 d)\mathbf{I} \end{bmatrix} \\ & \begin{bmatrix} \mathbf{I} & \mathbf{0} \\ \mathbf{nY'_{s3}} & \mathbf{I} \end{bmatrix} \begin{bmatrix} \cos(k_{\text{d}}t)\mathbf{I} & -j\sin(k_{\text{d}}t)\eta_{\text{d}}\mathbf{n} \\ j\sin(k_{\text{d}}t)\eta_{\text{d}}^{-1}\mathbf{n} & \cos(k_{\text{d}}t)\mathbf{I} \end{bmatrix}, \end{aligned} \tag{7.4}$$

where $\mathbf{I}$ = [1 0;0 1] denotes the identity matrix and $\mathbf{n}$ = [0 −1;1 0] represents the 90° rotation matrix. The wavenumber and wave impedance of the dielectric substrate

are denoted by k_{d} and η_{d}, respectively. The free-space wavenumber is denoted as k_0, while its wave impedance is represented as η_0. The three dielectric substrates share an identical thickness of t, while the two air gaps employ the same spacing of d. In order to minimise the material loss, ultra-low loss cyclic olefin copolymer (COC) is utilised as dielectric substrates, which presents a relative permittivity of $\epsilon_{\mathrm{r}} = 2.33$ and loss tangent of $\tan\delta = 0.0005$ over the frequency band of interest from 220 GHz to 330 GHz (Nielsen *et al.*, 2009).

Once the **ABCD** transfer matrix is built, the cumulative performance of the whole transmitarray in response to a linearly polarised wave under normal incidence can be readily calculated by using Equation (4.3), which is reproduced here as

$$\begin{bmatrix} \mathbf{S}_{11} & \mathbf{S}_{12} \\ \mathbf{S}_{21} & \mathbf{S}_{22} \end{bmatrix} = \begin{bmatrix} -\mathbf{I} & \frac{\mathbf{Bn}}{\eta_2} + \mathbf{A} \\ \frac{\mathbf{n}}{\eta_1} & \frac{\mathbf{Dn}}{\eta_2} + \mathbf{C} \end{bmatrix}^{-1} \begin{bmatrix} \mathbf{I} & \frac{\mathbf{Bn}}{\eta_2} - \mathbf{A} \\ \frac{\mathbf{n}}{\eta_1} & \frac{\mathbf{Dn}}{\eta_2} - \mathbf{C} \end{bmatrix}. \tag{7.5}$$

Here, $\mathbf{S}_{21}$ comprises transmission elements of different linear polarisations, namely

$$\mathbf{S}_{21} = \begin{bmatrix} T_{xx} & T_{xy} \\ T_{yx} & T_{yy} \end{bmatrix}. \tag{7.6}$$

Then, the S-parameters of the transmitarray under circularly polarised incident waves can be transformed from linear basis to circular basis using (Stephen *et al.*, 2018)

$$\begin{aligned} \mathbf{T}_{\mathrm{CP}} &= \begin{bmatrix} T_{\mathrm{RR}} & T_{\mathrm{RL}} \\ T_{\mathrm{LR}} & T_{\mathrm{LL}} \end{bmatrix} \\ &= \frac{1}{2} \begin{bmatrix} T_{xx} + T_{yy} + i(T_{xy} - T_{yx}) & T_{xx} - T_{yy} - i(T_{xy} + T_{yx}) \\ T_{xx} - T_{yy} + i(T_{xy} + T_{yx}) & T_{xx} + T_{yy} - i(T_{xy} - T_{yx}) \end{bmatrix}, \end{aligned} \tag{7.7}$$

where R and L denote right-handed (RHCP) and left-handed (LHCP) circular polarisations, respectively.

As an objective, the transmitarray-based circular polariser is designed to transmit the RHCP waves but reject the LHCP waves with an extinction ratio higher than 15 dB over a wide bandwidth. Here, the extinction ratio is defined as

$$\mathrm{ER\ (dB)} = 10\log_{10}\left(\frac{|T_{\mathrm{RR}}|^2}{|T_{\mathrm{RL}}|^2 + |T_{\mathrm{LR}}|^2 + |T_{\mathrm{LL}}|^2}\right). \tag{7.8}$$

It is noted that when using this expression, the polarisation conversion from LHCP to RHCP is anticipated to be suppressed, so that the circular polariser can be potentially

applied in wireless communications where cross-talk is undesired. Additionally, the circular polariser is expected to maintain a transmission magnitude above -1 dB over the entire frequency band of operation. As further design constraints, the achievable equivalent inductance and capacitance ranges of diverse patterns are explored by 3D full-wave simulations within a unit cell of fixed size. The responses of these patterns to the x- or y-polarised waves can be described by different circuit models. Furthermore, in order to account for the fabrication feasibility, the dielectric substrate thickness is specified in a range from 20 μm to 200 μm, while an identical spacing for the two air gaps that ranges from 100 μm to 500 μm is adopted. Based on the objectives and constraints mentioned above, the broadband semi-analytical approach is employed to determine the optimal frequency-independent circuit parameters for the circular polariser. Calculations reveal that a pattern providing purely inductive and capacitive responses for the two orthogonal polarisations accompanied with a pattern rotation around the z-axis is preferred for each metallic layer to realise the desired performance. The calculated optimal circuit parameters are detailed in Table 7.1, and the thicknesses of the three dielectric substrates are suggested to be $t = 20$ μm.

Following the procedure introduced in Chapter 4, a physical realisation of each metallic layer is conducted separately. Electromagnetic simulations are conducted with the commercial software ANSYS HFSS. To minimise the metal loss, gold is employed for each metallic layer, and its surface impedance at terahertz frequencies is described by a Drude model (Lucyszyn, 2007). A subwavelength unit cell size of $a = 400$ μm, corresponding to $0.44\lambda_0$ at 330 GHz, is chosen to avoid diffraction. The physically realised unit cell geometry of the circular polariser is shown in Figure 7.2, and its detailed physical dimensions are presented in Table 7.2. The top and bottom metallic

Table 7.1. Calculated optimal circuit parameters provided by the broadband semi-analytical approach for the circular polariser. L_{xi} and C_{yi} are the optimal equivalent inductance and capacitance of the i^{th} metallic layer along the x- and y-polarisations, respectively, and the pattern is anti-clockwise rotated by an angle of φ_i around the z-axis. The units for inductances and capacitances are pH and fF, respectively.

Top layer			Middle layer			Bottom layer		
L_{x1}	C_{y1}	φ_1	L_{x2}	C_{y2}	φ_2	L_{x3}	C_{y3}	φ_3
255	1.65	0°	0.34	0.71	45°	255	1.65	90°

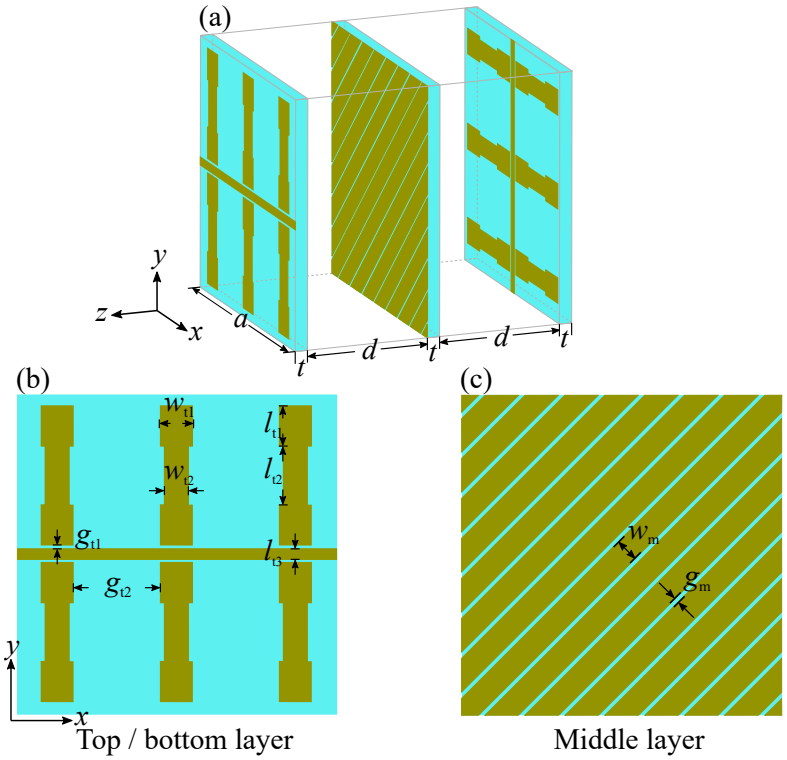

Figure 7.2. Unit cell geometry of the proposed circular polariser. (a) 3D view, (b) top or bottom metallic layer, and (c) middle metallic layer. The top and bottom layers share an identical pattern, but the bottom layer is rotated by 90° around the z-axis with respect to the top layer. Air gaps with a mechanically adjustable spacing of d are introduced in between the metallic layers to realise frequency tunability.

Table 7.2. Physical dimensions of the proposed circular polariser. The units are in µm.

Parameter	Value	Parameter	Value	Parameter	Value
a	400	g_{t2}	110	w_{t1}	40
t	20	l_{t1}	50	w_{t2}	30
d	210	l_{t2}	75	w_m	30
g_{t1}	5	l_{t3}	13	g_m	5

layers share an identical pattern, but the bottom layer is rotated by 90° around the z-axis with respect to the top layer. For the top metallic layer, a thin metallic strip oriented along the x-axis is employed to achieve a relatively high equivalent inductance, while the I-shaped patches are in series to minimise the equivalent capacitance, so that a predominately inductive response can be obtained along the x-polarisation. On the other hand, the I-shaped patches are in parallel along the y-axis to form a relatively high equivalent capacitance but a very limited inductance, so as to provide a predominately

capacitive response for the y-polarisation. A similar methodology is adopted for the middle layer to achieve the desired reactances for the two orthogonal polarisations. The middle layer is subsequently rotated by an angle of $\varphi_2 = 45°$ around the z-axis to yield the magneto-electric coupling, so that a bianisotropic response can be introduced.

7.3 Simulation results

Figure 7.3 shows the transmission magnitude and extinction ratio provided by the broadband semi-analytical approach and the 3D full-wave simulation. An excellent agreement between the calculated and simulated results is achieved. The slight deviation between them can be attributed to the difference between the equivalent reactances of the physically realised structure and the calculated optimal circuit parameters. It can be inferred from Figure 7.3(a) that the proposed circular polariser only allows RHCP incident waves to be transmitted, while LCHP transmission is largely suppressed. Importantly, circular polarisation conversion from one handedness to its orthogonal counterpart is well reduced at ~275 GHz, making the proposed structure applicable for wireless communications, in which a low cross-talk is desired. In Figure 7.3(b), a simulated extinction ratio higher than 15 dB can be maintained from 251 GHz to 298 GHz, leading

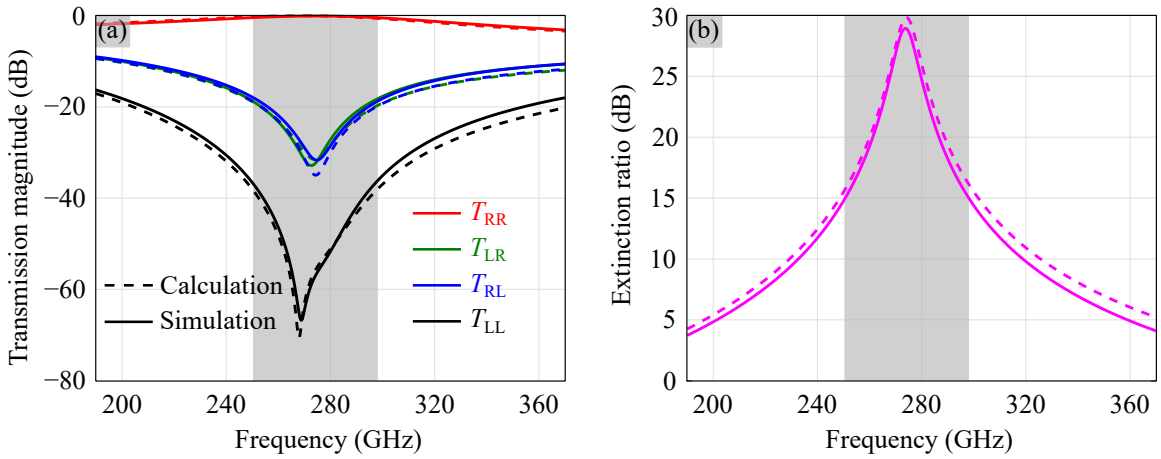

Figure 7.3. Calculated and simulated performance of the proposed circular polariser that selectively transmits RHCP waves. (a) Transmission magnitude and (b) extinction ratio. The calculated results are provided by the broadband semi-analytical approach, while the simulated results are obtained from the 3D full-wave simulation. The extinction ratio is defined as the transmittance ratio $|T_{RR}|^2 / \left(|T_{RL}|^2 + |T_{LR}|^2 + |T_{LL}|^2\right)$, where R and L denote right-handed and left-handed circular polarisations, respectively. The shaded area marks the simulated 15-dB extinction ratio bandwidth from 251 GHz to 298 GHz.

to a fractional bandwidth of 17.1% that is nearly twice that of the best circular polariser design (Pfeiffer and Grbic, 2014). Moreover, a RHCP transmission magnitude above -0.45 dB can be sustained over the entire 15-dB extinction ratio operation bandwidth.

The operation mechanism of the proposed circular polariser involves multiple reflections, but for understanding, can be simplified to a sequential circular-to-linear and linear-to-circular polarisation transformations. In general, the tri-layer structure can be considered as a combination of two quarter-wave plates and one linear polariser. It is assumed that incident waves propagate along the $-z$-axis. Further simulations reveal that the top and middle metallic layers collectively form a quarter-wave plate, which realises circular-to-linear polarisation conversion. Thus, RHCP incident waves can be effectively transformed into linearly polarised waves after passing through the top and middle layers, and their electric fields are oriented in a direction perpendicular to the middle layer metallic strips as shown in Figure 7.4(a). Consequently, the middle layer transmits this linearly polarised waves with low attenuation. In contrast, LHCP

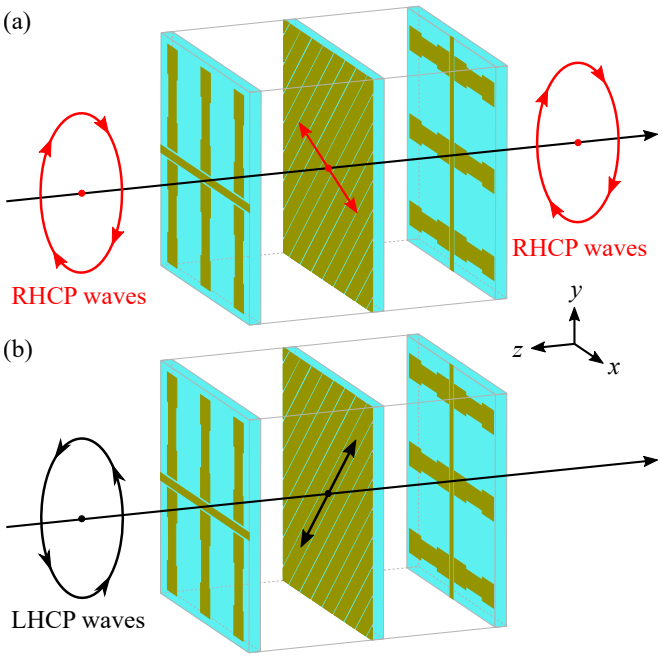

Figure 7.4. Operation principle of the circular polariser. (a) RHCP waves. The top and middle metallic layers collectively transform RHCP incident waves into linearly polarised waves, whose electric field is oriented in a direction perpendicular to the metallic strips in the middle layer. Subsequently, the middle and bottom layers jointly convert linearly polarised waves back to RHCP transmitted waves. (b) LHCP waves. The top and middle metallic layers transform LHCP incident waves into linearly polarised waves, with their electric field aligned with the middle layer metallic strips, and they are all reflected. Incident waves propagate along the $-z$-axis.

incident waves are converted to linearly polarised waves with electric fields aligned in a direction parallel to the middle layer metallic strips, and as a consequence they are completely reflected as illustrated in Figure 7.4(b). Similarly, simulations suggest that the middle and bottom layers in combination function as a second quarter-wave plate, which realises linear-to-circular polarisation conversion. Linearly polarised waves converted from RHCP incident waves can be decomposed into two orthogonal electric field components along the x- and y-axes, respectively. Moreover, a phase difference of around $-90°$ between the x- and y-directed field components can be obtained after passing through the second quarter-wave plate. As a result, linearly polarised waves converted from RHCP incident waves are eventually transformed into RHCP transmitted waves. Importantly, the proposed structure relies on multiple reflections in between the metallic layers, making its operation fundamentally different from the devices that merely cascade Jones matrices (Pfeiffer and Grbic, 2014).

In addition to the aforementioned operation frequency range from 251 GHz to 298 GHz, the proposed circular polariser is also capable of operating at nearby frequency bands by mechanically adjusting the air gap spacings. Figure 7.5(a) illustrates tunability of the circular polariser, where a 15-dB extinction ratio is maintained over a wide bandwidth. Figure 7.5(b) shows the the frequency of peak extinction ratio as a function of the air gap spacing, and their non-linear relationship results from the interference of multiple reflections between the metallic layers.

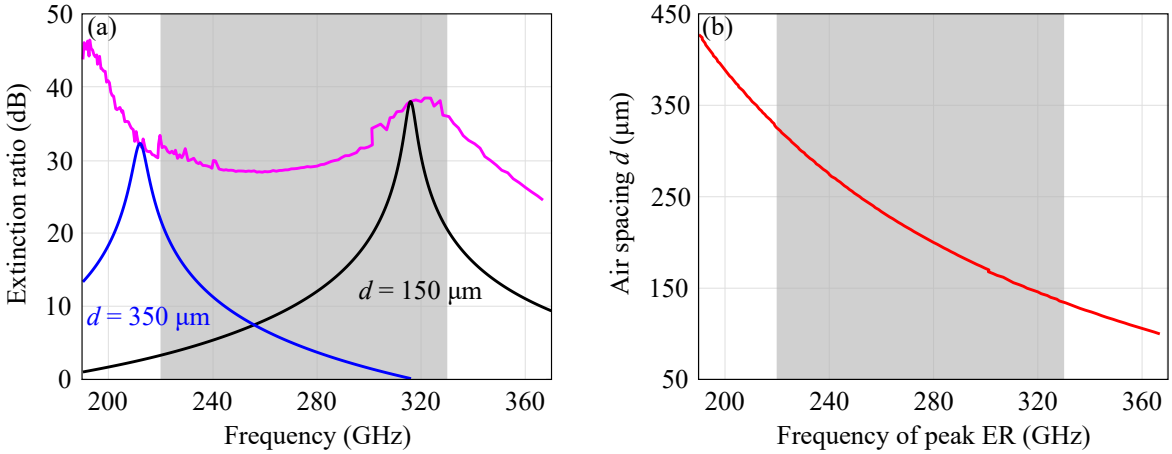

Figure 7.5. Simulated frequency tunability of the circular polariser by adjusting the air gap spacings. (a) Extinction ratios at different air gap spacings and (b) frequency of the peak extinction ratio versus air gap spacing d. The magenta curve in (a) depicts the peak extinction ratio of the circular polariser with air gaps of various spacings. The shaded area marks the frequency range of interest from 220 GHz to 330 GHz, defined for the WR-3.4 waveguide band.

7.4 Extensions

The operation principle of the circular polariser suggests that the proposed structure can be reconfigured to selectively transmit LHCP incident waves by simply rotating the middle metallic layer by 90° around the z-axis. This can be explained by the linear polarisation filtering of the middle layer. A 90° rotation of the middle layer makes the metallic strips perpendicular to the electric fields of linearly polarised waves converted from LHCP incident waves, but parallel to that transformed from RHCP incident waves. Linearly polarised waves converted from LHCP incident waves are then transformed into LHCP transmitted waves after propagating through the second quarter-wave plate. Consequently, the proposed structure will correspondingly transmit LHCP incident waves with a simulated extinction ratio above 15 dB from 251 GHz to 298 GHz, while the transmission magnitude is above −0.45 dB over the entire 15-dB extinction ratio operation bandwidth as depicted in Figure 7.6.

Apart from working as circular polarisers, the proposed structure can also function as a quasi-half-wave plate to convert between circular polarisation with opposite handednesses. This can be configured by a 90° rotation of the top or bottom metallic layer. We choose the bottom metallic layer rotation as an example. A 90° rotation of the bottom

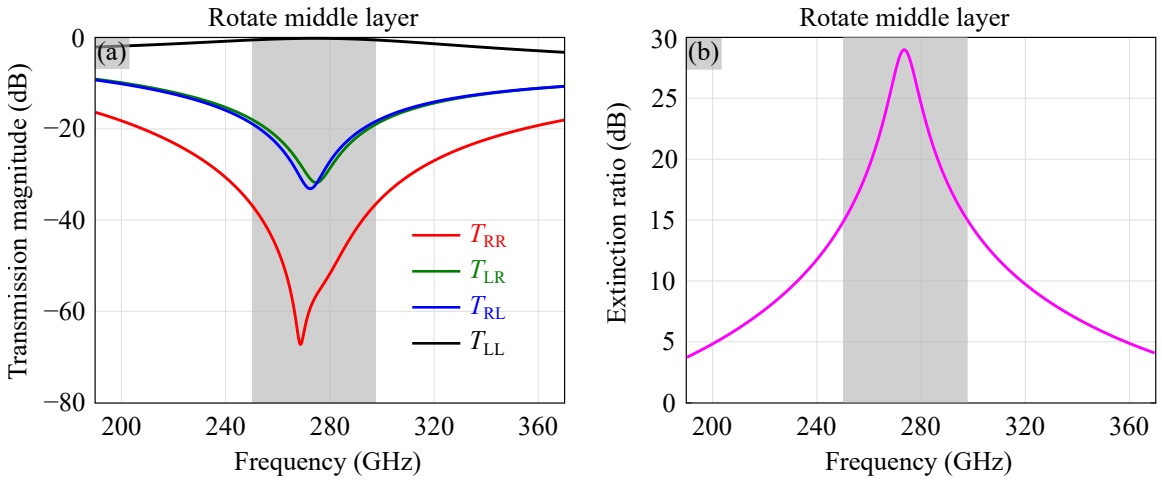

Figure 7.6. Simulation results of the proposed structure functioning as a circular polariser that allows LHCP waves transmission. (a) Transmission magnitude and (b) extinction ratio. The middle metallic layer is rotated by 90° around the z-axis. The extinction ratio here is defined as the transmittance ratio $|T_{LL}|^2 / \left(|T_{RL}|^2 + |T_{LR}|^2 + |T_{RR}|^2\right)$. The simulation curves in (a, b) are identical to the simulation ones shown in Figure 7.3, while the only difference is the polarisation exchange between RHCP and LHCP. The shaded area marks the 15-dB extinction ratio bandwidth from 251 GHz to 298 GHz.

layer results in a phase difference of around 90° between the x- and y-directed transmitted waves. Thus, linearly polarised waves converted from RHCP incident waves are then transformed into LHCP transmitted waves after propagating through the second quarter-wave plate constructed by the middle and bottom layers. The proposed structure with a 90° rotation of the top metallic layer works in a similar manner, but it transforms LHCP incident waves into RHCP transmitted waves. Figure 7.7 depicts the simulated performance of the structure with a 90° rotation of the top or bottom layer. In both cases, an extinction ratio of 15 dB can be maintained from 251 GHz to 298 GHz for

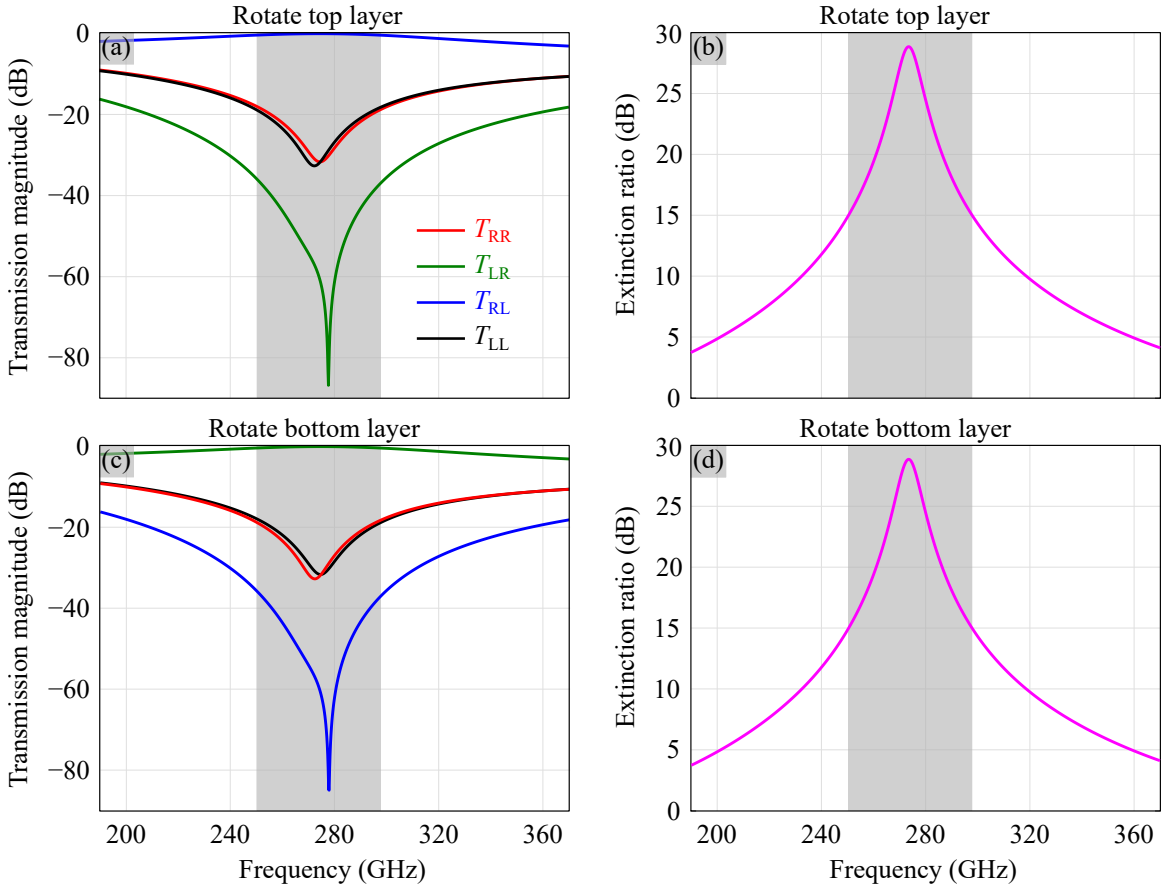

Figure 7.7. Simulation results of the proposed structure functioning as a transmissive quasi-half-wave plate by rotating the top or bottom metallic layer. (a) Transmission magnitude and (b) extinction ratio of the structure with the top metallic layer rotated by 90° around the z-axis. (c) Transmission magnitude and (d) extinction ratio of the structure with the bottom metallic layer rotated by 90° around the z-axis. The extinction ratio in (b) is defined as the transmittance ratio $|T_{RL}|^2 / \left(|T_{RR}|^2 + |T_{LR}|^2 + |T_{LL}|^2\right)$, while that in (d) is defined as $|T_{LR}|^2 / \left(|T_{RR}|^2 + |T_{RL}|^2 + |T_{LL}|^2\right)$. The simulation curves in (a, b) are identical to the ones in (c, d), while the only difference is the polarisation exchange between RHCP and LHCP. The shaded area marks the 15-dB extinction ratio bandwidth from 251 GHz to 298 GHz.

Table 7.3. Functionalities of the proposed structure by rotating a single metallic layer. All functionalities listed here share the same simulated 15-dB extinction ratio fractional bandwidth of 17.1%, namely from 251 GHz to 298 GHz, while the extinction ratio definitions are varied in different scenarios. Quasi-half-wave plate denotes that the device can invert circular polarisation from one handedness to the other, but cannot rotate linear polarisation by 90°.

Device	Metallic layer rotation (90°)	Functionality
Circular polariser	–	RHCP waves transmission only
Circular polariser	Middle	LHCP waves transmission only
Quasi-half-wave plate	Top	LHCP-to-RHCP transformation
Quasi-half-wave plate	Bottom	RHCP-to-LHCP transformation

both tailored reconfigurations, and their transmission magnitudes are above -0.45 dB over the entire operation frequency bands. It should be noted that the definition of extinction ratio needs to be re-defined accordingly for the structure working in different scenarios.

The achievable functionalities of the structure by a 90° rotation of the metallic layer around the z-axis is concluded in Table 7.3. Importantly, the operation bandwidths of the device working in different states can be readily tuned to nearby frequency bands, provided that the air gap spacings are mechanically adjustable.

7.5 Conclusion

This Chapter presents a transmitarray-based circular polariser exhibiting a simulated 15-dB extinction ratio fractional bandwidth of 17.1% from 251 GHz to 298 GHz. The circular polariser can filter circular polarisation of the preferred handedness with a transmission magnitude higher than -0.45 dB over the bandwidth of operation. Moreover, the proposed structure can also function as a quasi-half-wave plate by simply rotating a single metallic layer by 90° around the z-axis, and it holds the potential of mechanical tunability to operate at nearby frequency bands. Relying on the interference of multiple reflections in between the metallic layers, the proposed structure achieves bianisotropic responses but retains a planar and subwavelength profile. The operation bandwidth and versatility of the structure are competitive to the reported designs, and spectroscopic detection of chiral molecules in biology and polarisation-division multiplexing in communications can benefit from the proposed structure.

Chapter 8

Ultra-wideband far-infrared absorber

FAR-INFRARED absorbers exhibiting wideband performance are in great demand in numerous applications, including imaging, detection, and wireless communications. Here, a non-resonant far-infrared absorber with an ultra-wideband operation is proposed. This absorber is in the form of inverted pyramidal cavities etched into moderately doped silicon. By means of a wet-etching technique, the crystallinity of silicon restricts the formation of the cavities to a particular shape, in an angle that favors impedance matching between lossy silicon and free space. Far-infrared waves incident on this absorber experience multiple reflections on the slanted lossy silicon side walls, and are dissipated on the path towards the cavity bottom. The simulation and measurement results confirm that an absorption beyond 90% can be sustained from 1.25 to 5.00 THz. Furthermore, the experiment results suggest that the absorber can operate up to at least 21.00 THz with a specular reflection less than 10% and negligible transmission.

8.1 Introduction

Electromagnetic absorbers are essential components for various applications and have been widely studied in the far-infrared regime. Early research activities on far-infrared absorbers involved bottom-up chemical synthesis approaches. Prominently, gold black films made by amorphous deposition are known to exhibit excellent Ohmic absorption from the visible and near-infrared ranges down to 6 THz. These gold black films with a low thermal mass have been used for coating pyroelectric detectors to improve their sensitivity (Nelms and Dowson, 2005). Lately, carbon nanotubes from chemical synthesis have led to the implementation of absorbers with superior absorption, thermal conductivity, and damage threshold (Lehman *et al.*, 2005).

Over the past decades, the development of powerful computational electromagnetic solvers and advanced micro-fabrication techniques have facilitated the design and physical realisation of diverse microstructures for far-infrared absorption. As opposed to the bottom-up approach that exploits existing properties of synthesized materials, a top-down design and fabrication approach promises designability, robustness, and reproducibility of electromagnetic absorbers. A number of reports toward this direction have involved metamaterial-based perfect absorbers (Landy *et al.*, 2008; Tao *et al.*, 2008). Typically, these absorbers are composed of periodic metallic resonators on a grounded dielectric substrate. A near-unity absorption can be achieved through impedance matching near the resonance frequencies. An alternative approach involves lossy grating structures for diffraction and absorption (Shi *et al.*, 2014; Zang *et al.*, 2015; Peng *et al.*, 2015; Shi *et al.*, 2016).

Inspite of their scalability, most resonance-based absorbers have a limited fractional bandwidth of around 10–30% as a result of their resonant nature (Liu *et al.*, 2018). Alternatively, non-resonant structures have recently shown their excellent absorption performance in various frequency bands (Kim *et al.*, 2012; Liu *et al.*, 2018). In these non-resonant designs, the reflection was eliminated by gradient impedance matching, and the dissipation was derived from either lossy conductors or lossy dielectrics. In the visible and near-infrared ranges, tapered nano-grooves made of metals were shown to exhibit absorption by coupling incident light with gap surface plasmon polaritons (Beermann *et al.*, 2013, 2014). At terahertz frequencies, surface-relief structures made of PDMS in the form of micro-pyramids exhibited absorption from 0.75 THz to 2.00 THz (Kim *et al.*, 2012).

In this Chapter, we propose a non-resonant far-infrared absorber made of moderately doped silicon. The wet-etching process intrinsically forms inverted pyramidal air cavities into the silicon to provide a natural impedance transition and gradual absorption of incident waves. A fine control of the losses is attained by employing doped silicon. In contrast to the resonance-based silicon absorbers (Withayachumnankul *et al.*, 2013, 2014; Cheng *et al.*, 2015; Zhai *et al.*, 2017), the proposed structure shows a significantly broadened absorption bandwidth, while the fabrication complexity is greatly reduced.

8.2 Design

Figure 8.1 illustrates the unit cell geometry of the proposed far-infrared absorber. Microcavities taking the form of inverted pyramids are etched anisotropically into a moderately doped silicon. A wet-etching technique is employed to form naturally self-terminated pyramidal cavities. Due to the fact that a standard silicon surface terminates at (001) planes, while potassium hydroxide (KOH) selectively etches (001) planes instead of (111) crystal planes, the wet-etching process thus establishes the side walls with a fixed angle of $\theta = 54.7°$ (Zhang *et al.*, 2005). The cavity height h is determined by its aperture width b according to $h = (b \cdot \tan\theta)/2$. A minimum ridge width of 4 µm at the unit cell borders is set by fabrication constraints. Ideally, a zero-width ridge would be preferred since the flat silicon surface contributes to reflections especially at higher frequencies. Collectively, the absorber is formed by identical inverted pyramidal cavities periodically arranged as a planar array.

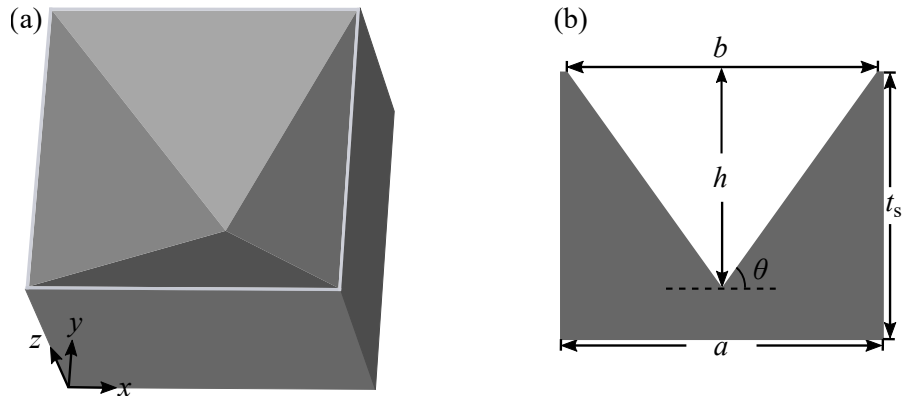

Figure 8.1. Unit cell geometry. (a) 3D view and (b) cross-sectional view. The detailed dimensions are given as follows: $a = 200$ µm, $b = 196$ µm, $t_s = 170$ µm, $h = 139$ µm, and $\theta = 54.7°$.

The employed silicon is ⟨100⟩ oriented and doped with phosphorus (n-type). The DC resistivity of the silicon lies in between 0.05–0.10 Ω·cm, while its carrier concentration is estimated as $\sim 2.3\times10^{17}$ cm^{-3} and its electron mobility equals 547 cm^2/(V·s) at room temperature. The corresponding plasma frequency is 8.44 THz and the collision frequency equals 1.97 THz.

Electromagnetic simulations are carried out with the commercial software ANSYS HFSS. In the HFSS simulations, a single unit cell is bounded by master-slave boundary conditions in the transverse plane to mimic an infinite planar array, and silicon properties are described by the Drude model (Hashimshony *et al.*, 2001). Floquet ports accounting for higher-order propagating modes are implemented to impose incident waves and also to collect the scattered waves. Given the available computational power and solution time required, the silicon thickness is chosen as t_s = 170 μm in the simulations so that the transmission of incident waves can be effectively suppressed. The upper simulation frequency is limited to 5.00 THz, set by the required computational power to account for the increased number of higher-order propagating modes at higher frequencies (see Appendix C).

Figure 8.2 shows the calculated and simulated absorption spectra of bare silicon slabs and etched slabs with different carrier concentrations adopted from Zhai *et al.* (2017) and Du *et al.* (2016). Here, the normalised absorption A is defined as $A = 1 - R - T$, where R and T denote the total reflected and transmitted power, respectively, each

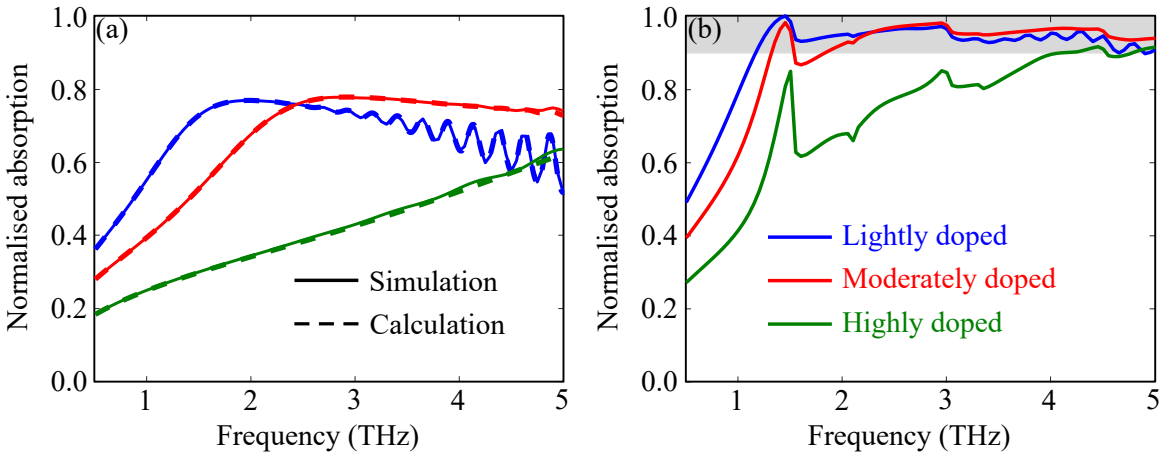

Figure 8.2. Absorption spectra of silicon materials with different carrier concentrations. (a) Calculated and simulated results of bare silicon slabs. (b) Simulated absorption spectra of absorbers. The shaded area in (b) marks the absorption beyond 90%. The carrier concentrations of lightly, moderately, and highly doped silicon are 8.8×10^{16}, 2.3×10^{17}, and 1.58×10^{18} cm^{-3}, respectively.

contributed by the fundamental modes and higher-order propagating modes. It can be inferred from Figure 8.2(a) and (b) that the proposed absorber shows a significant improvement in terms of absorption compared with the bare silicon, demonstrating the absorbing functionality of the proposed structure. From the bare silicon slabs in Figure 8.2(a), simulation results show close agreement with the results calculated based on Fresnel equations. It is worth noting that the lightly doped bare silicon shows non-negligible transmittance beyond 2.50 THz, and its low attenuation leads to multiple reflections inside of the bare silicon slab, resulting in Fabry-Pérot fringes at higher frequencies. Figure 8.2(b) depicts the absorption performance of the absorbers with different doping concentrations. It is clear that moderately doped silicon provides advantageous absorption, as the lightly doped silicon shows a decreasing absorption at higher frequencies resulting from its reduced dielectric loss, while the highly doped silicon exhibits an absorption below 90% at lower frequencies. It should be noted that the conductor-to-dielectric transitions of lightly, moderately, and highly doped silicon take place at 0.76 THz, 1.49 THz, and 3.68 THz, respectively, where the real part of the relative permittivity changes from negative to positive values. Dielectrics typically exhibit weaker reflections compared to conductors, and thus, a conductor-to-dielectric transition at a lower frequency leads to a superior absorption of lightly doped silicon in the lower frequency range. Increasing the doping level leads to a blue shift of the 90% absorption frequency range. Figure 8.3 shows the electric field magnitude distributions of absorbers with different doping levels at 1.50 THz and the highest simulation frequency of 5.00 THz. It reveals that higher-frequency components can penetrate deeper into the silicon, resulting from the reduced dielectric loss at higher frequencies.

Since the unit cell size of 200 μm corresponds to the free-space wavelength at 1.50 THz, the absorber basically operates above the subwavelength regime. Hence the effective medium theory is not applicable in explaining the absorption mechanism. For this particular design, the perfect absorption can be better explained in terms of wave propagation down the inverted pyramidal cavities, with slightly different interpretations at low and high frequencies. At low frequencies, the pyramidal cavities provide a smooth impedance matching to the lossy material, thus leading to absorption rather than reflection. In a ray-optics approximation at high frequencies, the angle of $\theta = 54.7^\circ$ of the side walls constituting the cavity does not allow back reflection to the source but rather causes reflection downwards the cavity. As illustrated in Figure 8.3, incident waves

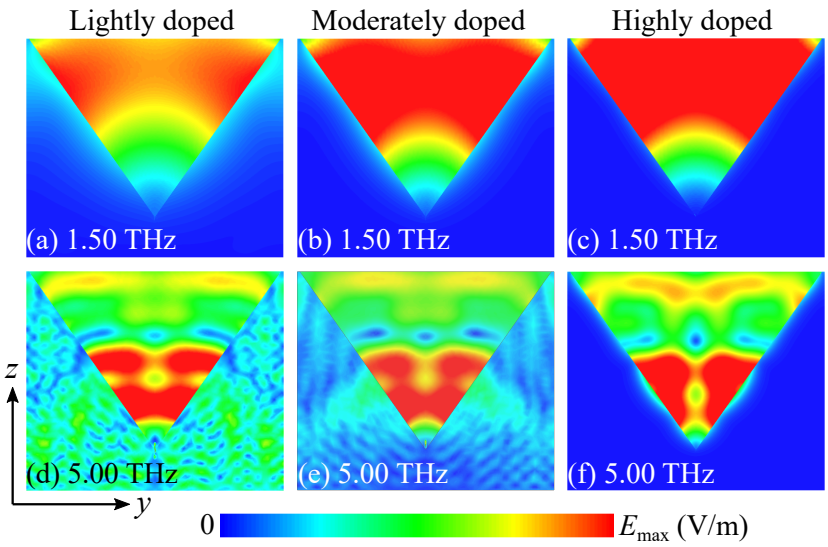

Figure 8.3. Simulated electric field magnitude distributions of absorbers made of silicon with different doping concentrations. The field distributions share the same linear scale.

experience multiple reflections along the path, and most of the energy is dissipated into the doped silicon resulting from dielectric loss.

8.3 Fabrication

The inverted pyramidal cavities are fabricated on a moderately doped silicon wafer of 250 µm thickness and 2-inch diameter. Images of the fabricated prototype are given in Figure 8.4. The sample was manufactured by the Functional Materials and Microsystems Research Group and the Micro Nano Research Facility at RMIT University. The silicon wafer is deposited with silicon nitride of around 500 nm thick on both sides

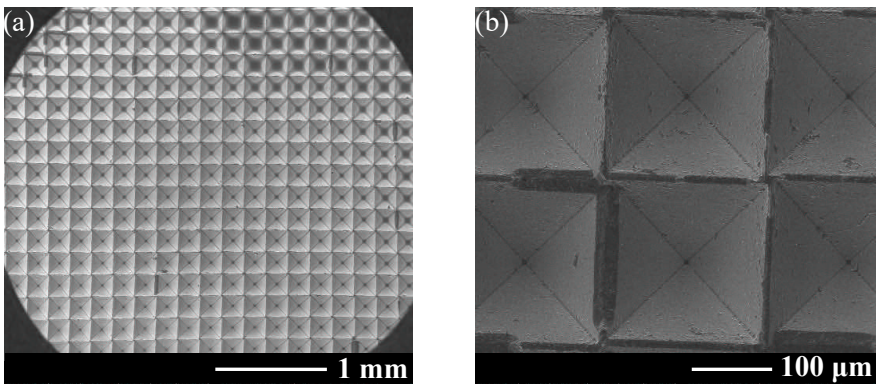

Figure 8.4. Scanning electron micrographs of the fabricated absorber. (a) Partial view and (b) magnified view containing 6 unit cells.

using low pressure chemical vapour deposition (LPCVD). This silicon nitride layer functions as a mask for the processing steps of etching with KOH, as silicon nitride does not react to KOH. Firstly, one surface of the nitride-coated wafer is patterned using photolithography and developed with a suitable developer. Thereafter, the wafer undergoes inductively coupled plasma-reactive ion etching (ICP-RIE) to etch silicon nitride in the openings created by the photolithography. In this process, the nitride layer is etched by using chemically reactive plasma under low pressure conditions, potentially combined with ion-induced etching. The deposited photoresist is then completely removed with acetone and isopropanol before KOH etching. The wafer is immersed in a bath of KOH, the solution is maintained constantly at 70°C; the concentration of the KOH solution used is 45%. It takes approximately 11 hours to etch these features completely. This process develops inverted pyramidal cavities at the specified angle across the surface. Finally, the nitride layers from the top and bottom surfaces are removed by RIE.

8.4 Measurement

The absorption performance of the proposed far-infrared absorber is characterised by jointly employing terahertz time-domain spectroscopy (THz-TDS) and Fourier-transform infrared spectroscopy (FTIR). Limited by its dynamic range, THz-TDS is used to interrogate the absorber in the frequency range of 0.50 THz to 1.50 THz, while FTIR is employed to characterise the structure from 1.50 THz to 21.00 THz. Figure 8.5 illustrates the experimental setup using THz-TDS in reflection mode. A linearly polarised incident

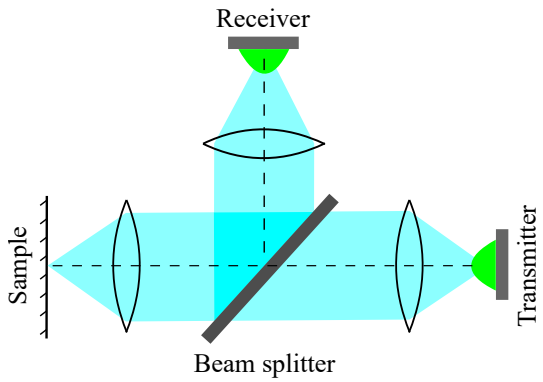

Figure 8.5. Schematic of the reflection measurement setup at normal incidence using THz-TDS. The measurement frequency range is from 0.50 THz to 1.50 THz, set by the dynamic range of THz-TDS.

wave propagates through a beam splitter, and is then focused onto the sample at normal incidence. A fraction of the energy is reflected toward the beam splitter to be collected by the receiver. In the reference measurement, the sample is replaced by a gold-coated mirror. Further experiments using the THz-TDS in transmission mode confirm the negligible wave transmission through the sample. For the absorption spectrum from 1.50 THz to 21.00 THz, a FTIR is employed to measure the reflection and transmission amplitudes of the sample.

8.5 Results

Owing to the four-fold symmetry of the unit cell, the absorber response is polarisation-independent under normal incidence. Figure 8.6 depicts the absorption spectra of the proposed absorber at normal incidence. It can be inferred from simulations that the diffraction from higher-order modes occurs from 1.50 THz, where non-negligible amount of power starts to be diffracted, resulting in a resonance-like dip at around 1.50 THz. The simulation results accounting for diffraction show close agreement with the measured results from 0.50 THz to 5.00 THz. Thus, an absorption beyond 90% is confirmed from 1.25 THz to 5.00 THz. Moreover, a measured specular reflection below 10% and negligible transmission can be maintained up to at least 21.00 THz. It is worth noting that the diffracted power cannot be fully measured due to the limitations of the

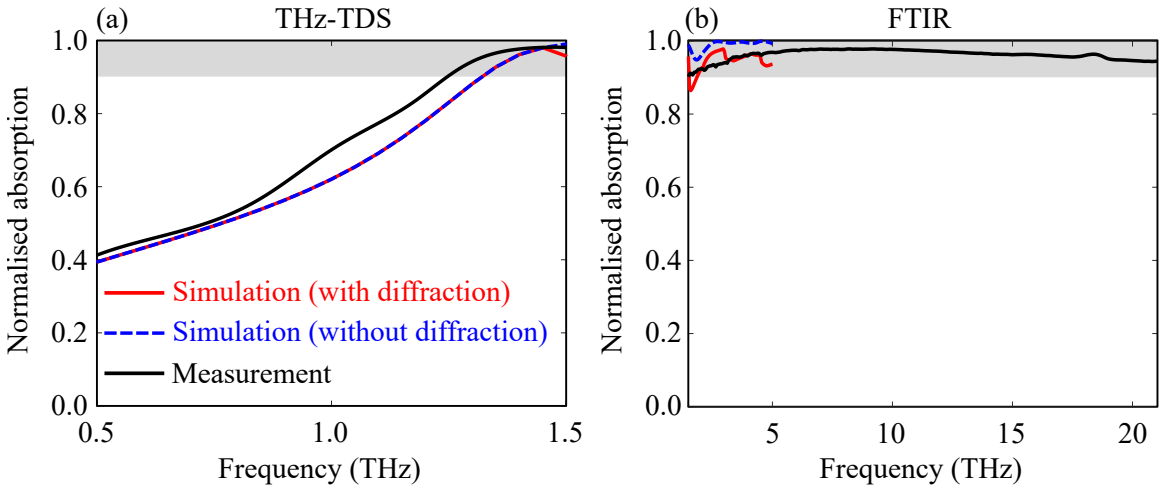

Figure 8.6. Normalised absorption spectra of the proposed absorber under normal incidence. The experiments are conducted by using (a) THz-TDS and (b) FTIR. All reflection measurements are normalised against the reference experiments taken with a gold-coated mirror. The shaded area marks the absorption beyond 90%.

available facility. The measured results show a discontinuity at 1.50 THz with a difference value of 0.08. This difference can be attributed to the experimental misalignments and system sensitivity of the THz-TDS and FTIR. Theoretically, the lower limit of the 90% absorption frequency band is mainly set by the conductor-to-dielectric transition frequency of the doped silicon, while its upper limit is expected where the dielectric loss of slicon vanishes. Additionally, the quality of the tip and ridge of the cavities also collectively limit the upper 90% absorption frequency bound. Additional simulations of moderately doped silicon absorber reveal that the 90% absorption coverage can be further extended with a smaller unit cell.

Figure 8.7 shows the simulated absorption spectra of the proposed absorber in response to obliquely incident waves without and with accounting for diffraction effects, where

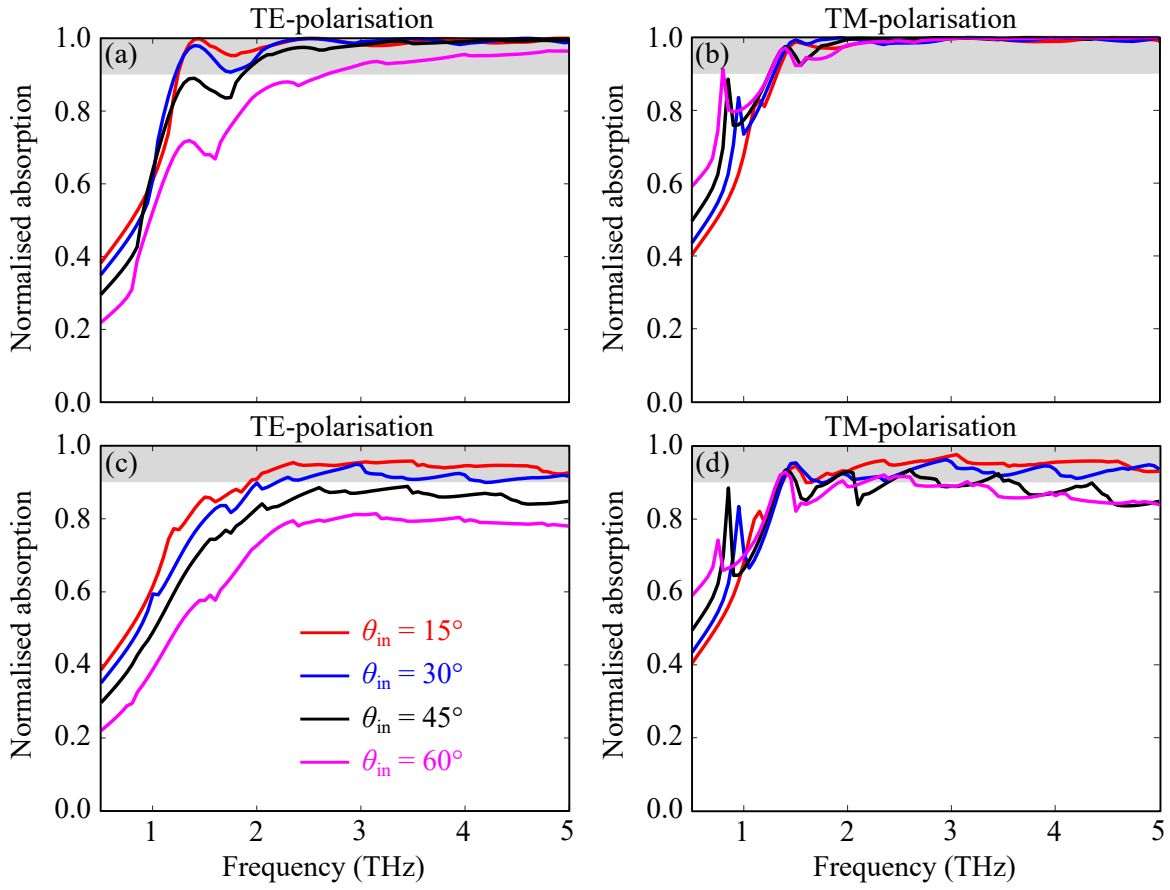

Figure 8.7. Simulated absorption spectra at different incidence angles for the TE-polarisation (left column) and TM-polarisation (right column). [(a, b)] and [(c, d)] correspond to the spectra without and with diffraction from higher-order propagating modes, respectively. The shaded area marks the absorption beyond 90%.

a non-negligible power from higher-order propagating modes can be inferred. Figure 8.7(c) illustrates that an absorption of 90% can be effectively maintained up to an incidence angle of 30° for the TE-polarised incident waves, while Figure 8.7(d) suggests that at a large incidence angle of 60°, a 90% absorption bandwidth still can be achieved in a limited range for the TM-polarisation. It is found that diffraction becomes stronger with larger incidence angles for the TE- and TM-polarisations, resulting in a degraded absorption performance.

8.6 Conclusion

In conclusion, we have proposed an ultra-wideband absorber that spans nearly the entire far-infrared spectrum. The structure can be fabricated into a moderately doped silicon that exhibits a lossy dielectric behaviour in the far-infrared. Since the pyramidal cavity is non-resonant, the structure exhibits an absorption of over 90% from 1.25 THz to 5.00 THz, accounting for diffraction. Additionally, a specular reflection below 10% and negligible transmission is observed experimentally up to 21.00 THz. The observation in the upper range is limited by the available computational power and characterisation facilities. This absorber is superior to existing far-infrared resonant absorbers in terms of the absorption spectrum coverage. Additionally, the fabrication can be achieved with standard photolithography and wet-etching techniques; it does not require multilayer processing or delicate control of compositions. The structure can be useful in far-infrared spectrometers and detectors to suppress stray far-infrared light and to increase detection sensitivity.

Chapter 9

Thesis summary

THIS Chapter concisely summarises the doctoral thesis. Chapters 1 and 2 provide the context for the doctoral program, which cover relevant research background, fundamental theories, and related demonstrations in the literature. Chapters 3 to 8 present the original contributions in relation to broadband terahertz metasurfaces for wavefront control and polarisation manipulation. Lastly, an outlook is presented in this Chapter.

9.1 Thesis conclusion

The main aim of the doctoral program was to develop and demonstrate techniques for realising terahertz metasurfaces with enhanced bandwidth. The developed methodologies have resulted in remarkable bandwidth improvement, much needed for terahertz applications. The realisations encompass metasurface-based functional devices for wavefront control and polarisation manipulation. This Section provides a brief summary on the original contributions of the thesis.

Reflectarray This part contains Chapter 3, and it presents a study on reflectarray bandwidth enhancement. A novel single-layer resonator is proposed, and a terahertz focusing reflectarray has been constructed and experimentally characterised to verify the functionality of the proposed resonator.

Transmitarrays This part comprises Chapters 4 to 7, and it discusses a semi-analytical approach that focuses on broadband performance. Subsequently, broadband transmitarrays for antireflection, polarisation conversions, and circular polarisation discrimination are systematically designed based on this approach.

Absorber This part includes Chapter 8, and it presents an ultra-wideband absorber. The non-resonant absorber is developed based on moderately doped silicon by means of a wet-etching technique, and the structure realises impedance matching between the lossy silicon and free-space over an ultra-wide bandwidth.

9.2 Outlook

The technical advancements introduced in this thesis are beneficial to the development of terahertz technology. As a complement to the thesis, this Section discusses further research challenges to expedite widespread adoption of the proposed methodology and functional devices into practical applications.

Dynamic scanning All the metasurface-based devices presented in this thesis employ passive resonators that cannot be actively reconfigured, leading to static functionality. Dynamically-reconfigurable devices are highly sought after for some applications. Therefore, resonators that are electronically tunable and can simultaneously maintain a high-efficiency and broadband performance are worth further investigation.

Methodology development The transmitarrays designed with an aid from the broadband semi-analytical approach provide designable birefringence or bianisotropy over

a wide bandwidth. However, metal loss and resonators' near-field coupling are both assumed to be negligible in the broadband approach, resulting in performance deviation from the 3D full-wave simulations. Moreover, the broadband approach cannot investigate the structure performance at oblique incidence. Thus, to enhance the capacities of this approach, further research efforts should be made to overcome its associated limitations.

Straightforward physical realisation Realising a physical structure from a circuit model is based on matching their reflection performance. However, the process is tedious and time-consuming as it starts from a pattern of arbitrary dimensions and informed adjustments until the results match the optimal ones. Additionally, the presence of parasitic capacitance or inductance contributes to performance discrepancy, where a purely inductive or capacitive response is desired. Thus, the development of a straightforward method to translate the optimal circuit parameters to physical structures is vitally important.

Appendix A

Axial ratio to extinction ratio transformation

In the microwave region, circular polarisation purity is commonly characterised by the axial ratio, while in the optics, the extinction ratio is typically adopted for the same purpose. In this Appendix, we show how the two ratios are related. Figure A.1 illustrates the polarisation ellipse of the electromagnetic wave that can be decomposed into left-handed circular polarisation (LHCP) and right-handed circular polarisation (RHCP). The major axis equals the vector summation of RHCP and LHCP electric field components, while the minor axis is the difference between them. Thus, the axial ratio of the electromagnetic wave can be expressed as

$$\mathrm{AR\ (dB)} = 20\log_{10}\left(\frac{|\mathbf{E}_\mathrm{L}| + |\mathbf{E}_\mathrm{R}|}{|\mathbf{E}_\mathrm{L}| - |\mathbf{E}_\mathrm{R}|}\right), \tag{A.1}$$

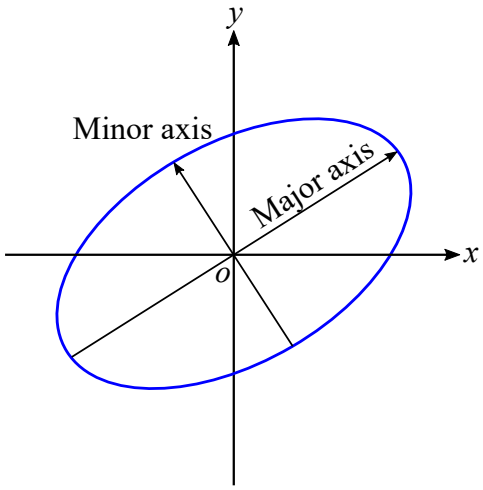

Figure A.1. Polarisation ellipse of the electromagnetic wave. The two principal axes are used for calculation of the axial ratio.

where $|\mathbf{E}_L|$ and $|\mathbf{E}_R|$ represent the electric field amplitudes of the LHCP and RHCP, respectively. On the other hand, the extinction ratio of LHCP to RHCP is defined as

$$\mathrm{ER\ (dB)} = 10 \log_{10} \left(\frac{|\mathbf{E}_L|^2}{|\mathbf{E}_R|^2} \right). \tag{A.2}$$

From Equations (A.1) and (A.2), the extinction ratio can be readily related to the axial ratio as

$$\mathrm{ER} = \left(\frac{\mathrm{AR} + 1}{\mathrm{AR} - 1} \right)^2, \tag{A.3}$$

where AR and ER above are in linear scale. Hence, it can be derived that a 3 dB axial ratio corresponds to $\sim$15 dB extinction ratio.

Appendix B

Gaussian beam profile

A collimated Gaussian beam is generated by the THz-TDS system, together with a plano convex lens with a focal length of 54 mm. The beam is utilised as an excitation for the reflectarray measurement in Chapter 3. Figure B.1 shows the measured raster-scanned beam profiles from 0.90 THz to 1.15 THz with a scan area of 40.5 × 40.5 mm^2. On that basis, an incident beam radius of ∼17 mm can be assumed.

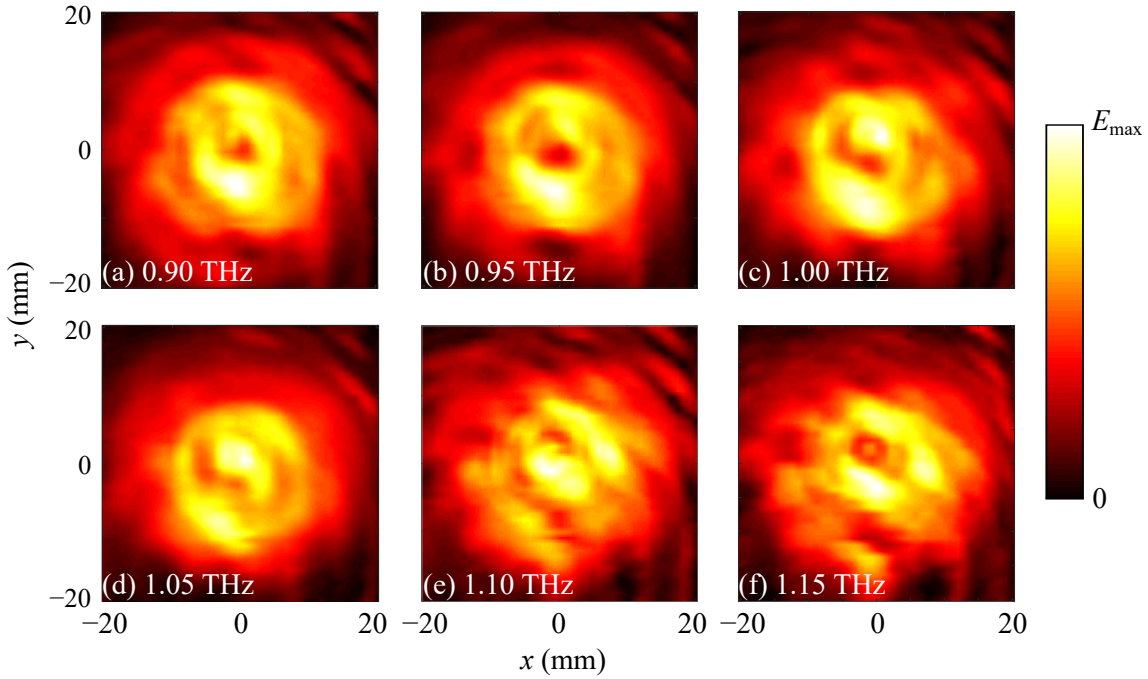

Figure B.1. Linear magnitude profiles of the measured Gaussian beam. The beam profiles at different frequencies are normalised to their respective maxima.

Appendix C

Cut-off frequencies of higher-order Floquet modes

In this Appendix, we discuss the cut-off frequency of a given Floquet mode. The cut-off frequency is defined as the starting frequency at which the mode becomes non-evanescent. It is assumed that an infinite periodic array consisting of unit cells of identical size is positioned in the xy-plane, with a lattice constant of p_x and p_x along the x- and y-axes, respectively. We consider a plane wave propagates along the $-z$-axis with an oblique incidence angle of (θ_i, φ_i), where θ_i is in the yz-plane and φ_i is in the xz-plane. Thus, its wavenumbers along the x- and y-axes can be expressed as (Petersson and Jin, 2006)

$$\begin{aligned} k_{xm} &= \frac{2\pi m}{p_x} - k_0 \sin\theta_i \cos\varphi_i \\ k_{yn} &= \frac{2\pi n}{p_y} - k_0 \sin\theta_i \sin\varphi_i, \end{aligned} \tag{C.1}$$

where k_0 denotes the free-space wavenumber, and (m, n) are the modal indices. The wavemumber of the incident plane wave in the z-direction can be written as

$$k_{z,mn} = \begin{cases} \sqrt{k_0^2 - k_{xm}^2 - k_{yn}^2}, & \text{if } k_{xm}^2 + k_{yn}^2 \leq k_0^2 \text{ (propagating waves)} \\ -j\sqrt{k_{xm}^2 + k_{yn}^2 - k_0^2}, & \text{if } k_{xm}^2 + k_{yn}^2 > k_0^2 \text{ (evanescent waves).} \end{cases} \tag{C.2}$$

At this stage, the cut-off frequency of a given mn mode can be readily calculated by setting $k_{z,mn} = 0$ and $k_0 = k_c = 2\pi f_c/c$. It is noted that the cut-off frequency of each higher-order mode is dependent on the plane wave incidence angle of (θ_i, φ_i).

Bibliography

ABDELRAHMAN-A. H., YANG-F., ELSHERBENI-A. Z., AND NAYERI-P. (2017). Analysis and design of transmitarray antennas, *Synthesis Lectures on Antennas*, **6**(1), pp. 1–175.

AHMADI-A., GHADARGHADR-S., AND MOSALLAEI-H. (2010). An optical reflectarray nanoantenna: the concept and design, *Optics Express*, **18**(1), pp. 123–133.

AKO-R. T., LEE-W. S. L., ATAKARAMIANS-S., BHASKARAN-M., SRIRAM-S., AND WITHAYACHUMNANKUL-W. (2020a). Ultra-wideband tri-layer transmissive linear polarization converter for terahertz waves, *APL Photonics*, **5**(4), art. no. 046101.

AKO-R. T., UPADHYAY-A., WITHAYACHUMNANKUL-W., BHASKARAN-M., AND SRIRAM-S. (2020b). Dielectrics for terahertz metasurfaces: material selection and fabrication techniques, *Advanced Optical Materials*, **8**(3), art. no. 1900750.

AL-NAIB-I., AND WITHAYACHUMNANKUL-W. (2017). Recent progress in terahertz metasurfaces, *Journal of Infrared, Millimeter, and Terahertz Waves*, **38**(9), pp. 1067–1084.

ARLT-J., AND PADGETT-M. (2000). Generation of a beam with a dark focus surrounded by regions of higher intensity: the optical bottle beam, *Optics Letters*, **25**(4), pp. 191–193.

AZAD-A. K., EFIMOV-A. V., GHOSH-S., SINGLETON-J., TAYLOR-A. J., AND CHEN-H.-T. (2017). Ultra-thin metasurface microwave flat lens for broadband applications, *Applied Physics Letters*, **110**(22), art. no. 224101.

BALAKRISHNAN-J., FISCHER-B. M., AND ABBOTT-D. (2009). Sensing the hygroscopicity of polymer and copolymer materials using terahertz time-domain spectroscopy, *Applied Optics*, **48**(12), pp. 2262–2266.

BALANIS-C. A. (2016). *Antenna Theory: Analysis and Design*, John Wiley & Sons.

BANERJEE-D., VON SPIEGEL-W., THOMSON-M. D., SCHABEL-S., AND ROSKOS-H. G. (2008). Diagnosing water content in paper by terahertz radiation, *Optics Express*, **16**(12), pp. 9060–9066.

BEERMANN-J., ERIKSEN-R. L., HOLMGAARD-T., PEDERSEN-K., AND BOZHEVOLNYI-S. I. (2014). Plasmonic black metals via radiation absorption by two-dimensional arrays of ultra-sharp convex grooves, *Scientific Reports*, **4**, art. no. 6904.

BEERMANN-J., ERIKSEN-R. L., SØNDERGAARD-T., HOLMGAARD-T., PEDERSEN-K., AND BOZHEVOLNYI-S. I. (2013). Plasmonic black metals by broadband light absorption in ultra-sharp convex grooves, *New Journal of Physics*, **15**(7), art. no. 073007.

BERRY-D., MALECH-R., AND KENNEDY-W. (1963). The reflectarray antenna, *IEEE Transactions on Antennas and Propagation*, **11**(6), pp. 645–651.

BLANCO-D., AND SAULEAU-R. (2018). Broadband and broad-angle multilayer polarizer based on hybrid optimization algorithm for low-cost Ka-band applications, *IEEE Transactions on Antennas and Propagation*, **66**(4), pp. 1874–1881.

BRÜCKNER-C., PRADARUTTI-B., STENZEL-O., STEINKOPF-R., RIEHEMANN-S., NOTNI-G., AND TÜNNERMANN-A. (2007). Broadband antireflective surface-relief structure for THz optics, *Optics Express*, **15**(3), pp. 779–789.

BUSCH-S., TOWN-G., SCHELLER-M., AND KOCH-M. (2015). Focus free terahertz reflection imaging and tomography with Bessel beams, *Journal of Infrared, Millimeter, and Terahertz Waves*, **36**(3), pp. 318–326.

CARRASCO-E., BARBA-M., AND ENCINAR-J. A. (2006). Aperture-coupled reflectarray element with wide range of phase delay, *Electronics Letters*, **42**(12), pp. 667–668.

CARRASCO-E., BARBA-M., AND ENCINAR-J. A. (2007). Reflectarray element based on aperture-coupled patches with slots and lines of variable length, *IEEE Transactions on Antennas and Propagation*, **55**(3), pp. 820–825.

CASTRO-C., ELSCHNER-R., MERKLE-T., SCHUBERT-C., AND FREUND-R. (2020). Experimental demonstrations of high-capacity THz-wireless transmission systems for beyond 5G, *IEEE Communications Magazine*, **58**(11), pp. 41–47.

CHAHARMIR-M. R., SHAKER-J., CUHACI-M., AND SEBAK-A. (2003). Reflectarray with variable slots on ground plane, *IEE Proceedings - Microwaves, Antennas and Propagation*, **150**(6), pp. 436–439.

CHAHARMIR-M. R., SHAKER-J., GAGNON-N., AND LEE-D. (2010). Design of broadband, single layer dual-band large reflectarray using multi open loop elements, *IEEE Transactions on Antennas and Propagation*, **58**(9), pp. 2875–2883.

CHANG-C.-C., HEADLAND-D., ABBOTT-D., WITHAYACHUMNANKUL-W., AND CHEN-H.-T. (2017). Demonstration of a highly efficient terahertz flat lens employing tri-layer metasurfaces, *Optics Letters*, **42**(9), pp. 1867–1870.

CHANG-C.-C., HUANG-L., NOGAN-J., AND CHEN-H.-T. (2018). Narrowband terahertz bandpass filters employing stacked bilayer metasurface antireflection structures, *APL Photonics*, **3**(5), art. no. 051602.

CHENG-Y., CHEN-H., ZHAO-J., MAO-X., AND CHENG-Z. (2018). Chiral metamaterial absorber with high selectivity for terahertz circular polarization waves, *Optical Materials Express*, **8**(5), pp. 1399–1409.

CHENG-Y., WANG-Y., NIU-Y., AND ZHAO-Z. (2020). Concealed object enhancement using multi-polarization information for passive millimeter and terahertz wave security screening, *Optics Express*, **28**(5), pp. 6350–6366.

CHENG-Y. Z., WITHAYACHUMNANKUL-W., UPADHYAY-A., HEADLAND-D., NIE-Y., GONG-R. Z., BHASKARAN-M., SRIRAM-S., AND ABBOTT-D. (2015). Ultrabroadband plasmonic absorber for terahertz waves, *Advanced Optical Materials*, **3**(3), pp. 376–380.

CHENG-Z., AND CHENG-Y. (2019). A multi-functional polarization convertor based on chiral metamaterial for terahertz waves, *Optics Communications*, **435**, pp. 178–182.

CHEN-H.-T., TAYLOR-A. J., AND YU-N. (2016a). A review of metasurfaces: physics and applications, *Reports on Progress in Physics*, **79**(7), art. no. 076401.

CHEN-H.-T., ZHOU-J., O'HARA-J. F., CHEN-F., AZAD-A. K., AND TAYLOR-A. J. (2010). Antireflection coating using metamaterials and identification of its mechanism, *Physical Review Letters*, **105**, art. no. 073901.

CHEN-L., QU-S., CHEN-B., BAI-X., NG-K., AND CHAN-C. H. (2017). Terahertz metasurfaces for absorber or reflectarray applications, *IEEE Transactions on Antennas and Propagation*, **65**(1), pp. 234–241.

CHEN-M., FAN-F., XU-S.-T., AND CHANG-S.-J. (2016b). Artificial high birefringence in all-dielectric gradient grating for broadband terahertz waves, *Scientific Reports*, **6**(1), pp. 1–10.

CHEN-Q., QU-S., LI-J., CHEN-Q., AND XIA-M. (2013a). An X-band reflectarray with novel elements and enhanced bandwidth, *IEEE Antennas and Wireless Propagation Letters*, **12**, pp. 317–320.

CHEN-Q., QU-S., ZHANG-X., AND XIA-M. (2012). Low-profile wideband reflectarray by novel elements with linear phase response, *IEEE Antennas and Wireless Propagation Letters*, **11**, pp. 1545–1547.

CHEN-Y. W., AND ZHANG-X.-C. (2014). Anti-reflection implementations for terahertz waves, *Frontiers of Optoelectronics*, **7**(2), pp. 243–262.

CHEN-Z., GONG-Y., DONG-H., NOTAKE-T., AND MINAMIDE-H. (2013b). Terahertz achromatic quarter wave plate: design, fabrication, and characterization, *Optics Communications*, **311**, pp. 1–5.

CHEON-H., YANG-H., AND SON-J. (2017). Toward clinical cancer imaging using terahertz spectroscopy, *IEEE Journal of Selected Topics in Quantum Electronics*, **23**(4), pp. 1–9.

COLBURN-S., ZHAN-A., AND MAJUMDAR-A. (2018). Metasurface optics for full-color computational imaging, *Science Advances*, **4**(2), art. no. eaar2114.

CONG-L., XU-N., GU-J., SINGH-R., HAN-J., AND ZHANG-W. (2014). Highly flexible broadband terahertz metamaterial quarter-wave plate, *Laser & Photonics Reviews*, **8**(4), pp. 626–632.

DAI-J., ZHANG-J., ZHANG-W., AND GRISCHKOWSKY-D. (2004). Terahertz time-domain spectroscopy characterization of the far-infrared absorption and index of refraction of high-resistivity, float-zone silicon, *Journal of the Optical Society of America B*, **21**(7), pp. 1379–1386.

DECKER-M., STAUDE-I., FALKNER-M., DOMINGUEZ-J., NESHEV-D. N., BRENER-I., PERTSCH-T., AND KIVSHAR-Y. S. (2015). High-efficiency dielectric Huygens' surfaces, *Advanced Optical Materials*, **3**(6), pp. 813–820.

DE VRIES-H. (1951). Rotatory power and other optical properties of certain liquid crystals, *Acta Crystallographica*, **4**(3), pp. 219–226.

DORNEY-T. D., BARANIUK-R. G., AND MITTLEMAN-D. M. (2001). Material parameter estimation with terahertz time-domain spectroscopy, *Journal of the Optical Society of America A*, **18**(7), pp. 1562–1571.

DU-L.-H., LI-J., ZHAI-Z.-H., MENG-K., LIU-Q., ZHONG-S.-C., ZHOU-P.-W., ZHU-L.-G., LI-Z.-R., AND PENG-Q.-X. (2016). A high-performance broadband terahertz absorber based on sawtooth-shape doped-silicon, *AIP Advances*, **6**(5), art. no. 055112.

EISELE-H., AND HADDAD-G. I. (1998). Two-terminal millimeter-wave sources, *IEEE Transactions on Microwave Theory and Techniques*, **46**(6), pp. 739–746.

EULER-M., FUSCO-V., CAHILL-R., AND DICKIE-R. (2010). 325 GHz single layer sub-millimeter wave FSS based split slot ring linear to circular polarization convertor, *IEEE Transactions on Antennas and Propagation*, **58**(7), pp. 2457–2459.

FAN-R.-H., ZHOU-Y., REN-X.-P., PENG-R.-W., JIANG-S.-C., XU-D.-H., XIONG-X., HUANG-X.-R., AND WANG-M. (2015). Freely tunable broadband polarization rotator for terahertz waves, *Advanced Materials*, **27**(7), pp. 1201–1206.

FAN-S., JEONG-K., WALLACE-V. P., AND AMAN-Z. (2019). Use of terahertz waves to monitor moisture content in high-pressure natural gas pipelines, *Energy & Fuels*, **33**(9), pp. 8026–8031.

FEI-P., SHEN-Z., WEN-X., AND NIAN-F. (2015). A single-layer circular polarizer based on hybrid meander line and loop configuration, *IEEE Transactions on Antennas and Propagation*, **63**(10), pp. 4609–4614.

GANSEL-J. K., LATZEL-M., FRÖLICH-A., KASCHKE-J., THIEL-M., AND WEGENER-M. (2012). Tapered gold-helix metamaterials as improved circular polarizers, *Applied Physics Letters*, **100**(10), art. no. 101109.

GANSEL-J. K., THIEL-M., RILL-M. S., DECKER-M., BADE-K., SAILE-V., VON FREYMANN-G., LINDEN-S., AND WEGENER-M. (2009). Gold helix photonic metamaterial as broadband circular polarizer, *Science*, **325**(5947), pp. 1513–1515.

GAO-W., LEE-W. S. L., YU-X., FUJITA-M., NAGATSUMA-T., FUMEAUX-C., AND WITHAYACHUMNANKUL-W. (2021). Characteristics of effective-medium-clad dielectric waveguides, *IEEE Transactions on Terahertz Science and Technology*, **11**(1), pp. 28–41.

GAO-W., YU-X., FUJITA-M., NAGATSUMA-T., FUMEAUX-C., AND WITHAYACHUMNANKUL-W. (2019). Effective-medium-cladded dielectric waveguides for terahertz waves, *Optics Express*, **27**(26), pp. 38721–38734.

GEORGE-D. K., AND MARKELZ-A. G. (2013). *Terahertz Spectroscopy of Liquids and Biomolecules*, Springer Berlin Heidelberg, Berlin, Heidelberg, pp. 229–250.

GERCHBERG-R. W. (1972). A practical algorithm for the determination of phase from image and diffraction plane pictures, *Optik*, **35**, pp. 237–246.

GOODMAN-J. W. (2005). *Introduction to Fourier Optics*, Roberts and Company Publishers.

GRISCHKOWSKY-D., KEIDING-S., VAN EXTER-M., AND FATTINGER-C. (1990). Far-infrared time-domain spectroscopy with terahertz beams of dielectrics and semiconductors, *Journal of the Optical Society of America B*, **7**(10), pp. 2006–2015.

HAN-Z., OHNO-S., TOKIZANE-Y., NAWATA-K., NOTAKE-T., TAKIDA-Y., AND MINAMIDE-H. (2018). Off-resonance and in-resonance metamaterial design for a high-transmission terahertz-wave quarter-wave plate, *Optics Letters*, **43**(12), pp. 2977–2980.

HASANI-H., KAMYAB-M., AND MIRKAMALI-A. (2010). Broadband reflectarray antenna incorporating disk elements with attached phase-delay lines, *IEEE Antennas and Wireless Propagation Letters*, **9**, pp. 156–158.

HASHIMSHONY-D., GELTNER-I., COHEN-G., AVITZOUR-Y., ZIGLER-A., AND SMITH-C. (2001). Characterization of the electrical properties and thickness of thin epitaxial semiconductor layers by THz reflection spectroscopy, *Journal of Applied Physics*, **90**(11), pp. 5778–5781.

HAWKES-A. M., KATKO-A. R., AND CUMMER-S. A. (2013). A microwave metamaterial with integrated power harvesting functionality, *Applied Physics Letters*, **103**(16), art. no. 163901.

HEADLAND-D. (2017). *Efficient Terahertz-Range Beam Control Using Flat Optics*, PhD thesis, The University of Adelaide.

HEADLAND-D., CARRASCO-E., NIRANTAR-S., WITHAYACHUMNANKUL-W., GUTRUF-P., SCHWARZ-J., ABBOTT-D., BHASKARAN-M., SRIRAM-S., PERRUISSEAU-CARRIER-J., AND FUMEAUX-C. (2016a). Dielectric resonator reflectarray as high-efficiency nonuniform terahertz metasurface, *ACS Photonics*, **3**(6), pp. 1019–1026.

HEADLAND-D., FUJITA-M., AND NAGATSUMA-T. (2020a). Half-maxwell fisheye lens with photonic crystal waveguide for the integration of terahertz optics, *Optics Express*, **28**(2), pp. 2366–2380.

HEADLAND-D., MONNAI-Y., ABBOTT-D., FUMEAUX-C., AND WITHAYACHUMNANKUL-W. (2018a). Tutorial: terahertz beamforming, from concepts to realizations, *APL Photonics*, **3**(5), art. no. 051101.

HEADLAND-D., NIU-T., CARRASCO-E., ABBOTT-D., SRIRAM-S., BHASKARAN-M., FUMEAUX-C., AND WITHAYACHUMNANKUL-W. (2017). Terahertz reflectarrays and nonuniform metasurfaces, *IEEE Journal of Selected Topics in Quantum Electronics*, **23**(4), pp. 1–18.

HEADLAND-D., THURGOOD-P., STAVREVSKI-D., WITHAYACHUMNANKUL-W., ABBOTT-D., BHASKARAN-M., AND SRIRAM-S. (2015). Doped polymer for low-loss dielectric material in the terahertz range, *Optical Materials Express*, **5**(6), pp. 1373–1380.

HEADLAND-D., WITHAYACHUMNANKUL-W., WEBB-M., EBENDORFF-HEIDEPRIEM-H., LUITEN-A., AND ABBOTT-D. (2016b). Analysis of 3D-printed metal for rapid-prototyped reflective terahertz optics, *Optics Express*, **24**(15), pp. 17384–17396.

HEADLAND-D., WITHAYACHUMNANKUL-W., YAMADA-R., FUJITA-M., AND NAGATSUMA-T. (2018b). Terahertz multi-beam antenna using photonic crystal waveguide and Luneburg lens, *APL Photonics*, **3**(12), art. no. 126105.

HEADLAND-D., WITHAYACHUMNANKUL-W., YU-X., FUJITA-M., AND NAGATSUMA-T. (2020b). Unclad microphotonics for terahertz waveguides and systems, *Journal of Lightwave Technology*, **38**(24), pp. 6853–6862.

HEADLAND-D., YU-X., FUJITA-M., AND NAGATSUMA-T. (2019). Near-field out-of-plane coupling between terahertz photonic crystal waveguides, *Optica*, **6**(8), pp. 1002–1011.

HECHT-E. (2002). *Optics*, 4 edn, Addison-Wesley, San Francisco.

HERNANDEZ-CARDOSO-G., ROJAS-LANDEROS-S., ALFARO-GOMEZ-M., HERNANDEZ-SERRANO-A., SALAS-GUTIERREZ-I., LEMUS-BEDOLLA-E., CASTILLO-GUZMAN-A., LOPEZ-LEMUS-H., AND CASTRO-CAMUS-E. (2017). Terahertz imaging for early

screening of diabetic foot syndrome: a proof of concept, *Scientific Reports*, **7**, art. no. 42124.

HESLER-J., KERR-A., GRAMMER-W., AND WOLLACK-E. (2007). Recommendations for waveguide interfaces to 1 THz, *18th International Symposium on Space Terahertz Technology*, pp. 100–103.

HOMES-C. C., CARR-G. L., LOBO-R. P. S. M., LAVEIGNE-J. D., AND TANNER-D. B. (2007). Silicon beam splitter for far-infrared and terahertz spectroscopy, *Applied Optics*, **46**(32), pp. 7884–7888.

HOSAKO-I. (2005). Multilayer optical thin films for use at terahertz frequencies: method of fabrication, *Applied Optics*, **44**(18), pp. 3769–3773.

HU-A., CHU-F., GUO-C., LI-G., AND WU-J. (2018). Wideband reflective quarter-wave plates based on subwavelength mixed metal dielectric gratings, *Optik*, **163**, pp. 120–125.

HUANG-J., AND ENCINAR-J. A. (2007). *Reflectarray Antennas*, Vol. 30, John Wiley & Sons.

HUANG-L., CHANG-C.-C., ZENG-B., NOGAN-J., LUO-S.-N., TAYLOR-A. J., AZAD-A. K., AND CHEN-H.-T. (2017). Bilayer metasurfaces for dual- and broadband optical antireflection, *ACS Photonics*, **4**(9), pp. 2111–2116.

HUANG-L., CHOWDHURY-D. R., RAMANI-S., REITEN-M. T., LUO-S.-N., TAYLOR-A. J., AND CHEN-H.-T. (2012). Experimental demonstration of terahertz metamaterial absorbers with a broad and flat high absorption band, *Optics Letters*, **37**(2), pp. 154–156.

HUANG-Y., ZHOU-Y., AND WU-S.-T. (2007). Broadband circular polarizer using stacked chiral polymer films, *Optics Express*, **15**(10), pp. 6414–6419.

IEEE 802 LAN/MAN STANDARDS COMMITTEE. (2017). IEEE Standard for High Data Rate Wireless Multi-Media Networks–Amendment 2: 100 Gb/s Wireless Switched Point-to-Point Physical Layer, *IEEE Std 802.15.3d-2017 (Amendment to IEEE Std 802.15.3-2016 as amended by IEEE Std 802.15.3e-2017)*, pp. 1–55.

JEONG-J., KIM-D., PARK-H.-R., KANG-T., LEE-D., KIM-S., BAHK-Y.-M., AND KIM-D.-S. (2018). Anomalous extinction in index-matched terahertz nanogaps, *Nanophotonics*, **7**(1), pp. 347–354.

JIA-S. L., WAN-X., BAO-D., ZHAO-Y. J., AND CUI-T. J. (2015). Independent controls of orthogonally polarized transmitted waves using a Huygens metasurface, *Laser & Photonics Reviews*, **9**(5), pp. 545–553.

JI-Y.-Y., FAN-F., WANG-X.-H., AND CHANG-S.-J. (2018). Broadband controllable terahertz quarter-wave plate based on graphene gratings with liquid crystals, *Optics Express*, **26**(10), pp. 12852–12862.

KHAN-M. I., AND TAHIR-F. A. (2017). A compact half and quarter-wave plate based on bi-layer anisotropic metasurface, *Journal of Physics D: Applied Physics*, **50**(43), art. no. 43LT04.

KIM-D.-H., KIM-D.-S., HWANG-S., AND JANG-J.-H. (2012). Surface relief structures for a flexible broadband terahertz absorber, *Optics Express*, **20**(15), pp. 16815–16822.

KONONENKO-T. V., KNYAZEV-B. A., SOVYK-D. N., PAVELYEV-V. S., KOMLENOK-M. S., KOMANDIN-G. A., AND KONOV-V. I. (2020). Silicon kinoform cylindrical lens with low surface roughness for high-power terahertz radiation, *Optics & Laser Technology*, **123**, art. no. 105953.

KRUK-S., HOPKINS-B., KRAVCHENKO-I. I., MIROSHNICHENKO-A., NESHEV-D. N., AND KIVSHAR-Y. S. (2016). Broadband highly efficient dielectric metadevices for polarization control, *APL Photonics*, **1**(3), art. no. 030801.

LANDY-N. I., SAJUYIGBE-S., MOCK-J. J., SMITH-D. R., AND PADILLA-W. J. (2008). Perfect metamaterial absorber, *Physical Review Letters*, **100**, art. no. 207402.

LEE-W. S. L., AKO-R. T., LOW-M. X., BHASKARAN-M., SRIRAM-S., FUMEAUX-C., AND WITHAYACHUMNANKUL-W. (2018a). Dielectric-resonator metasurfaces for broadband terahertz quarter- and half-wave mirrors, *Optics Express*, **26**(11), pp. 14392–14406.

LEE-W. S., NIRANTAR-S., HEADLAND-D., BHASKARAN-M., SRIRAM-S., FUMEAUX-C., AND WITHAYACHUMNANKUL-W. (2018b). Broadband terahertz circular-polarization beam splitter, *Advanced Optical Materials*, **6**(3), art. no. 1700852.

LEHMAN-J. H., ENGTRAKUL-C., GENNETT-T., AND DILLON-A. C. (2005). Single-wall carbon nanotube coating on a pyroelectric detector, *Applied Optics*, **44**(4), pp. 483–488.

LEVY-U., AND FAINMAN-Y. (2004). Dispersion properties of inhomogeneous nanostructures, *Journal of the Optical Society of America A*, **21**(5), pp. 881–889.

LI-L., CHEN-Q., YUAN-Q., SAWAYA-K., MARUYAMA-T., FURUNO-T., AND UEBAYASHI-S. (2009). Novel broadband planar reflectarray with parasitic dipoles for wireless communication applications, *IEEE Antennas and Wireless Propagation Letters*, **8**, pp. 881–885.

LIU-H., LUO-K., TANG-S., PENG-D., HU-F., AND TU-L. (2018). An ultra-wideband THz/IR metamaterial absorber based on doped silicon, *Materials*, **11**(12), art. no. 2590.

LIU-Z., LI-Z., LIU-Z., CHENG-H., LIU-W., TANG-C., GU-C., LI-J., CHEN-H.-T., CHEN-S., AND TIAN-J. (2017). Single-layer plasmonic metasurface half-wave plates with wavelength-independent polarization conversion angle, *ACS Photonics*, **4**(8), pp. 2061–2069.

LOKSZTEJN-A., AND DZWOLAK-W. (2010). Vortex-induced formation of insulin amyloid superstructures probed by time-lapse atomic force microscopy and circular dichroism spectroscopy, *Journal of Molecular Biology*, **395**(3), pp. 643 – 655.

LUCYSZYN-S. (2007). Evaluating surface impedance models for terahertz frequencies at room temperature, *PIERS Online*, **3**(4), pp. 554–559.

LUO-X. (2018). Subwavelength optical engineering with metasurface waves, *Advanced Optical Materials*, **6**(7), art. no. 1701201.

LV-N., ZHANG-L., JIANG-L., MUHAMMAD-A., WANG-H., AND YUAN-L. (2020). A design of microfluidic chip with quasi-Bessel beam waveguide for scattering detection of label-free cancer cells, *Cytometry Part A*, **97**(1), pp. 78–90.

MAO-Y., XU-S., YANG-F., AND ELSHERBENI-A. Z. (2015). A novel phase synthesis approach for wideband reflectarray design, *IEEE Transactions on Antennas and Propagation*, **63**(9), pp. 4189–4193.

MCMASTER-W. H. (1954). Polarization and the Stokes parameters, *American Journal of Physics*, **22**(6), pp. 351–362.

MENG-H., XIANG-B., ZHANG-J., DOU-W., AND YU-Y. (2014). The generation of Bessel beam and its application in millimeter wave imaging, *Journal of Infrared, Millimeter, and Terahertz Waves*, **35**(2), pp. 208–217.

MENLO SYSTEMS. (2020). Fibre-coupled terahertz time-domain spectroscopy system (THz-TDS) TERA K15, https://www.menlosystems.com/products/thz-time-domain-solutions/terak15-terahertz-spectrometer/. Accessed: 2020-12-07.

MILES-R. E., ZHANG-X.-C., EISELE-H., AND KROTKUS-A. (2007). *Terahertz Frequency Detection and Identification of Materials and Objects*, Springer Science & Business Media.

MOMENI HASAN ABADI-S. M. A., AND BEHDAD-N. (2016a). A broadband, circular-polarization selective surface, *Journal of Applied Physics*, **119**(24), art. no. 244901.

MOMENI HASAN ABADI-S. M. A., AND BEHDAD-N. (2016b). Wideband linear-to-circular polarization converters based on miniaturized-element frequency selective surfaces, *IEEE Transactions on Antennas and Propagation*, **64**(2), pp. 525–534.

MONNAI-Y., JAHN-D., WITHAYACHUMNANKUL-W., KOCH-M., AND SHINODA-H. (2015). Terahertz plasmonic Bessel beamformer, *Applied Physics Letters*, **106**(2), art. no. 021101.

MORENO-PEÑARRUBIA-A., KUZNETSOV-S. A., AND BERUETE-M. (2020). Ultrathin subterahertz half-wave plate with high conversion efficiency based on Zigzag metasurface, *IEEE Transactions on Antennas and Propagation*, **68**(11), pp. 7700–7704.

NAFTALY-M., AND MILES-R. E. (2007). Terahertz time-domain spectroscopy for material characterization, *Proceedings of the IEEE*, **95**(8), pp. 1658–1665.

NAGAI-M., MUKAI-N., MINOWA-Y., ASHIDA-M., TAKAYANAGI-J., AND OHTAKE-H. (2014). Achromatic THz wave plate composed of stacked parallel metal plates, *Optics Letters*, **39**(1), pp. 146–149.

NAGATSUMA-T., DUCOURNAU-G., AND RENAUD-C. C. (2016). Advances in terahertz communications accelerated by photonics, *Nature Photonics*, **10**(6), pp. 371–379.

NAKATA-Y., TAIRA-Y., NAKANISHI-T., AND MIYAMARU-F. (2017). Freestanding transparent terahertz half-wave plate using subwavelength cut-wire pairs, *Optics Express*, **25**(3), pp. 2107–2114.

NELMS-N., AND DOWSON-J. (2005). Goldblack coating for thermal infrared detectors, *Sensors and Actuators A: Physical*, **120**(2), pp. 403 – 407.

NIELSEN-K., RASMUSSEN-H. K., ADAM-A. J. L., PLANKEN-P. C. M., BANG-O., AND JEPSEN-P. U. (2009). Bendable, low-loss Topas fibers for the terahertz frequency range, *Optics Express*, **17**(10), pp. 8592–8601.

NIU-L., WANG-K., YANG-Y., WU-Q., YE-X., YANG-Z., LIU-J., AND YU-H. (2019). Diffractive elements for zero-order Bessel beam generation with application in the terahertz reflection imaging, *IEEE Photonics Journal*, **11**(1), pp. 1–12.

NIU-T. (2015). *Terahertz Reflectarrays*, PhD thesis, The University of Adelaide.

NIU-T., WITHAYACHUMNANKUL-W., AND FUMEAUX-C. (2015). Terahertz broadband reflectarray with parallel elliptical dipoles, *2015 IEEE 4th Asia-Pacific Conference on Antennas and Propagation (APCAP)*, pp. 98–100.

NIU-T., WITHAYACHUMNANKUL-W., UNG-B. S.-Y., MENEKSE-H., BHASKARAN-M., SRIRAM-S., AND FUMEAUX-C. (2013). Experimental demonstration of reflectarray antennas at terahertz frequencies, *Optics Express*, **21**(3), pp. 2875–2889.

NIU-T., WITHAYACHUMNANKUL-W., UPADHYAY-A., GUTRUF-P., ABBOTT-D., BHASKARAN-M., SRIRAM-S., AND FUMEAUX-C. (2014). Terahertz reflectarray as a polarizing beam splitter, *Optics Express*, **22**(13), pp. 16148–16160.

PATTY-C. L., LUO-D. A., SNIK-F., ARIESE-F., BUMA-W. J., TEN KATE-I. L., VAN SPANNING-R. J., SPARKS-W. B., GERMER-T. A., GARAB-G., AND KUDENOV-M. W. (2018). Imaging linear and circular polarization features in leaves with complete mueller matrix polarimetry, *Biochimica et Biophysica Acta (BBA) - General Subjects*, **1862**(6), pp. 1350–1363.

PECORA-E. F., CORDARO-A., KIK-P. G., AND BRONGERSMA-M. L. (2018). Broadband antireflection coatings employing multiresonant dielectric metasurfaces, *ACS Photonics*, **5**(11), pp. 4456–4462.

PENG-Y., ZANG-X., ZHU-Y., SHI-C., CHEN-L., CAI-B., AND ZHUANG-S. (2015). Ultrabroadband terahertz perfect absorber by exciting multi-order diffractions in a double-layered grating structure, *Optics Express*, **23**(3), pp. 2032–2039.

PETERSSON-L. R., AND JIN-J.-M. (2006). A three-dimensional time-domain finite-element formulation for periodic structures, *IEEE Transactions on Antennas and Propagation*, **54**(1), pp. 12–19.

PEYTAVIT-E., DONCHE-C., LEPILLIET-S., DUCOURNAU-G., AND LAMPIN-J.-F. (2011). Thin-film transmission lines using cyclic olefin copolymer for millimetre-wave and terahertz integrated circuits, *Electronics Letters*, **47**(7), pp. 453–454.

PFEIFFER-C., AND GRBIC-A. (2013a). Cascaded metasurfaces for complete phase and polarization control, *Applied Physics Letters*, **102**(23), art. no. 231116.

PFEIFFER-C., AND GRBIC-A. (2013b). Metamaterial Huygens' surfaces: tailoring wave fronts with reflectionless sheets, *Physical Review Letters*, **110**, art. no. 197401.

PFEIFFER-C., AND GRBIC-A. (2013c). Millimeter-wave transmitarrays for wavefront and polarization control, *IEEE Transactions on Microwave Theory and Techniques*, **61**(12), pp. 4407–4417.

PFEIFFER-C., AND GRBIC-A. (2014). Bianisotropic metasurfaces for optimal polarization control: analysis and synthesis, *Physical Review Applied*, **2**, art. no. 044011.

PFEIFFER-C., EMANI-N. K., SHALTOUT-A. M., BOLTASSEVA-A., SHALAEV-V. M., AND GRBIC-A. (2014). Efficient light bending with isotropic metamaterial Huygens' surfaces, *Nano Letters*, **14**(5), pp. 2491–2497.

PISANO-G., NG-M. W., HAYNES-V., AND MAFFEI-B. (2012). A broadband metal-mesh half-wave plate for millimetre wave linear polarisation rotation, *Progress In Electromagnetics Research*, **25**, pp. 101–114.

POZAR-D. M., TARGONSKI-S. D., AND SYRIGOS-H. D. (1997). Design of millimeter wave microstrip reflectarrays, *IEEE Transactions on Antennas and Propagation*, **45**(2), pp. 287–296.

QU-S., ZHANG-H., WU-W., LI-P., YANG-S., AND NIE-Z. (2016). Wideband folded reflectarray using novel elements with high orthogonal polarization isolation, *IEEE Transactions on Antennas and Propagation*, **64**(7), pp. 3195–3200.

RANJBAR-B., AND GILL-P. (2009). Circular dichroism techniques: biomolecular and nanostructural analyses-a review, *Chemical Biology & Drug Design*, **74**(2), pp. 101–120.

REID-M., AND FEDOSEJEVS-R. (2006). Terahertz birefringence and attenuation properties of wood and paper, *Applied Optics*, **45**(12), pp. 2766–2772.

ROUHI-K., RAJABALIPANAH-H., AND ABDOLALI-A. (2019). Multi-bit graphene-based bias-encoded metasurfaces for real-time terahertz wavefront shaping: from controllable orbital angular momentum generation toward arbitrary beam tailoring, *Carbon*, **149**, pp. 125 – 138.

SAHA-A., BHATTACHARYA-K., AND CHAKRABORTY-A. K. (2012). Achromatic quarter-wave plate using crystalline quartz, *Applied Optics*, **51**(12), pp. 1976–1980.

SAHIN-S., NAHAR-N. K., AND SERTEL-K. (2018). Permittivity and loss characterization of SUEX epoxy films for mmW and THz applications, *IEEE Transactions on Terahertz Science and Technology*, **8**(4), pp. 397–402.

SALEH-B. E., AND TEICH-M. C. (2019). *Fundamentals of Photonics*, John Wiley & Sons.

SANZ-FERNÁNDEZ-J., SAENZ-E., AND DE MAAGT-P. (2015). A circular polarization selective surface for space applications, *IEEE Transactions on Antennas and Propagation*, **63**(6), pp. 2460–2470.

SCHELLER-M. (2011). Real-time terahertz material characterization by numerical three-dimensional optimization, *Optics Express*, **19**(11), pp. 10647–10655.

SCHNEIDER-T., WIATREK-A., PREUSSLER-S., GRIGAT-M., AND BRAUN-R. (2012). Link budget analysis for terahertz fixed wireless links, *IEEE Transactions on Terahertz Science and Technology*, **2**(2), pp. 250–256.

SCHURIG-D., MOCK-J. J., JUSTICE-B., CUMMER-S. A., PENDRY-J. B., STARR-A. F., AND SMITH-D. R. (2006). Metamaterial electromagnetic cloak at microwave frequencies, *Science*, **314**(5801), pp. 977–980.

SEDRA-A. S., SEDRA-D. E. A. S., SMITH-K. C., AND SMITH-K. C. (1998). *Microelectronic Circuits*, New York: Oxford University Press.

SHALAEV-V. M., CAI-W., CHETTIAR-U. K., YUAN-H.-K., SARYCHEV-A. K., DRACHEV-V. P., AND KILDISHEV-A. V. (2005). Negative index of refraction in optical metamaterials, *Optics Letters*, **30**(24), pp. 3356–3358.

SHANNON-C. E. (1949). Communication in the presence of noise, *Proceedings of the IRE*, **37**(1), pp. 10–21.

SHEN-Y. C., LO-T., TADAY-P. F., COLE-B. E., TRIBE-W. R., AND KEMP-M. C. (2005). Detection and identification of explosives using terahertz pulsed spectroscopic imaging, *Applied Physics Letters*, **86**(24), art. no. 241116.

SHI-C., ZANG-X. F., CHEN-L., PENG-Y., CAI-B., NASH-G. R., AND ZHU-Y. M. (2016). Compact broadband terahertz perfect absorber based on multi-interference and

diffraction effects, *IEEE Transactions on Terahertz Science and Technology*, **6**(1), pp. 40–44.

SHI-C., ZANG-X., WANG-Y., CHEN-L., CAI-B., AND ZHU-Y. (2014). A polarization-independent broadband terahertz absorber, *Applied Physics Letters*, **105**(3), art. no. 031104.

SHI-H., AND HAO-Y. (2018). Wide-angle optical half-wave plate from the field transformation approach and form-birefringence theory, *Optics Express*, **26**(16), pp. 20132–20144.

SHI-J., WANG-Y., CHEN-T., XU-D., ZHAO-H., CHEN-L., YAN-C., TANG-L., HE-Y., FENG-H., AND YAO-J. (2018). Automatic evaluation of traumatic brain injury based on terahertz imaging with machine learning, *Optics Express*, **26**(5), pp. 6371–6381.

SHIN-H. J., KIM-S.-H., PARK-K., LIM-M.-C., CHOI-S.-W., AND OK-G. (2017). Free-standing guided-mode resonance humidity sensor in terahertz, *Sensors and Actuators A: Physical*, **268**, pp. 27 – 31.

SIEGEL-P. H. (2002). Terahertz technology, *IEEE Transactions on Microwave Theory and Techniques*, **50**(3), pp. 910–928.

SINGH-R., CAO-W., AL-NAIB-I., CONG-L., WITHAYACHUMNANKUL-W., AND ZHANG-W. (2014). Ultrasensitive terahertz sensing with high-Q Fano resonances in metasurfaces, *Applied Physics Letters*, **105**(17), art. no. 171101.

SINGH-R., PLUM-E., MENZEL-C., ROCKSTUHL-C., AZAD-A. K., CHEVILLE-R. A., LEDERER-F., ZHANG-W., AND ZHELUDEV-N. I. (2009). Terahertz metamaterial with asymmetric transmission, *Physical Review B*, **80**, art. no. 153104.

SOBHANI-H., ROOHOLAMININEJAD-H., AND BAHRAMPOUR-A. (2016). Creation of twisted terahertz waves carrying orbital angular momentum via a plasma vortex, *Journal of Physics D: Applied Physics*, **49**(29), art. no. 295107.

STEPHEN-L., YOGESH-N., AND SUBRAMANIAN-V. (2018). Broadband asymmetric transmission of linearly polarized electromagnetic waves based on chiral metamaterial, *Journal of Applied Physics*, **123**(3), art. no. 033103.

SUN-J., TIMURDOGAN-E., YAACOBI-A., HOSSEINI-E. S., AND WATTS-M. R. (2013). Large-scale nanophotonic phased array, *Nature*, **493**, art. no. 195.

TAMMINEN-A., MÄKELÄ-S., ALA-LAURINAHO-J., HÄKLI-J., KOIVISTO-P., RANTAKARI-P., SÄILY-J., LUUKANEN-A., AND RÄISÄNEN-A. V. (2013). Reflectarray design for 120-GHz radar application: measurement results, *IEEE Transactions on Antennas and Propagation*, **61**(10), pp. 5036–5047.

TANG-W., LI-X., DAI-J. Y., JIN-S., ZENG-Y., CHENG-Q., AND CUI-T. J. (2019). Wireless communications with programmable metasurface: transceiver design and experimental results, *China Communications*, **16**(5), pp. 46–61.

TAO-H., LANDY-N. I., BINGHAM-C. M., ZHANG-X., AVERITT-R. D., AND PADILLA-W. J. (2008). A metamaterial absorber for the terahertz regime: design, fabrication and characterization, *Optics Express*, **16**(10), pp. 7181–7188.

TARGONSKI-S. D., AND POZAR-D. M. (1996). Minimization of beam squint in microstrip reflectarrays using an offset feed, *IEEE Antennas and Propagation Society International Symposium. 1996 Digest*, pp. 1326–1329.

TAVALLAEE-A. A., WILLIAMS-B. S., HON-P. W. C., ITOH-T., AND CHEN-Q.-S. (2011). Terahertz quantum-cascade laser with active leaky-wave antenna, *Applied Physics Letters*, **99**(14), art. no. 141115.

TZYDYNZHAPOV-G., GUSIKHIN-P., MURAVEV-V., DREMIN-A., NEFYODOV-Y., AND KUKUSHKIN-I. (2020). New real-time sub-terahertz security body scanner, *Journal of Infrared, Millimeter, and Terahertz Waves*, pp. 1–10.

VALENTINE-J., ZHANG-S., ZENTGRAF-T., ULIN-AVILA-E., GENOV-D. A., BARTAL-G., AND ZHANG-X. (2008). Three-dimensional optical metamaterial with a negative refractive index, *Nature*, **455**(7211), pp. 376–379.

VATANSEVER-F., AND HAMBLIN-M. R. (2012). Far infrared radiation (FIR): its biological effects and medical applications, *Photonics & Lasers in Medicine*, **1**(4), pp. 255–266.

WAGNER-GENTNER-A., GRAF-U., RABANUS-D., AND JACOBS-K. (2006). Low loss THz window, *Infrared Physics & Technology*, **48**(3), pp. 249–253.

WALIA-S., SHAH-C. M., GUTRUF-P., NILI-H., CHOWDHURY-D. R., WITHAYACHUMNANKUL-W., BHASKARAN-M., AND SRIRAM-S. (2015). Flexible metasurfaces and metamaterials: a review of materials and fabrication processes at micro-and nano-scales, *Applied Physics Reviews*, **2**(1), art. no. 011303.

WANG-D., GU-Y., GONG-Y., QIU-C.-W., AND HONG-M. (2015a). An ultrathin terahertz quarter-wave plate using planar babinet-inverted metasurface, *Optics Express*, **23**(9), pp. 11114–11122.

WANG-H. B., CHENG-Y. J., AND CHEN-Z. N. (2020). Wideband and wide-angle single-layered-substrate linear-to-circular polarization metasurface converter, *IEEE Transactions on Antennas and Propagation*, **68**(2), pp. 1186–1191.

WANG-Q., ZHANG-X., XU-Y., TIAN-Z., GU-J., YUE-W., ZHANG-S., HAN-J., AND ZHANG-W. (2015b). A broadband metasurface-based terahertz flat-lens array, *Advanced Optical Materials*, **3**(6), pp. 779–785.

WASELIKOWSKI-S., KRATT-K., BADILITA-V., WALLRABE-U., KORVINK-J. G., AND WALTHER-M. (2010). Three-dimensional microcoils as terahertz metamaterial with electric and magnetic response, *Applied Physics Letters*, **97**(26), art. no. 261105.

WATTS-C. M., LIU-X., AND PADILLA-W. J. (2012). Metamaterial electromagnetic wave absorbers, *Advanced Materials*, **24**(23), pp. OP98–OP120.

WATTS-C. M., SHREKENHAMER-D., MONTOYA-J., LIPWORTH-G., HUNT-J., SLEASMAN-T., KRISHNA-S., SMITH-D. R., AND PADILLA-W. J. (2014). Terahertz compressive imaging with metamaterial spatial light modulators, *Nature Photonics*, **8**(8), pp. 605–609.

WEN-Q.-Y., ZHANG-H.-W., XIE-Y.-S., YANG-Q.-H., AND LIU-Y.-L. (2009). Dual band terahertz metamaterial absorber: design, fabrication, and characterization, *Applied Physics Letters*, **95**(24), art. no. 241111.

WILLIAMS-B. S. (2007). Terahertz quantum-cascade lasers, *Nature Photonics*, **1**(9), pp. 517–525.

WILTSE-J. C. (1984). History of millimeter and submillimeter waves, *IEEE Transactions on Microwave Theory and Techniques*, **32**(9), pp. 1118–1127.

WITHAYACHUMNANKUL-W., SHAH-C. M., FUMEAUX-C., KALTENECKER-K., WALTHER-M., FISCHER-B. M., ABBOTT-D., BHASKARAN-M., AND SRIRAM-S. (2013). Terahertz localized surface plasmon resonances in coaxial microcavities, *Advanced Optical Materials*, **1**(6), pp. 443–448.

WITHAYACHUMNANKUL-W., SHAH-C. M., FUMEAUX-C., UNG-B. S.-Y., PADILLA-W. J., BHASKARAN-M., ABBOTT-D., AND SRIRAM-S. (2014). Plasmonic resonance toward terahertz perfect absorbers, *ACS Photonics*, **1**(7), pp. 625–630.

WITHAYACHUMNANKUL-W., YAMADA-R., FUJITA-M., AND NAGATSUMA-T. (2018). All-dielectric rod antenna array for terahertz communications, *APL Photonics*, **3**(5), art. no. 051707.

WU-H., LUO-Q., CHEN-H., HAN-Y., YU-X., AND LIU-S. (2019). Magnetically controllable nonreciprocal Goos-Hänchen shift supported by a magnetic plasmonic gradient metasurface, *Physical Review A*, **99**, art. no. 033820.

WU-J., NG-B., LIANG-H., BREESE-M. B. H., HONG-M., MAIER-S. A., MOSER-H. O., AND HESS-O. (2014). Chiral metafoils for terahertz broadband high-contrast flexible circular polarizers, *Physical Review Applied*, **2**, art. no. 014005.

WU-J., NG-B., TURAGA-S. P., BREESE-M. B. H., MAIER-S. A., HONG-M., BETTIOL-A. A., AND MOSER-H. O. (2013). Free-standing terahertz chiral meta-foils exhibiting strong optical activity and negative refractive index, *Applied Physics Letters*, **103**(14), art. no. 141106.

WU-L., XU-D., WANG-Y., ZHANG-Y., WANG-H., LIAO-B., GONG-S., CHEN-T., WU-N., FENG-H., AND YAO-J. (2020). Horizontal-scanning attenuated total reflection terahertz imaging for biological tissues, *Neurophotonics*, **7**(2), pp. 1 – 10.

YAKOVLEV-E. V., ZAYTSEV-K. I., DOLGANOVA-I. N., AND YURCHENKO-S. O. (2015). Non-destructive evaluation of polymer composite materials at the manufacturing stage using terahertz pulsed spectroscopy, *IEEE Transactions on Terahertz Science and Technology*, **5**(5), pp. 810–816.

YANG-B., YE-W.-M., YUAN-X.-D., ZHU-Z.-H., AND ZENG-C. (2013). Design of ultrathin plasmonic quarter-wave plate based on period coupling, *Optics Letters*, **38**(5), pp. 679–681.

YANG-Q., GU-J., XU-Y., ZHANG-X., LI-Y., OUYANG-C., TIAN-Z., HAN-J., AND ZHANG-W. (2017). Broadband and robust metalens with nonlinear phase profiles for efficient terahertz wave control, *Advanced Optical Materials*, **5**(10), art. no. 1601084.

YANG-X., ZHAO-X., YANG-K., LIU-Y., LIU-Y., FU-W., AND LUO-Y. (2016). Biomedical applications of terahertz spectroscopy and imaging, *Trends in Biotechnology*, **34**(10), pp. 810 – 824.

YANG-Z. Y., ZHAO-M., LU-P. X., AND LU-Y. F. (2010a). Ultrabroadband optical circular polarizers consisting of double-helical nanowire structures, *Optics Letters*, **35**(15), pp. 2588–2590.

YANG-Z. Y., ZHAO-M., LU-P. X., AND LU-Y. F. (2010b). Ultrabroadband optical circular polarizers consisting of double-helical nanowire structures, *Optics Letters*, **35**(15), pp. 2588–2590.

YOON-G., LEE-D., NAM-K. T., AND RHO-J. (2018). Geometric metasurface enabling polarization independent beam splitting, *Scientific Reports*, **8**(1), pp. 1–8.

YOSHIOKA-T., OGATA-T., NONAKA-T., MORITSUGU-M., KIM-S.-N., AND KURIHARA-S. (2005). Reversible-photon-mode full-color display by means of photochemical modulation of a helically cholesteric structure, *Advanced Materials*, **17**(10), pp. 1226–1229.

YOU-X., AKO-R. T., LEE-W. S. L., BHASKARAN-M., SRIRAM-S., FUMEAUX-C., AND WITHAYACHUMNANKUL-W. (2020a). Broadband terahertz transmissive quarter-wave metasurface, *APL Photonics*, **5**(9), art. no. 096108.

YOU-X., AKO-R. T., LEE-W. S. L., BHASKARAN-M., SRIRAM-S., FUMEAUX-C., AND WITHAYACHUMNANKUL-W. (2021a). Terahertz transmissive half-wave metasurface with enhanced bandwidth. (Under review).

YOU-X., AKO-R. T., LEE-W. S. L., LOW-M. X., BHASKARAN-M., SRIRAM-S., FUMEAUX-C., AND WITHAYACHUMNANKUL-W. (2019a). Terahertz reflectarray with enhanced bandwidth, *Advanced Optical Materials*, **7**(20), art. no. 1900791.

YOU-X., FUMEAUX-C., AND WITHAYACHUMNANKUL-W. (2018). Terahertz focusing reflectarray with enhanced bandwidth, *43rd International Conference on Infrared, Millimeter, and Terahertz Waves (IRMMW-THz)*. Nagoya, Japan, DOI: 10.1109/IRMMW-THz.2018.8510345.

YOU-X., FUMEAUX-C., AND WITHAYACHUMNANKUL-W. (2019b). Broadband terahertz quarter-wave plate design, *44th International Conference on Infrared, Millimeter, and Terahertz Waves (IRMMW-THz)*. Paris, France, DOI: 10.1109/IRMMW-THz.2019.8874192.

YOU-X., FUMEAUX-C., AND WITHAYACHUMNANKUL-W. (2021b). Concept of mechanically tunable terahertz circular polarizer, *11th International Conference on Metamaterials, Photonic Crystals and Plasmonics (META)*. Warsaw, Poland (Invited; scheduled).

YOU-X., FUMEAUX-C., AND WITHAYACHUMNANKUL-W. (2021c). Systematically designed broadband terahertz metasurfaces, *SPIE Next-Generation Spectroscopic Technologies XIV*. Florida, USA (Invited).

YOU-X., UPADHYAY-A., CHENG-Y., BHASKARAN-M., SRIRAM-S., FUMEAUX-C., AND WITHAYACHUMNANKUL-W. (2020b). Ultra-wideband far-infrared absorber based on anisotropically etched doped silicon, *Optics Letters*, **45**(5), pp. 1196–1199.

YUE-G., WANG-Z., CHEN-L., CHENG-L., TANG-J., ZOU-X., ZENG-Y., AND LI-L. (2017). Demonstration of 60 GHz millimeter-wave short-range wireless communication system at 3.5 Gbps over 5 m range, *Science China Information Sciences*, **60**(8), art. no. 080306.

YU-N., AIETA-F., GENEVET-P., KATS-M. A., GABURRO-Z., AND CAPASSO-F. (2012). A broadband, background-free quarter-wave plate based on plasmonic metasurfaces, *Nano Letters*, **12**(12), pp. 6328–6333.

YUN-J., OH-S. J., SONG-K., YOON-D., SON-H. Y., CHOI-Y., HUH-Y., AND RIEH-J. (2017). Terahertz reflection-mode biological imaging based on InP HBT source and detector, *IEEE Transactions on Terahertz Science and Technology*, **7**(3), pp. 274–283.

YU-X., OHTA-M., TAKIZAWA-N., MIKAME-K., ONO-S., AND BAE-J. (2019a). Femtosecond-laser-fabricated periodic tapered structures on a silicon substrate for terahertz antireflection, *Applied Optics*, **58**(35), pp. 9595–9602.

YU-X., SUGETA-M., YAMAGAMI-Y., FUJITA-M., AND NAGATSUMA-T. (2019b). Simultaneous low-loss and low-dispersion in a photonic-crystal waveguide for terahertz communications, *Applied Physics Express*, **12**(1), art. no. 012005.

ZANG-X., SHI-C., CHEN-L., CAI-B., ZHU-Y., AND ZHUANG-S. (2015). Ultra-broadband terahertz absorption by exciting the orthogonal diffraction in dumbbell-shaped gratings, *Scientific Reports*, **5**, art. no. 8901.

ZHAI-M., YUAN-W., AND HAN-Z. (2017). Efficient terahertz plasmonic absorbers with v-grooves using highly doped silicon substrate and simple wet-etching techniques, *Journal of Infrared, Millimeter, and Terahertz Waves*, **38**(12), pp. 1502–1509.

ZHANG-B., HENDRICKSON-J., NADER-N., CHEN-H.-T., AND GUO-J. (2014). Metasurface optical antireflection coating, *Applied Physics Letters*, **105**(24), art. no. 241113.

ZHANG-S., PARK-Y.-S., LI-J., LU-X., ZHANG-W., AND ZHANG-X. (2009). Negative refractive index in chiral metamaterials, *Physical Review Letters*, **102**, art. no. 023901.

ZHANG-X., CHANG-T., CUI-H.-L., SUN-Z., YANG-C., YANG-X., LIU-L., AND FAN-W. (2017). A free-space measurement technique of terahertz dielectric properties, *Journal of Infrared, Millimeter, and Terahertz Waves*, **38**(3), pp. 356–365.

ZHANG-Y., ZHANG-J., LUO-G., ZHOU-X., XIE-G., ZHU-T., AND LIU-Z. (2005). Fabrication of silicon-based multilevel nanostructures via scanning probe oxidation and anisotropic wet etching, *Nanotechnology*, **16**(4), art. no. 422.

ZHAO-H., WANG-Y., CHEN-L., SHI-J., MA-K., TANG-L., XU-D., YAO-J., FENG-H., AND CHEN-T. (2018a). High-sensitivity terahertz imaging of traumatic brain injury in a rat model, *Journal of Biomedical Optics*, **23**(3), pp. 1 – 7.

ZHAO-J., ZHANG-C., CHENG-Q., YANG-J., AND CUI-T. J. (2018b). An optically transparent metasurface for broadband microwave antireflection, *Applied Physics Letters*, **112**(7), art. no. 073504.

ZHAO-Y., BELKIN-M., AND ALÙ-A. (2012). Twisted optical metamaterials for planarized ultrathin broadband circular polarizers, *Nature Communications*, **3**(1), pp. 1–7.

ZHAO-Y., ENGHETA-N., AND ALÙ-A. (2011). Homogenization of plasmonic metasurfaces modeled as transmission-line loads, *Metamaterials*, **5**(2), pp. 90–96.

ZHOU-M., SØRENSEN-S. B., KIM-O. S., JØRGENSEN-E., MEINCKE-P., AND BREINBJERG-O. (2013). Direct optimization of printed reflectarrays for contoured beam satellite antenna applications, *IEEE Transactions on Antennas and Propagation*, **61**(4), pp. 1995–2004.

ZHOU-M., SØRENSEN-S. B., KIM-O. S., JØRGENSEN-E., MEINCKE-P., BREINBJERG-O., AND TOSO-G. (2014). The generalized direct optimization technique for printed reflectarrays, *IEEE Transactions on Antennas and Propagation*, **62**(4), pp. 1690–1700.

ZI-J., XU-Q., WANG-Q., TIAN-C., LI-Y., ZHANG-X., HAN-J., AND ZHANG-W. (2018). Antireflection-assisted all-dielectric terahertz metamaterial polarization converter, *Applied Physics Letters*, **113**(10), art. no. 101104.

ZOU-L., LÓPEZ-GARCÍA-M., WITHAYACHUMNANKUL-W., SHAH-C. M., MITCHELL-A., BHASKARAN-M., SRIRAM-S., OULTON-R., KLEMM-M., AND FUMEAUX-C. (2014). Spectral and angular characteristics of dielectric resonator metasurface at optical frequencies, *Applied Physics Letters*, **105**(19), art. no. 191109.

ZOU-L., WITHAYACHUMNANKUL-W., SHAH-C. M., MITCHELL-A., BHASKARAN-M., SRIRAM-S., AND FUMEAUX-C. (2013). Dielectric resonator nanoantennas at visible frequencies, *Optics Express*, **21**(1), pp. 1344–1352.